

A MOLECULAR PRECURSOR SOLID-STATE ROUTE TO INORGANIC
NANOPARTICLES

By

PO-YU HWANG

A DISSERTATION

Submitted to the faculty of Delaware State University in partial fulfillment
of the requirement for the degree of Doctor of Philosophy
of Applied Chemistry in the Department of Chemistry

DOVER, DELAWARE
December 2018

This dissertation is approved by the following members of the Final Oral Review Committee:

Dr. Cherese Winstead Casson, Committee Chairperson, Department of Chemistry, Delaware State University

Dr. Cheng-Yu Lai, Committee Co-Chairperson, Department of Mechanical and Material Engineering, Florida International University

Dr. Aristides Marcano, Committee Member, Division of Physical and Computational Sciences, Delaware State University

Dr. Gabriel Gwanmesia, Committee Member, Division of Physical and Computational Sciences, Delaware State University

Dr. Gulnihal Ozbay, Committee Member, Department of Agriculture and Natural Resources, Delaware State University

Dr. Kevin Dobson, External Committee Member, Institute of Energy Conversion, University of Delaware

DEDICATION

This dissertation is dedicated to my parents Ching-Ming Hwang and Hui-Chu Chuang and my sister Christina Hwang, who have supported me in my endeavor to pursue knowledge in the field of Chemistry with their persistent guidance and unyielding love. I would also like to thank my uncle Harrison Chuang and all members of the Chuang family, who have enabled my passion as a student of science and engineering and I appreciate their equal love and support to me as their own. The achievements and prestige I may enjoy tomorrow should belong and be enjoyed by all members of my beloved family.

Lastly, I'd like to extend the dedication to my dearest Valerie. On this day, I can say I have completed our dreams.

ACKNOWLEDGEMENT

It is with my utmost gratitude and appreciation that I write this acknowledgment to all of those who were integral to the academic growths and achievements in my pursuit to become a Doctor of Philosophy in Applied Chemistry here in Delaware State University. First, I would like to give my sincerest gratitude to my research advisor and co-advisor Dr. Cheng-Yu Lai and Dr. Daniela R. Radu, whose great mentorship has always challenged me to be the better version of myself both in academia and in life. They have granted me the knowledge and aptitude to pursue the career of a professional chemist and the important ethics to be a great human being. No words enough can convey my gratitude of your trust to me. Thank you!

Secondly, I would also like to give thanks to my fellow colleagues and friends, Dr. Dominik M. Berg, Nicholas Pizzi, Martin Chi, Mimi Liu, Anjuli Bhandari, Aaron R. Legar, Miranda L. Penny, and Dylan R. McConnell. Not only have they provided companionship, they have also helped me in tackling the many obstacles in the field of research. It has been a pleasure working and sharing quality time with you all.

Lastly, I would like to extend my gratitude to Dr. Cherese Winstead, who has acted as the chair of my dissertation committee and provided her full support. I would also like to thank fellow committee members, Dr. Aristides Marcano, Dr. Gabriel Gwanmesia and Dr. Gulinihal Ozbay of Delaware State University, and Dr. Kevin Dobson of Institute of Energy Conversion. I am humbled by your guidance and trust in the matter of my graduation. Thank you all!

This project is based upon work supported in part by the US Department of Energy Sunshot Initiative (Award DE-EE0006322) and the National Science Foundation (Grant No. 1458980 and No. 1435716). I'd like to thank our collaborator at the Institute of Energy Conversion of University of Delaware for the use of their facility and technical supports on thin-film photovoltaic device fabrications. The use of Stanford Synchrotron Radiation Lightsource, SLAC National Accelerator Laboratory, was supported by the US Department of Energy, Office of Basic Energy Science under the Contract No. DE-AC02-76SF00515. Finally, I'd also like to extend my thanks to the Department of Defense for their financial support.

ABSTRACT

Iron Pyrite (FeS_2) has been the center of development to obtain a high efficiency, low-cost, earth-abundant and environmental-friendly photovoltaic absorber materials in the field of solar research for many decades. Many studies have offered explanations attempting to solve the conundrum, but, between the innate and unsolvable stoichiometric and phase instability challenges and the contradictory conclusions, no effective solution has been made to address pyrite's failing to reach its theoretical capability.

Iron germanium sulfide (Fe_2GeS_4) has recently emerged as a potential thin-film photovoltaic absorber material to replace its binary predecessor. With the introduction of the third element, germanium (Ge), the new ternary material was theorized to confer better thermal stability while improving with better band-gap and retaining the favorable low-cost of production traits enjoyed by iron pyrite. This work proposes a facile solid-state synthesis route to obtain high-quality, phase pure Fe_2GeS_4 nanoparticles from molecular precursors undergoing mechanical mixing and a two-hour annealing procedure under a sulfur-rich atmosphere. Analysis of the resulting Fe_2GeS_4 product has demonstrated good thermal stability under elevated temperatures (up to 500 °C), and the elimination of the phase coexistence challenge in comparison to pyrite. A comprehensive phase shift mechanism of iron chalcogenides and a Fe_2GeS_4 reaction mechanism is proposed to supplement the discussion of pyrite's phase instability. A facile thin-films fabrication is designed by undergoing further mechanical processing and annealing treatment and is revealed that Fe_2GeS_4 withstands high temperature in the thin-film device.

TABLE OF CONTENTS

LIST OF TABLES	viii
LIST OF FIGURES	ix
LIST OF ABBREVIATIONS.....	xii
CHAPTER 1. INTRODUCTION	1
1.1. The Need for Solar Energy.....	1
1.2. The Photovoltaic Effects	3
1.3. Summary on Solar Cell Classifications.....	6
1.3.1. Silicon-based Photovoltaic Materials.....	7
1.3.2. Nanocrystals-based Thin-Film Photovoltaic Materials.....	8
1.3.3. Copper Chalcogenide-based Thin-Film Photovoltaic Materials.....	11
1.3.4. Iron Chalcogenide-based Thin-Film Photovoltaic Materials	12
1.4. Solid-State Synthesis in Chemistry	14
CHAPTER 2. LITERATURE	17
2.1. Iron Pyrite Thin-film Syntheses and Challenges.....	17
2.2. Challenges for Iron Pyrite as a Photovoltaic Material	21
2.2.1. Stoichiometric Instability of Iron Pyrite.....	22
2.2.2. Phase Instability of Iron Pyrite.....	23
2.2.3. Iron Pyrite's Dependence on Material Morphology	30
2.3. Proposal of New Types of Iron Chalcogenide Photovoltaic Material	31
2.4. Known Methods of Fe ₂ GeS ₄ Syntheses	32
2.4.1. Solution Synthesis of Colloidal Fe ₂ GeS ₄ Nanocrystals	32
2.4.2. Mechanochemical Processing and Post-Heat Treatment of Fe ₂ GeS ₄ Nanocrystals.....	36
CHAPTER 3. EXPERIMENTAL METHODS	43
3.1. Materials.....	43
3.2. Experimental Methods	43
3.2.1. Molecular Precursor Solid-State Synthesis of the Fe ₂ GeS ₄ Nanoparticles.....	44
3.2.2. Fabrication of the Fe ₂ GeS ₄ Thin-Films	46
3.3. Characterization of Fe ₂ GeS ₄ Nanoparticle Properties.....	51
CHAPTER 4. RAPID MOLECULAR SOLID-STATE SYNTHESIS TO CRYSTALLINE Fe₂GeS₄ NANOPARTICLES	54
Introduction	54

Background and Significance.....	55
4.1 Precursor Combination Test.....	57
4.2. Annealing Temperature Test.....	69
4.2.1. Acac-Gly Series Annealing Temperature Tests	70
4.2.2. Cl ₂ -Gly Series Annealing Temperature Test.....	80
4.2.3. Cl ₃ -Gly Series Annealing Temperature Test.....	91
4.3. Discussion of Iron Sulfides Phase Shift Paradigm.....	103
CHAPTER 5. FACILE APPROACH TO Fe₂GeS₄ NANOPARTICLE INK AND	
THIN-FILM PROCESSING	109
Introduction	109
Background and Significance.....	109
5.1. Ink Quality Test.....	110
5.2. Adhesion Test.....	112
5.3. Thin-Film Composition Test.....	114
5.4. Discussion	116
CHAPTER 6. CONCLUSION AND PATH FORWARD.....	118
REFERENCES.....	122

LIST OF TABLES

Table 3.1. Materials used in this dissertation	43
Table 4.1. Rietveld refinement data of the Acac-Gly series when annealed at 400 °C.....	71
Table 4.2. Rietveld refinement data of the Acac-Gly series when annealed at 450 °C.....	73
Table 4.3. Rietveld refinement data of the Acac-Gly series when annealed at 500 °C.....	75
Table 4.4. Rietveld refinement data of the Acac-Gly series when annealed at 550 °C.....	77
Table 4.5. Rietveld refinement data of the Acac-Gly series when annealed at 600 °C.....	79
Table 4.6. Rietveld refinement data of the Cl ₂ -Gly series when annealed at 400 °C.....	82
Table 4.7. Rietveld refinement data of the Cl ₂ -Gly series when annealed at 450 °C.....	84
Table 4.8. Rietveld refinement data of the Cl ₂ -Gly series when annealed at 500 °C.....	86
Table 4.9. Rietveld refinement data of the Cl ₂ -Gly series when annealed at 550 °C.....	88
Table 4.10. Rietveld refinement data of the Cl ₂ -Gly series when annealed at 600 °C.....	90
Table 4.11. Rietveld refinement data of the Cl ₃ -Gly series when annealed at 400 °C.....	93
Table 4.12. Rietveld refinement data of the Cl ₃ -Gly series when annealed at 450 °C.....	95
Table 4.13. Rietveld refinement data of the Cl ₃ -Gly series when annealed at 500 °C.....	97
Table 4.14. Rietveld refinement data of the Cl ₃ -Gly series when annealed at 550 °C.....	99
Table 4.15. Rietveld refinement data of the Cl ₃ -Gly series when annealed at 600 °C.....	101
Table 5.1. Comparison of the lift-off pressure of the sample ink 1 – 4 for the Adhesion Test..	113
Table 5.2. Refined phase analysis of Film Composition Study of Ink 4 post thin-film processing.	115

LIST OF FIGURES

Figure 1.1. Schematics of a typical solar cell and photovoltaic Effect.....	4
Figure 1.2. Effectiveness of a typical silicon-based solar cell in respect to solar radiation spectrum ³	5
Figure 1.3. Schematic of a typical chemical vapor deposition in a tube furnace ¹⁸	15
Figure 2.1. SEM images of a surface roughening by sintering of iron pyrite thin-film at 540 °C in sulfur vapor ¹⁶	20
Figure 2.2. (a) WAXRD, (b) Raman spectrum, and EDS Ratio of pyrite sample phase changes with increasing vacuum annealing temperature ²⁴	25
Figure 2.3. (a) XPS spectrum and (b) Fe _{1-δ} S molar fraction showing the adverse effect of increasing in vacuum annealing temperature to phase purity ²⁴	27
Figure 2.4. Effect of increasing vacuum annealing temperature versus (a) the Hall resistivity (ρ_{xy}), (b) the magnetoresistance (MR) and (c) the magnetization hysteresis loops of similarly produced FeS ₂ films ²⁴	29
Figure 2.5. Calculated optical absorption coefficients for FeS ₂ , Fe ₂ SiS ₄ , and Fe ₂ GeS ₄ ¹⁷	32
Figure 2.6. Fe XPS spectrum of the as-synthesized Fe ₂ GeS ₄ nanocrystals from 0 h to 24 h air exposure ³⁵	35
Figure 2.7. XRD patterns of the milled Fe ₂ GeS ₄ product over various milling times ³⁶	39
Figure 2.8. Schematic of the mechanochemical process utilized to synthesize Fe ₂ GeS ₄ NCs ³⁶	40
Figure 3.1. Schematic of the molecular precursor based solid-state approach utilized to synthesize Fe ₂ GeS ₄ NPs.....	44
Figure 3.2. Schematic of the processing of Fe ₂ GeS ₄ nanoparticle ink.	48
Figure 3.3. Schematic of the processing of Fe ₂ GeS ₄ thin-films.....	49

Figure 3.4. Schematics of the glued pin apparatus designed for the adhesion test.	50
Figure 4.1. Comparison of the XRD pattern of Cl ₂ -I ₄ product and Fe ₂ GeS ₄ literature.	59
Figure 4.2. Comparison of the XRD pattern of Acac-I ₄ product and Fe ₂ GeS ₄ literature.	60
Figure 4.3. Comparison of the XRD pattern of Acac-Gly product and Fe ₂ GeS ₄ literature.	62
Figure 4.4. Comparison of the XRD pattern of Cl ₂ -Gly product and Fe ₂ GeS ₄ literature.	64
Figure 4.5. Comparison of the XRD pattern of Cl ₃ -Gly product and Fe ₂ GeS ₄ literature.	67
Figure 4.6. Comparison of the XRD pattern measured for the precursor combination test.	68
Figure 4.7. TEM image of Fe ₂ GeS ₄ nanoparticles produced with Cl ₃ -Gly.	68
Figure 4.8. XRD patterns of the Acac-Gly series when annealed at 400 °C.	71
Figure 4.9. XRD patterns of the Acac-Gly series when annealed at 450 °C.	73
Figure 4.10. XRD patterns of the Acac-Gly series when annealed at 500 °C.	75
Figure 4.11. XRD patterns of the Acac-Gly series when annealed at 550 °C.	77
Figure 4.12. XRD patterns of the Acac-Gly series when annealed at 600 °C.	79
Figure 4.13. XRD patterns of the Cl ₂ -Gly series when annealed at 400 °C.	82
Figure 4.14. XRD patterns of the Cl ₂ -Gly series when annealed at 450 °C.	84
Figure 4.15. XRD patterns of the Cl ₂ -Gly series when annealed at 500 °C.	86
Figure 4.16. XRD patterns of the Cl ₂ -Gly series when annealed at 550 °C.	88
Figure 4.17. XRD patterns of the Cl ₂ -Gly series when annealed at 600 °C.	90
Figure 4.18. XRD patterns of the Cl ₃ -Gly series when annealed at 400 °C.	93
Figure 4.19. XRD patterns of the Cl ₃ -Gly series when annealed at 450 °C.	95
Figure 4.20. XRD patterns of the Cl ₃ -Gly series when annealed at 500 °C.	97
Figure 4.21. XRD patterns of the Cl ₃ -Gly series when annealed at 550 °C.	99

Figure 4.22. XRD patterns of the Cl ₃ -Gly series when annealed at 600 °C.....	100
Figure 4.23. Thermalgravimetric analysis of the 600 °C Cl ₃ -Gly product of Fe ₂ GeS ₄	103
Figure 4.24. Proposed mechanism of Fe ₂ GeS ₄ formation.	108
Figure 5.1. Photos of the Fe ₂ GeS ₄ nanoparticle inks made (a) Ink 1, (b) Ink 2, (c) Ink 3 and (d) Ink 4.	112
Figure 5.1. Typical diagram of lift-off pressure over time to determine the maximum pressure.	113
Figure 5.3. Comparison of the XRD patterns of the annealed Fe ₂ GeS ₄ films from 400 °C to 600 °C.	115
Figure 5.4. Raman spectroscopy of Film Composition Study of Ink 4 post thin-film processing. Each symbol and vertical drop-line marks different iron compound phase. The ■ symbol represents reference peaks of Fe ₂ GeS ₄ , the ● symbol represents those of greigite, and the ▲ symbol represents those of pyrite.	116

LIST OF ABBREVIATIONS

CIGS	Copper indium gallium sulfide
CSP	Chemical spray pyrolysis
CVD	Chemical vapor deposition
CVT	Chemical vapor transportation
CZTS	Copper zinc tin sulfide
EDS	Energy-dispersive X-ray spectroscopy
FTO	Fluorine tin oxide
HDA	Hexadecylamine
HMDS	Hexamethyldisilazane
ICDD	International Centre of Diffraction Data
ITO	Indium tin oxide
LP-MOCVD	Low pressure metalorganic chemical vapor deposition
NC	Nanocrystal
NP	Nanoparticle
ODE	Ocetadecene
PV	Photovoltaic
SEM	Scanning electron microscope
TEM	Transmission electron microscope
WAXRD	Wide-angle X-ray diffraction spectroscopy
XPS	X-ray photoelectron spectroscopy

CHAPTER 1. INTRODUCTION

1.1. The Need for Solar Energy

If one can summarize the history of human civilization, then it will be the endless conflicts and struggles for resources, whether it is in the form of land, precious metal, or even exotic trade goods. Fast-forward to the 20th century, the war for resources has transformed and become the competition to access fossil fuels due to the increasing demand to continuously power the human civilization. However, the energy crises in the past decades had not only caused the increasing strain to the global economy, it had also caused the rise in political tensions in the Middle East. However, an even severer consequence of the heavy reliance on fossil fuel comes in the form of the increasing pollution to the planet that we call our home.

Indeed, the dire outlook of a polluted and uninhabitable Earth has slowly become an irreversible and grim reality in everyone's mind near the end of the 20th century, and most of the energy solutions employed even in modern days have done little to alleviate the problem. According to a 2017 report generated by the U.S. Energy Information Administration, fossil fuels, which includes natural gas, coal and petroleum, was responsible for 62.7% of the total electricity generation in the U.S. in 2017. About 20.0% of the electricity were generated by nuclear power. The third place was taken by hydropower with 7.5% also as the leader of the renewable category¹. While the three mentioned above has served the power demand very well with 90.2% of the total electricity generated, they all caused potentially irreversible environmental impacts as consequences of using them. Fossil fuel power plants, for example, generate byproducts in the form of waste heat and greenhouse gases, including carbon dioxide,

water vapor, methane and others. The emission of these gases to the atmosphere has been speculated to be responsible for the greenhouse effect with the increase of Earth's surface temperature steadily and dangerously close to the point of no return. The release of the particulate matter, also known as PM, into the atmosphere has also been linked to have adverse health effects, including heart and lung diseases². Nuclear power plants produce the byproduct in the form of the radioactive waste, a hazardous material to the environment and all forms of life that requires proper disposal facilities as exposure could cancer. Also, the mishandling of the operation could cause environment disaster, such as the one in Chernobyl and Fukushima, where high-level of radiations have caused the surrounding lands inhabitable for human settlements. Lastly, the environmental consequence of building a hydropower plant includes changing the water flow and the landscape forever, which also bears the possibility of affecting local fish species in numerous adverse ways.

In the recent decades, there has been a surge of interest to search for a highly efficient, yet environmental-friendly renewable energy source. Among the many renewable energy solutions that have been studied thoroughly over the decades, solar energy has come forward as a very promising solution. Solar energy is the harness of the light and heat of sunlight into the usable and storable energy in the form of electricity. It is a clean energy because solar, unlike fossil fuels or nuclear energy, by principle does not produce hazardous wastes and release them into the environment. It is also a renewable energy due to that sunlight is the most plentiful and widest distributed source of energy that is also seemingly endless as it will continue to exist for as long as the sun does. In addition, the effect of climate and the latitude of a region can be detrimental to the performance of the solar cells. Despite the limitations that should be

considered, it does not overshadow the promise of clean and renewable that is solar power and undermine the interest of developing high efficiency photovoltaic materials capable of providing day-to-day electric usage, and this goal has been one of the top priorities to governments and scientific community around the globe.

1.2. The Photovoltaic Effects

Most of the power generations in the U.S., as mentioned above, are done by fossil fuels and nuclear power stations, which both are classified as the thermal power station. For most types thermal power stations, they rely on converting the individual energy sources to produce thermal energy, typically by the combustion of the fuel, and transforming them into kinetic energy through mechanical motions. For example, a fossil fuel power station produces heat by the combustion of natural gas, coal, or petroleum in a steam boiler. The steam created is then directed to drive a steam turbine to cause the kinetic motion necessary to generate electricity via electric generators. Power productions such as the above example are based on the steam engine idea from the industrial era to turn kinetic energy into power. On the other hand, solar power is based off a different concept entirely.

A solar power station, instead, relies on the principle of the “photovoltaic effect,” as shown in the schematic in Figure 1.1, it produces electricity first by absorbing the photons of the sunlight into a semiconductor material. Once absorbed, the photon causes the excitation of the electrons to a higher energy state, while still contained within the material itself. The energy gap required to cause an excitation of an electron is called the “band-gap”. Afterward, the excited

electrons lose the charges and in the same process create the electric potential, which is a storable energy format thus concludes the energy production. The capability for a semiconductor material to produce voltage and electric current upon the exposure of light is defined as having the photovoltaic effect.

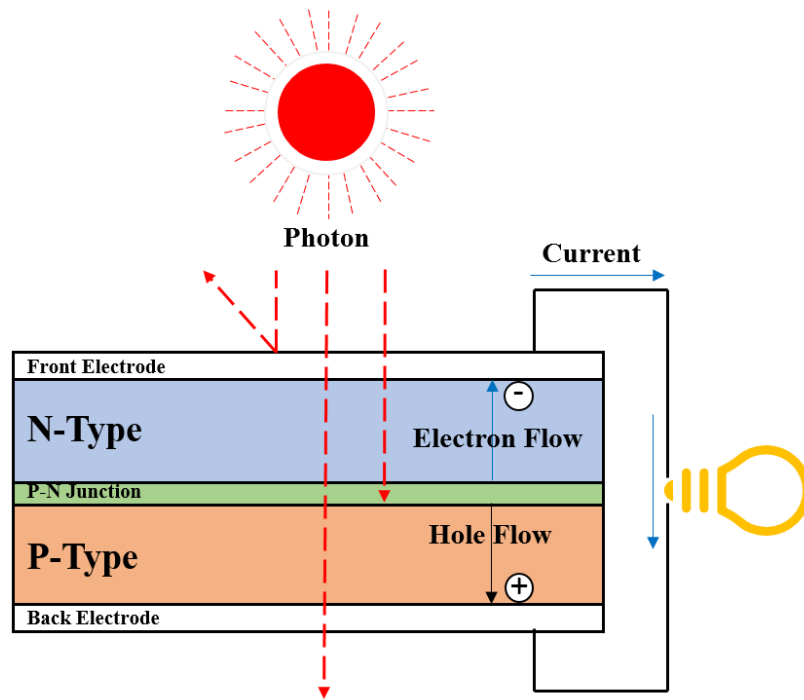


Figure 1.1. Schematics of a typical solar cell and photovoltaic Effect.

While the radiation of sunlight technically covers a much wider range of the electromagnetic spectrum, typically only the photons within the wavelengths in the visible region are applicable to the typical silicon photovoltaic cell designs for many reasons. In principle, photons with energy lower than the band-gap tend not to be absorbed. The photons with energy higher than the band-gap could be absorbed by a photovoltaic material in theory, but the exceeding energy is not be absorbed and released as heat instead due to the thermalization of the

photon energies. As a result, the energy of capturable photons ranges for a typical silicon-based solar cell roughly corresponds to photons of the visible regions, as shown in Figure 1.2, which occupies 400 to 700 nm in the electromagnetic spectrum³. Between the non-absorption photons and the photon energy lost to thermalization, the theoretical maximum efficiency has been calculated to have the loss of approximately 50% of the sunlight radiation could be absorbed and converted into electricity³.

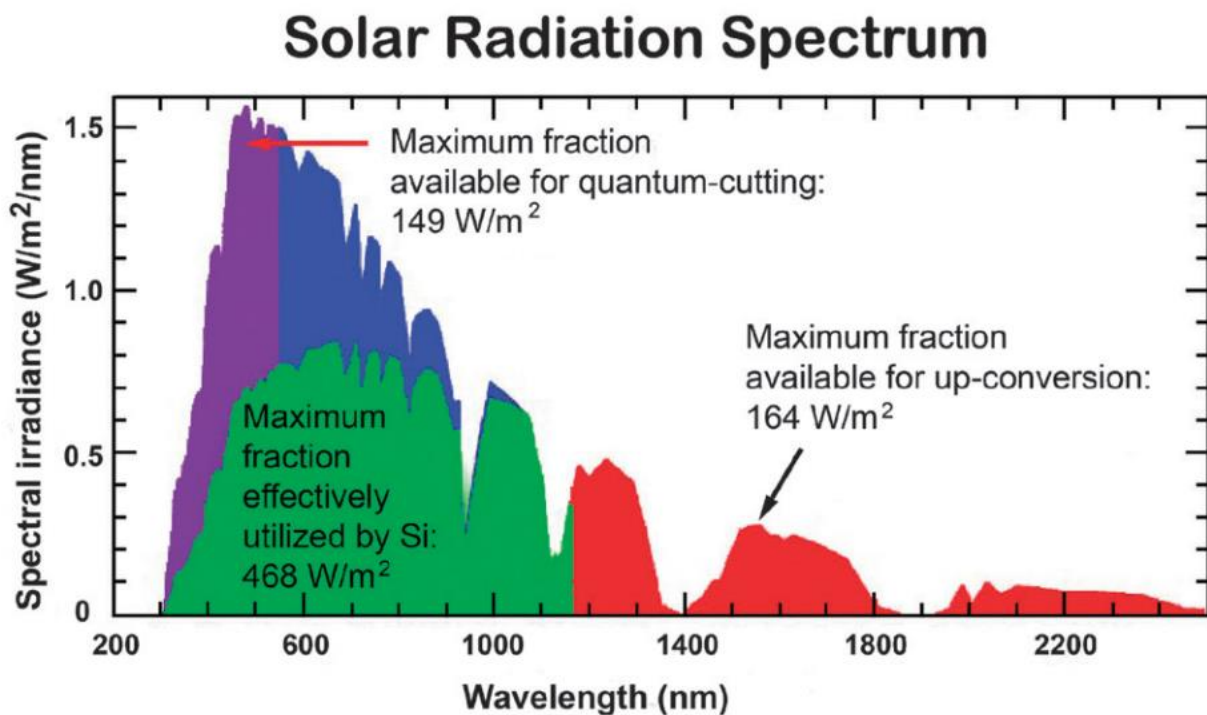


Figure 1.2. Effectiveness of a typical silicon-based solar cell in respect to solar radiation spectrum³.

Of course, there are also many other environmental factors to consider when it comes to solar cell efficiency, such as unfavorable climate and low average time of daylight of a specific area where a solar panel is installed, effectively decreasing the performances and even the

lifetime of the solar panel itself. These limitations are more of the reason why the band-gap of a photovoltaic material tends to be the first and primary property to be considered when examining the potential of a new photovoltaic device. Since if the band-gap value is not useful to begin with to perform in a laboratory condition, where all interferences are null, then there is little that can be added during processing to make the material perform better in a real-world scenario.

1.3. Summary on Solar Cell Classifications

The research and development for photovoltaic materials has covered significant grounds and been classified into three generations thus far. The first-generation solar cells are mainly based on silicon crystalline wafers and have been dominating the market traditionally with reliable efficiency and stability^{4,5,6}. The second-generation solar cells are the lightweight thin-film devices based on amorphous silicon and the semiconductor compounds in nanocrystal structure including the cadmium telluride (CdTe) and copper indium gallium sulfide (CIGS)^{7,10,11}. Finally, the third-generation solar cells have been exploring the new field of utilizing polymers and organic molecules to create the organic solar cells and has seen the least commercial backing out of the three generations due to the high production cost, low stability and low efficiency some of the generation three materials have been performing⁵.

1.3.1. Silicon-based Photovoltaic Materials

The silicon solar cell, being the first-generation solar cell, is a bulk material that has been widely commercialized for its low cost, high efficiency and high stability. They are separated into three types based on their respective crystalline structure, the single-crystal, the polycrystalline, and the amorphous silicon solar cell. The single-crystal silicon, by definition, refers to those solar panel consists of a single and pure silicon crystal, meaning with the better material parameter but, at the same time, more expensive to manufacture. The single-crystal silicon solar cell generally speaking can outperform the other two types of silicon solar cells. Taking the single-junction solar cells for example, as organized in the semi-annually solar efficiency report organized by Green et. al., the highest recorded efficiency for a single-crystal silicon solar cell is 26.7% by the Kaneka Corporation in 2017^{4,5}. The polycrystalline silicon solar cells are made of multiple silicon crystals thus has lower efficiency, highest efficiency reported in the same category is 22.3% by Benick et. al.⁶. Slightly lower due to the electrons transfer lost caused by junctions between multiple crystals. Despite that, the polycrystalline type of silicon solar cell has enjoyed tremendous commercial success and is the product a customer typically will purchase in a solar panel retailer. The amorphous silicon solar cell, being the herald of the second generation of solar cells, is similar in concept with the polycrystalline silicon solar cell as both deploys multiple crystals conjoining in the same structure, but the amorphous silicon solar cell has only a fraction of the amount of crystals when compared to the polycrystalline counterpart. The smaller number of crystals deployed gives the amorphous silicon a commercial edge for being significant cheaper and lighter, a very much desired property when it comes to application. The amorphous silicon solar cell does perform the lowest in efficiency, with the

highest reported being 10.2% by the National Institute of Advanced Industrial Science and Technology (AIST)⁷. The development of the amorphous silicon solar cell marked the one of the first steps into the direction of downscaling the photovoltaic devices, which has blossomed into an entire industry of its own over the past decade.

These silicon solar cells have become a staple of clean, renewable energy as more have been set up around the world on the rooftops of residential housings, commercial districts, traffic signs on the highways, to the solar panels supplying power to various satellites and the International Space Station. Indeed, the single crystal silicon solar cell has seen a wide and thorough implementation as a clean, renewable energy source alternative to that of fossil fuels; yet, its utility is significantly limited by the heavy weight and tremendous sizes that comes with its structure, a grave disadvantage that even the design of amorphous solar cell cannot properly solve. As neither lightweight nor downscaling seem possible to the silicon in the near future, some of the focus in solar research has shifted to the nanoparticle based thin-film solar cell design as an alternative.

1.3.2. Nanocrystals-based Thin-Film Photovoltaic Materials

Trying to away from the many burdens and limitations of the bulky and heavyweight silicon crystalline wafer based solar cells the scientific community has put much focus on the thin-film solar cells. The development of the thin-film devices utilizes nanoparticle based photovoltaic materials marks the second generation of solar cells. The thickness of the thin-film varies by design and could be conceived from a few nanometers (nm) to the scale of micrometers

(μm). The small thickness is crucial as it leads to high absorption of the sunlight, small diffusion length, and high recombination velocity. The direction to move to low weight and high flexibility is another great departure from the traditional first-generation solar cell. As oppose to growing bulk size single crystals like the silicon solar cells, which would be counterproductive to the goal of downsizing of the thin-film solar cells, the latter utilizes nanoparticles as its main absorber material and can deposit the material through various means. Nanoparticle is defined as the “ultrafine particles” that the size is measured to have the diameters between 1 to 100 nm and typically refers to inorganic materials in this scale. Besides the obvious benefits of downscaling the product in both weight and size, nanoparticles have been in the center of attention of chemists and material scientists for this scale serves as a bridge connecting the bulk and atomic or molecular materials, as the property change of the same material can occur just by downsizing said material from bulk to nanoscale. Typical examples of the types of change of properties entering the nanoscale include the increasing mechanical strength and lowering the activation energy required to initiate a reaction.

A thin-film solar device is typically consisted of multiple layers of different types of material to achieve the photovoltaic effect⁹. From the bottom to the top, in the order of the types of material deposited onto the device, a typical thin-film solar device consists of a substrate, a back-contact layer, a p-type layer, an n-type layer, a transition layer, a top contact layer, and finally an optional anti-reflective or contact layer. A substrate, as the base of the entire solar cell, tends to be made of glass, alumina, or any material that’s lightweight, strong yet not conductive naturally because its purpose is only going to be a base support of the rest of the layers on top. The substrate tends to have a thin of back contact layer pre-coated on top prior to the

manufacturing of the thin-film device⁹. Typical back contact layer materials are molybdenum (Mo), zinc oxide (ZnO), indium tin oxide (ITO), and fluorine tin oxide (FTO). A back-contact layer needs to have excellent conductivity, as it not only serves as one of the two outlets that connect the thin-film solar device to the exteriors, but it also connects directly to the entirety of p-type layer, which serves as the main absorber that the photovoltaic effect is going to perform at. The p-type, known as the positive-type layer, is then directly adheres to the n-type, also known as the negative-type, which is designed and doped to have be more electron-rich, more negatively charged, when compares to the p-type. The physical contact of the p-type and n-type layers is termed the junction, a barrier of the two materials that no electron can freely travel under normal circumstances, unless photons pass through. The primary purpose of the p-type layer is then to capture photons from the sunlight as it passes through the layer, absorbing its energy of the photons and transferring to the electrons, which then causes excitation of the electrons and charged carriers that then transfer to the n-type material. Such flow of electrons passing from the p-type to the n-type layers is the electron flow, or the electric current, created by the photovoltaic effect. The charged electrons entering into the n-type layer leaves the photovoltaic device through the top contact layer into the circuit, which becomes the electricity that can be utilized and stored for future use.

One of the first non-silicon based photovoltaic material is the CdTe (cadmium telluride). The research on CdTe as a candidate of photovoltaic material first began in the 1960s due to the interest it has garnered with the high absorption property with the ideal direct band gap of 1.45 eV, which has been calculated to be near the optimum for converting sunlight into electricity⁹. Over the years, the CdTe has shown great promise with its high efficiency, highest

reported as 21.0 % as of 2014 by First Solar, and its low-cost production that's very tempting to newfound companies and investors, and it has climbed to the second most utilized solar material just behind single crystal silicon at one point¹⁰. Yet, the induction of cadmium, a known carcinogenic element that has caused widespread pollution and consequential to death and diseases in the early 20th century, is in direct contrary to the very goal of searching for a clean energy alternative and safe to use consumer product¹¹.

1.3.3. Copper Chalcogenide-based Thin-Film Photovoltaic Materials

The copper chalcogenide poses as a replacement for the carcinogenic CdTe, with the CuS (copper sulfide) as the next photovoltaic material. The term chalcogenide describes the species including the elements, sulfur (S), selenium (Se) and telluride (Te). Copper chalcogenide is the umbrella term for all of the compounds, with or without the induction of other elements, that are copper and chalcogenide elements based. Despite also been speculated to have excellent direct band-gap of 1.55 eV, CuS does not enjoy the same high efficiency displayed as its predecessors. Instead, the potential for copper chalcogenide as photovoltaic material series with the doping of rare metals indium (In) and gallium (Ga) has shown great promises in promoting better photovoltaic properties. One of the most successful copper chalcogenide based solar cell is the copper indium gallium sulfide (CIGS, $\text{CuIn}_x\text{Ga}_{(1-x)}\text{Se}_2$), and it has quickly become one of the most well-known second generation solar cell material and has seen much of the popularity and commercial success as the CdTe. As CIGS has been reported to perform with high efficiency, recently at 22.9% efficiency by Solar Frontier in 2017, as well as being a cleaner and more user-

friendly material when in comparison to CdTe¹². It is classified a quaternary copper chalcogenide that consists of four elements, copper, indium, gallium and sulfur. However, the less earth abundant nature of the rare metals, indium and gallium, has seen a huge price hike in recent years, leading to the higher cost in production, which has proven to be an enormous barrier to commercial success¹¹. Despite the tremendous interest initially displayed by both the academia and the photovoltaic industry, the CIGS, while still at the center of attention, does not enjoy as much as prestige anymore. The lesson learned from CIGS and CuInSe₂ is the doping of other metals into the copper chalcogenide has proven to be a successful and meaningful approach to promote the efficiency and stability, yet the use of high cost materials could severely limit the potential research and development of said photovoltaic material. The search for low-cost yet efficiency competitive alternatives remains the focus for the scientific community.

1.3.4. Iron Chalcogenide-based Thin-Film Photovoltaic Materials

Iron chalcogenide as a photovoltaic material was developed as a concept to address to the issue of high-cost of production that was seen in the development for copper chalcogenides. Iron chalcogenide is defined as any compounds made up with iron and the chalcogen atoms, S, Se, and Te. One iron chalcogenide has garnered great interests recently is iron pyrite. Iron pyrite, also known as iron disulfide, is a mineral with the chemical formula of FeS₂. It is also famously known for the nickname “Fool’s Gold” due to its similar appearances to gold nuggets fooling many gold prospectors during the California Gold Rush in the 19th century. As it turns out, FeS₂ has excellent light absorption, good electron mobility and carrier diffusion length on top of the

the useful direct band-gap reported to be 0.95 eV^{13,14,15}. In addition, iron pyrite is the most earth abundant sulfide mineral, which in itself is a huge advantage with the promise of low-cost of production compare to the copper chalcogenides and other materials, thus, as a result, is an economical choice that has caught the attention of many in the scientific community as a cheaper alternative photovoltaic material moving forward¹⁶. FeS₂ is also a very environmental and user-friendly material as it does not contain any elements of toxicity nor carcinogenicity unlike its predecessor CdSe¹¹.

With all its promises, recent publications have confirmed numerous poor performances made with the FeS₂ based photovoltaic device, and it has to do with the factor that it is an extremely unstable material. First, FeS₂ is known to be extremely moisture sensitive and prone to oxidize to produce rust, iron oxide (FeO₂), and sulfate (SO₄²⁻). In addition, the material is extremely easy for the FeS₂ structure to collapse under the slightest temperature changes, and generate other S-deficient binary phases, which tend to have inconsistent band-gaps, electronic and magnetic properties^{15,16}. The proposal to address these shortcomings including the phase instability have been primarily focusing on either designing a route to obtain phase pure pyrite or to identify new iron chalcogenides as new photovoltaic materials. To answer the shortcomings of FeS₂ pyrite's spontaneity of decomposing into the S-deficient phases, Yu et. al. in 2011 had proposed an olivine structured iron chalcogenide by adding a third element, such as silicon (Si) and germanium (Ge), to produce ternary iron chalcogenide variants as a replacement of the original binary FeS₂, to produce the iron silicon sulfide (Fe₂SiS₄) or the iron germanium sulfide (Fe₂GeS₄) respectively¹⁷. The third element would provide strong covalent bonding with sulfur, creating a much more stable compound than the binary FeS₂ that is prone to decompose under

moderate temperatures. The olivine structure provided Fe_2SiS_4 and Fe_2GeS_4 the same six-coordinate environment for the Fe^{2+} cations as pyrite, but a change to the sulfide anions from the disulfide S_2^{2-} to simple sulfide S^{2-} was calculated to have provided the stability against decomposition into iron or silicon (or germanium) binary phases. Both ternary compounds have been theorized to have exceptional direct band-gap, with 1.55 eV for Fe_2SiS_4 and 1.40 eV for Fe_2GeS_4 , which is about 0.4 eV higher than the FeS_2 pyrite band-gap is thus more advantageous with respect to absorption of photons¹⁷. The increase in thermal stability, the absence of phase coexistence and separation into smaller band-gap binary iron chalcogenide phases are also promising aspects that has put the two new iron chalcogenide compounds on the spotlight.

1.4. Solid-State Synthesis in Chemistry

Unlike the typical solution-based synthesis in material chemistry that involves the reaction materials dissolved in solvents at elevated temperatures, a solid-state synthesis is a reaction route that utilizes mostly in solid phase inorganic materials. Recently, this type of synthesis has gained traction with the scientific community due to the facile and robust nature of these reactions are often involved in. A solid-state synthesis is often the subject of more physics-based inorganic materials in nature, such as ceramics, mineralogy, and metallurgy. Unlike the solution-based synthesis that often work with organic materials and solvents, and therefore typically operates at low to moderate temperatures, a solid-state synthesis would often involve in temperature as low as the upper hundreds for a gas reaction, such as the chemical vapor deposition (CVD) or the chemical vapor transport (CVT), as shown in the exemplar

schematics in Figure 1.3, and as high as in the thousands for an oven reaction, such as an annealing procedure.

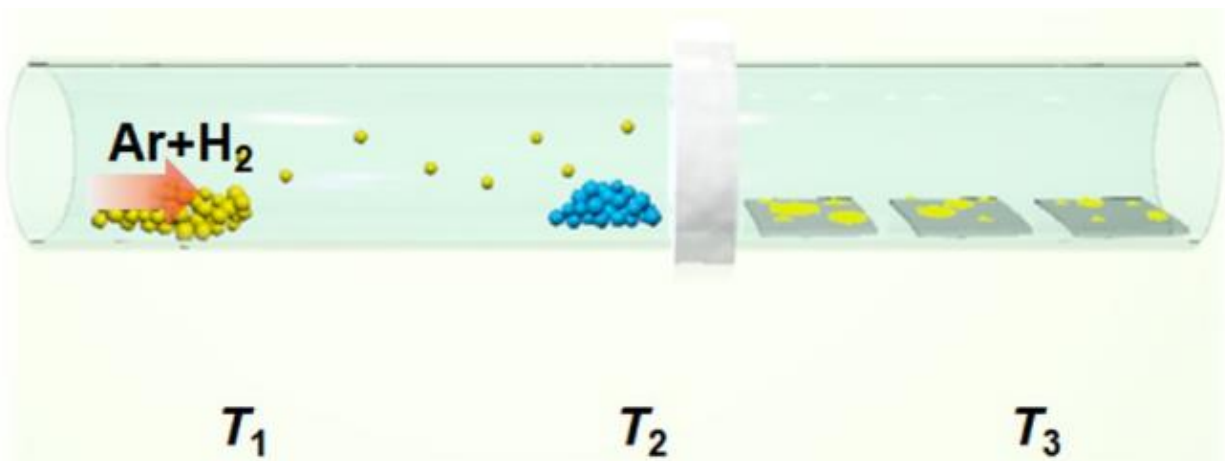


Figure 1.3. Schematic of a typical chemical vapor deposition in a tube furnace¹⁸.

The factors that strongly influence the rate of a solid-state reaction are, the surface area of contact between the solid reagents, the rate of diffusion, and the rate of nucleation. Diffusion in solid-state synthesis is the reaction leading toward the defect phase in order to decompose the precursor solids into reactants that can be utilized for the synthesis itself, it is often controlled by the increase in temperature in the synthesis. Nucleation is defined as the creation of the new product phase and can be optimized by utilizing precursor solids with similar crystalline structure to the final product with either the topotactic transformation and the epitaxy reaction. The topotactic transformation is the mixing and displacing of atoms within a crystal structure and the initial crystal lattice will be consistent with the final crystal lattice due to the balanced loss or gain of material. The epitaxy reaction is the growth of one crystal phase on the face of another

crystal that have the same structural orientation, which is typically seen in deposition of one material onto a target substrate.

CHAPTER 2. LITERATURE

2.1. Iron Pyrite Thin-film Syntheses and Challenges

Methods of synthesizing iron pyrite photovoltaic cell have changed drastically over the past decades. Bulk iron pyrite as a photovoltaic material has been demonstrated by Ennaoui and Tributsch in 1984 in the form of photoelectrochemical and Schottky solar cells¹⁵. The bulk iron pyrite was synthesized by placing an electrode in an aqueous electrolyte and different crystal stoichiometric profiles could be obtained according to the specific growth conditions, and this synthetic pyrite grew as large as 1 cm² in dimension¹⁵. Even though only products with poor purity could be obtained, the devices synthesized with this method had regardless proven the possibility of using pyrite has the capability of performing the photovoltaic effect¹⁵.

A continuous study by the same research team had deployed chemical vapor transportation (CVT) to prepare iron pyrite photoelectrodes by annealing the iron and sulfur elemental powders and additions of small amount of halogen acting as mineralizer and transport agent to fasten the reaction¹⁹. Despite the build-up of thin-layer of iron oxide on the electrode surface, Ennaoui et. al. managed to produce monocrystalline n-type FeS₂ photoelectrode products with high photocurrent quantum efficiency and high electron mobility, yet the solar device did not perform well overall due to the small photopotential and the low effective carrier density. The development of bulk iron pyrite photovoltaic device in the 80s, despite the exceptional quantum efficiencies of over 90% and good photocurrent observed, the performance was overall plagued by the low photovoltage^{14,15,19}.

The first published pyrite thin-film was developed by Seehra et. al. in 1979 via evaporation method, but the group did not conduct any characterization with respect to the phase composition and photovoltaic properties²⁰. The concept of pyrite thin-film solar cells was developed in the late 80s and early 90s and had quickly become an attractive topic of research as it not only conserve material, but it also provide a path to high efficiency through efficient charge separation corresponded to the high internal electric field^{17,21}. Smestad et. al. explored the options to synthesize iron pyrite thin-films with other techniques, which included metal organic chemical vapor deposition (MOCVD), chemical spray pyrolysis (CSP), and chemical vapor transport (CVT) and managed to synthesize a thin-film with thickness of 0.1 to 0.2 μm . Yet, poor performance and great amount of impurity was observed. This was concluded that the presence of S-deficiency sites with the stoichiometry of $\text{Fe}_{1-\delta}\text{S}$, which generated less favorable band-gap with defect band, had caused the decrease in barrier height and photovoltage in the solar device²². Building on the previous study, the same research group conducted sulfurization of iron oxide (Fe_3O_4 or Fe_2O_3) layers and had produced good quality films with good crystallinity and purity in addition to the photoconductivity and photoelectrochemical response, albeit small photocurrents and photovoltage observed¹³. Further improvements on the iron pyrite thin-film's crystallinity, phase composition as well as the morphological characters were made in a publication by Hopfner et. al. by employing a low-pressure metalorganic chemical vapor deposition (LP-MOCVD), but it was determined that no significant differences of the electrical properties were observed, which the cause was assigned to the lack of grain growth following the reaction²³.

Solution processing to synthesize iron pyrite colloidal materials began in the recent decade. In 2010, Puthussery et. al. proposed to use iron pyrite nanocrystals as the base material for the ink that would be utilized for dip-coating processing, an inexpensive method suitable use with nanocrystal ink. Puthussery's research has been focusing on the understanding the grain growth mechanics and the realization of surface passivation technique on the iron pyrite films, with the main goal being to showcase the possibility of inexpensive, high manufacturing scalability pyrite films with colloidal nanocrystals as the base material¹⁶.

Puthussery presented a hot-injection synthesis of the colloidal pyrite nanocrystals at that was then purified using the standard precipitation and suspension techniques to obtain phase pure colloids. It was noted that the attempt to disperse the colloids in chloroform would be unsuccessful due to serious aggregation as the result of the unsuitable ligand used for the reaction. Initial preparation of the ink was unsuccessful due to the serious aggregation, which could be reversed by undergoing a partial ligand exchange. The ink was utilized in the layer-by-layer dip-coating process of and then sintered in sulfur atmosphere at the moderate temperatures of 500 – 600 °C, upon which a larger grain crystalline film could be obtained. It was reported that the average grain size post sintering was ~300 nm in diameter, which was a significant increase from the 5-20 nm colloids previously. Aside from the benefit of significant grain growth, the sintering process was also designed to reduce the S-deficiency problems shown previously in the bulk device and to remove carbon and to densify the film^{13,14,15,19,22}. Though a byproduct from the grain growth, the densifying of the thin-film is still important to reduce grain boundaries within the polycrystalline structure, which helps to reduce the loss of electron transport and increase efficiency. However, as shown in Figure 2.1, Puthussery had observed the

roughening up of the film surface and with it the formation of voids across the film surface¹⁶. It was concluded that the sintering employed, while it does provide the increase in grain size, the poorer intergrain connectivity and substrate coverage posed a challenge for future iron pyrite research. Providing a higher sulfur partial pressure during the sintering could provide the better grain connectivity, thus the less formation of voids in the film structure, while still retain the level of grain size increase that can also observed in a typical sintering procedure. Yet, sintering at a slightly higher temperature at 650 °C could become harmful to the material, as it was observed by Puthussery et. al. that pyrrhotite formation was observed at this temperature¹⁶.

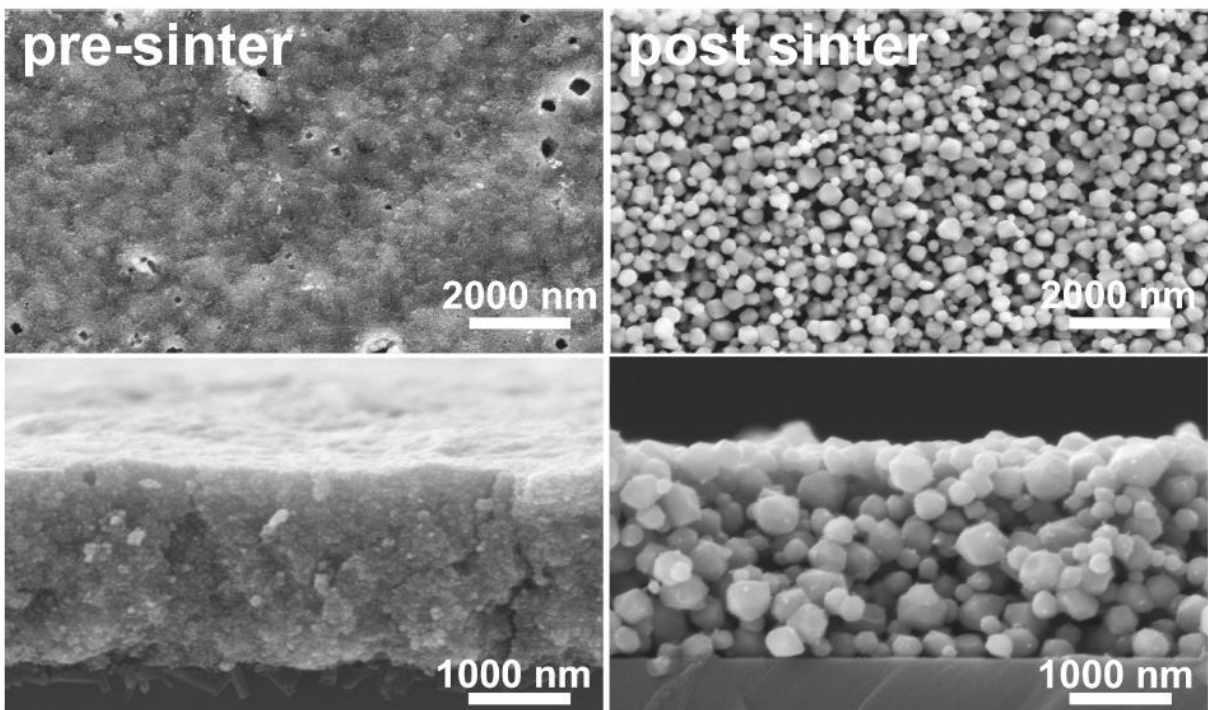


Figure 2.1. SEM images of a surface roughening by sintering of iron pyrite thin-film at 540 °C in sulfur vapor¹⁶.

The lack of stability of the FeS₂ pyrite films was also reported in the publication. As stated by Puthussery, the as-made pyrite NC thin-films without sintering could decompose within a few weeks under air as indicated by the drastic color change from gold to black. The color change most likely related to the phase pure FeS₂ phase's decomposition into the S-deficient impurity Fe_{1-δ}S phase. The sintered films held longer and could stay stable for at least a month in air without any color change.

With the latest iteration of iron pyrite thin-film processing technique, the scalability toward industrial level with either roll-to-roll printing or the dip-coating process is potentially very promising. However, pyrite's thermal instability to decompose under high temperature condition as well as the decrease in film quality post-sintering regardless of the atmosphere it is placed in seems to be an uncontrollable factor that could undermine the material's potential to be an effective photovoltaic material^{13,14,16,22,24}.

2.2. Challenges for Iron Pyrite as a Photovoltaic Material

Regardless of the many attempts to prepare pyrite thin-film solar cells, whether by vacuum processing or by solution processing, there have not been any significant progress made to produce a working solar cell that could match the predicted expectations^{13,14,15,16,19,22,23,25,26,27,28,29}. Many explanations and proposals have been put forward to address the shortcomings of the pyrite solar cells, which includes the stoichiometric instability, pyrite's synthesis conditions which is associated with phase instability, and the varying

dependence of conduction type on material's surface, crystalline size, and thin-film thickness^{16,24,25,26,27,28,29}.

2.2.1. Stoichiometric Instability of Iron Pyrite

The stoichiometric instability of pyrite could often be observed in the formation of S-deficiency sites on the surface of pyrite thin-film during thermal treatments, and were often proposed as the cause to undermine a pyrite solar cell's performance^{13,16,24}. The effect of the S-vacancy issue, however, and the effect of the S-rich sites to the stability, electronic structure and band-gap of pyrite surface was researched with a computational study by Zhang et. al. in 2012. With a layer by layer modelling, it was calculated that the electronic states for the first three atomic layers of a pyrite crystal would be localized and thus different to the rest of the crystal, which had bulk-like properties, including the electronic structure and band-gap. The S-rich sites on the surface generally had smaller band-gaps with less than 0.3 eV, which could be responsible for the poor photovoltage observed for pyrite solar cells in previous publication²⁶. On the other hand, S-vacancy sites had slightly more favorable band-gaps, thus was more favorable for fabrication to pyrite solar cells compare to S-rich sites. Yet, neither the S-vacancy nor the S-rich sites could reach the theoretical band-gap and electronic structure of the stoichiometric pyrite^{13,14,15}. Additionally, deliberately altering the stoichiometry of pyrite to compensate for the lower band-gap was discussed. With Hu's proposal to replace ~10% of the sulfur atoms in pyrite with oxygen atoms, it was calculated that the new iron sulfur oxide alloy could obtain better light

absorption in the near-IR region than pyrite itself, with the increase of band-gap from ~1.0 to 1.2 – 1.3 eV, while obtaining better thermal stability as well²⁸.

However, contradictory conclusions have been made about the facile formation of S-deficiency between different publications¹⁷. Analysis done by Ellmer and Hopfner have concluded that FeS₂ is a stoichiometric compound by nature, and the high formation energy required to form S-deficiency sites also support the idea^{30,31}. This contradiction has only served to decrease the interest on pyrite as a photovoltaic material. Yu et. al. thus had proposed the notion that pyrite's S-vacancy, which was theorized to occur naturally, should not be confused with the S-deficiency that could be caused by thermal instability¹⁷.

2.2.2. Phase Instability of Iron Pyrite

One of the disadvantageous traits that a FeS₂ thin-film photovoltaic cell faces is the phase instability issue^{17,24}. Each individual instability phases carry drastic differences in optical, electronic and magnetic properties compare to the original, phase pure FeS₂, further increasing the difficulty to obtain a consistent photovoltaic device with the theorized high-performance²⁴. The phase instability issue is not exclusive to just one specific pyrite morphology nor is it exclusive to just a specific thin-film device preparation method. In the bulk pyrite research work by Ennaouli et. al. utilizing crystal growth technique with electrochemistry, their associated products produced the impurity phase in the form of the iron oxide thin-layer generated on the electrode surface during the syntheses^{15,19}. Chemical vapor deposition methods under high temperature condition generally produced impurity phase in the form of S-deficiency sites on the

thin-film surface^{13,14,16,22,24}. The differences between the two types of impurities was that the oxide impurity was concluded to be associated with the etching treatment as an effort to polish the electrode surface. On the other hand, the generation of the S-deficiency sites was the result of thermal instability causing sulfur to leave the pyrite lattice, which in turn led to the conversion from FeS₂ to Fe_{1-δ}S in order to conserve charge neutrality and the conversion from the point group O_h to C₄^{13,16,32}. The lack of defect observed in the superstructure has led to speculation that a homogeneous distribution of S-deficiency sites should be assumed³².

To better understand the cause and effect of the phase instability of FeS₂, Zhang et. al. (2015) proposed a systematic study to examine the effect of temperature has on the as-synthesized FeS₂ thin-film samples²⁴. These films that have undergone the single temperature vacuum annealing were then analyzed by WAXRD, SEM/EDS, Raman spectroscopy, electronic transport and magnetometry. The WAXRD reveals a very clear picture of the effect of temperature on FeS₂ phase stability. Figure 2.2, shown in Zhang's report, displays the results of WAXRD, SEM/EDS, and Raman Spectroscopy across the different vacuum annealing temperature settings²⁴.

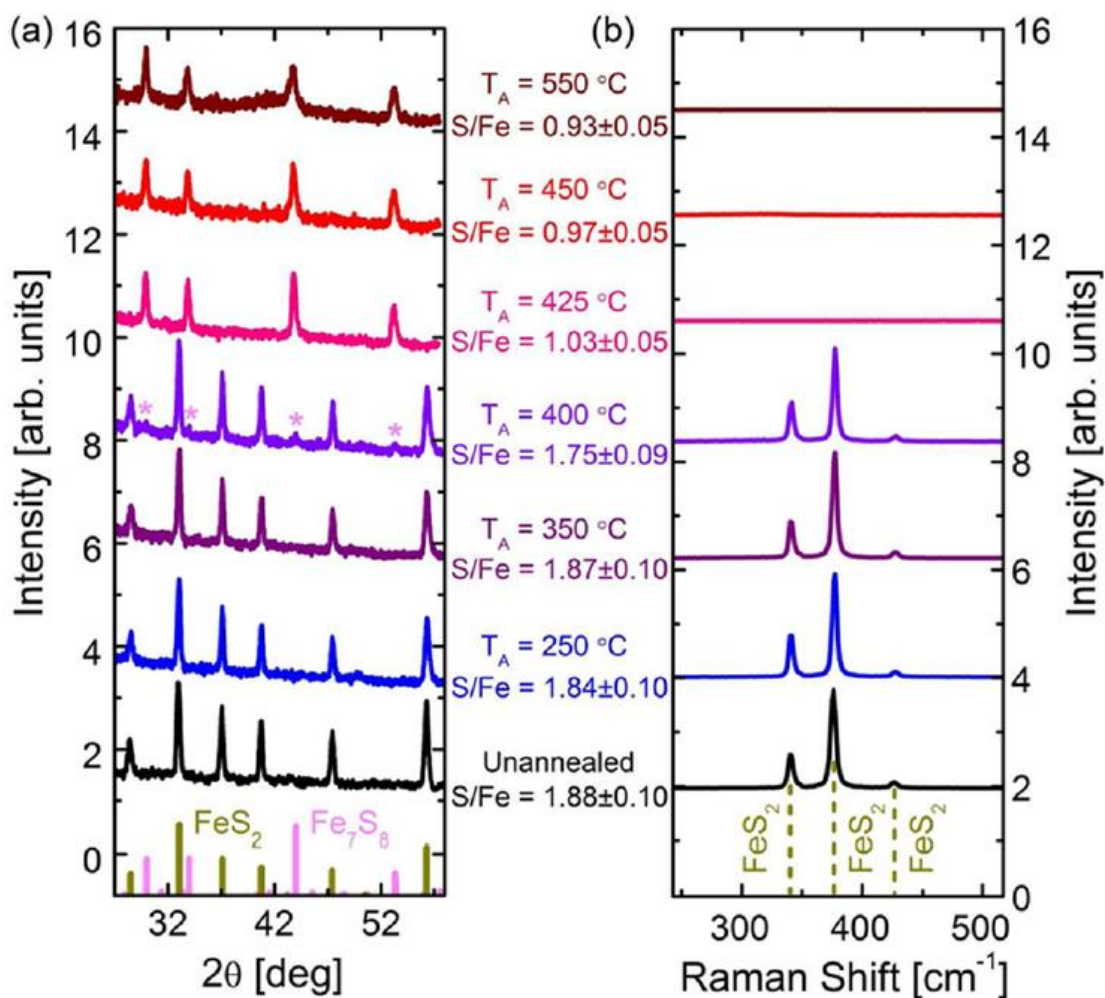


Figure 2.2. (a) WAXRD, (b) Raman spectrum, and EDS Ratio of pyrite sample phase changes with increasing vacuum annealing temperature²⁴.

The unannealed sample displays in the figure has shown only the phase pure FeS₂ spectra. The phase purity largely stayed the same until the vacuum annealing temperature reaches 400 °C, where the Fe₇S₈ impurity peaks began to surface. At 425 °C, it was observed that FeS₂ phase peaks had all disappeared, leaving only the Fe₇S₈ impurity peaks on the XRD pattern from 425 to 550 °C. The Raman spectrum shows a similar story, as the peaks identifying the presence of FeS₂ were present from the unannealed sample to 400 °C annealed sample, yet the same peaks

quickly vanished as the annealing temperature approached 425 °C and stayed this way until 550 °C, indicating the lack of presence of FeS₂ from that point forward. Zhang et. al. thus concluded there's a sudden and drastic reduction of FeS₂ pyrite and rapid formation of Fe_{1-δ}S pyrrhotite occurring between 400 °C and 425 °C from these findings²⁴.

Given that the X-ray Photoelectron Spectroscopy is a surface-specific sensitive analysis tool, Zhang and his group set out to collect the change FeS₂ pyrite film surfaces following the increase in vacuum annealing temperature²⁴. Minor amount of Fe_{1-δ}S pyrrhotite was observed to form on the FeS₂ pyrite film surface at the vacuum annealing temperature as low as 160 °C as a minority phase. The development of the Fe_{1-δ}S pyrrhotite phase rapidly increases from 380 °C to 410 °C as a complete conversion from pyrite to pyrrhotite taking place and making the latter the majority phase of the annealed film sample, shown in the complete change of XPS spectrum in Figure 2.3(a). The sudden increase in Fe_{1-δ}S molar fraction and overtaking as the majority phase near 400 °C, as shown in Figure 2.3(b), agrees with the previous assessments. The development of Fe_{1-δ}S beginning on the surface and between grain boundaries was in consistent with previous reports also^{13,14,16,22,24,32}.

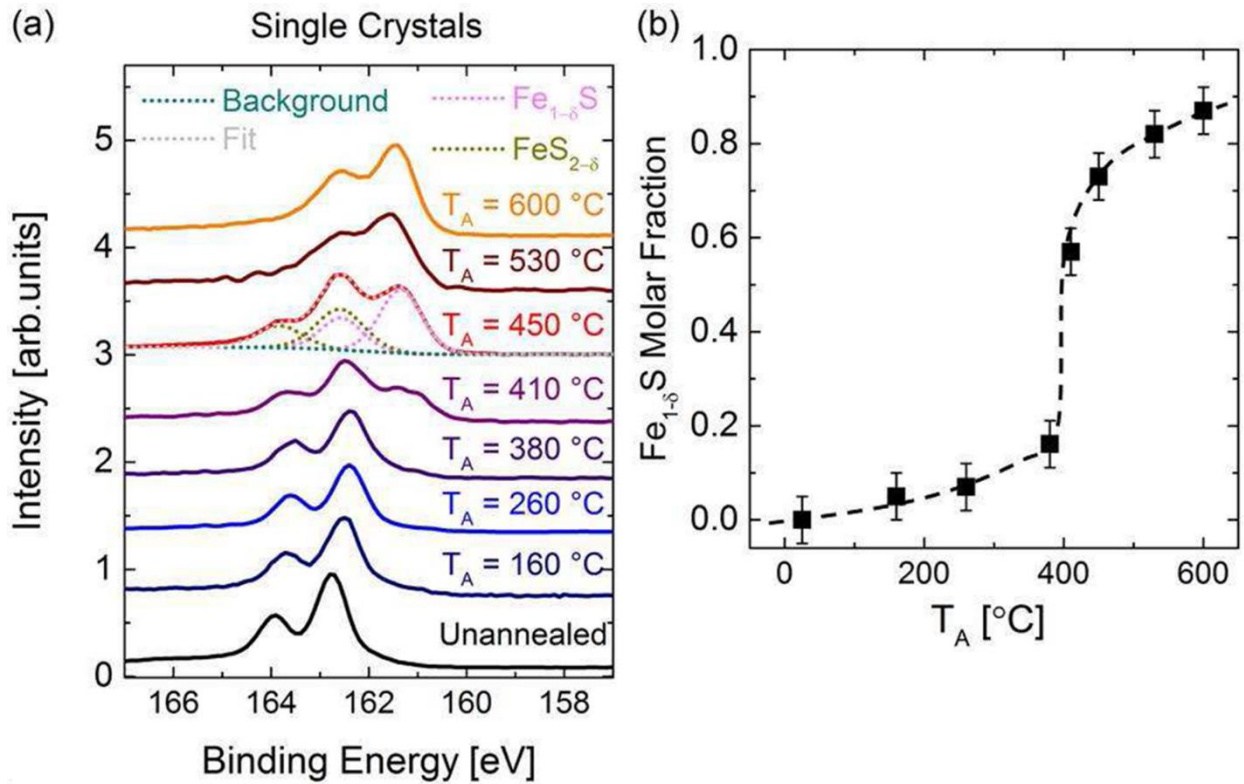


Figure 2.3. (a) XPS spectrum and (b) Fe_{1-δ}S molar fraction showing the adverse effect of increasing in vacuum annealing temperature to phase purity²⁴.

The same single crystal film samples also underwent analyses to determine the electronic and magnetic properties. It was discovered by Zhang (2015) that the resistivity changes for samples until 400 °C has only relatively small changes and stayed semiconductor-like behaviors, but increasing between 400 °C to 425 °C sees a sharp decrease in resistivity, which is consistent with Zhang's previous discoveries of the rapid development of Fe_{1-δ}S pyrrhotite phase as it was already known pyrrhotite phases have metal-like behaviors, which are good conductors with low resistivity²⁴. Further analyses were conducted utilizing the Zabrodskii plots, which is commonly used to determine the characteristic of the devices, with the $\ln W$, where W is the reduced activation energy, decreasing with the decreasing $\ln T$, where T is the temperature, marks the

characteristic of the metallic conduction of the metal-insular transition while the $\ln W$ increases with the decreasing $\ln T$ is the characteristic of the insulating conduction of the metal-insular transition. Zhang's analysis has shown that samples with the vacuum annealing temperatures above 425 °C has the $\ln W$ values increases with the $\ln T$, a behavior that signifies metallic properties and also consistent with the resistivity values obtained in the previous experiment²⁴. With the combining results, Zhang concluded that the $\text{Fe}_{1-\delta}\text{S}$ pyrrhotite phase, the metal-like phase of the scope of this experiment as oppose to the FeS_2 pyrite phase which is more semiconductor-like, is the majority phase that has developed rapidly between 400 °C to 425 °C²⁴.

Lastly, on the examination of the magnetic properties, it was observed that a drastic change at 350 °C, as shown in Figure 2.4(a), occurred and changed the material's behavior to an electron-like material, thus signaling the change from a p-type, a typical pyrite behavior, to a n-type conduction, which is a typical pyrrhotite behavior. At Figure 2.4(b), the conductive nanoclusters were observed after 425 °C, which was indicative of the presence of $\text{Fe}_{1-\delta}\text{S}$ pyrrhotite impurity phase as it has the ferromagnetic property, indicative of pyrrhotite's metallic behavior. This is in direct contrast to the pure FeS_2 pyrite that is known to have negligible magnetization. Interestingly, Figure 2.4(c) shows samples at 550 °C and beyond shows a significant magnetization drop, falling back to negligible level like prior to 400 °C, which Zhang had pointed out could be the indicative antiferromagnetic FeS troilite phase forming. This trend is in agreement with the development of S-deficiency sites on the thin-film surface observed in previous publications^{13,24}.

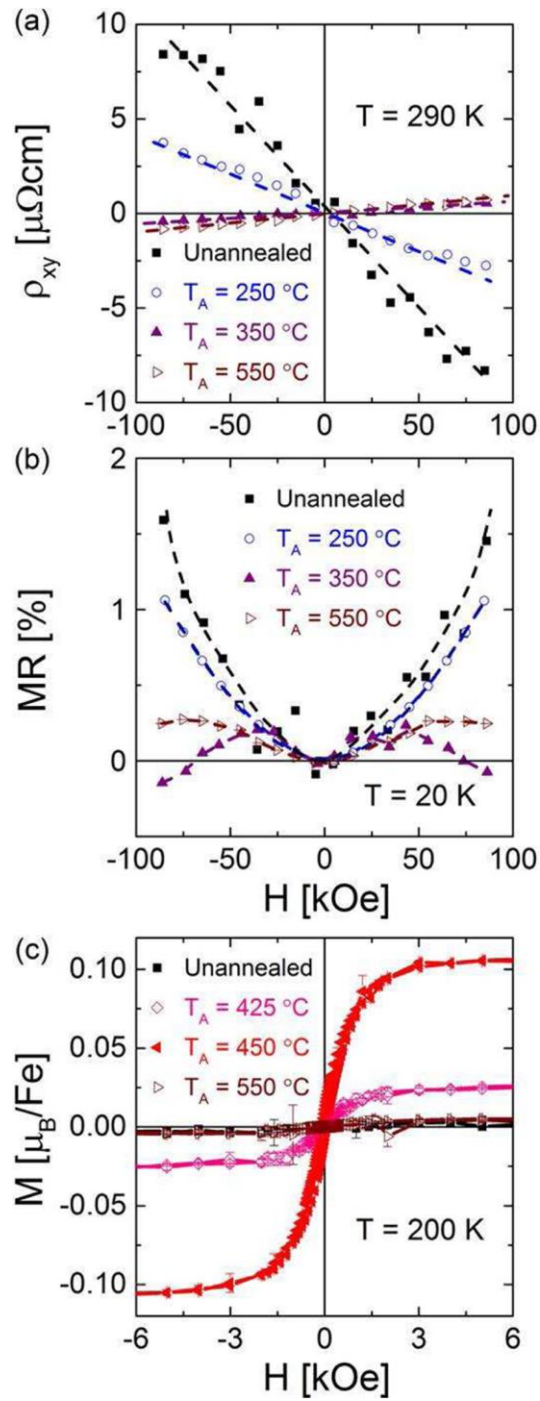


Figure 2.4. Effect of increasing vacuum annealing temperature versus (a) the Hall resistivity (ρ_{xy}), (b) the magnetoresistance (MR) and (c) the magnetization hysteresis loops of similarly produced FeS₂ films²⁴.

The rapid development of $\text{Fe}_{1-\delta}\text{S}$ pyrrhotite phase taking over as the majority phase began above $400\text{ }^\circ\text{C}$, but the onset of the pyrrhotite formation on the surface can begin as early as $160\text{ }^\circ\text{C}$. While it is unlikely that a photovoltaic device will ever experience temperature as high as $160\text{ }^\circ\text{C}$ during typical operation in an ambient temperature, the temperature in fact can be easily achievable during processing. As a matter of fact, the very experimental method Zhang has conducted in the report is sulfurization, which is a typical processing method aiming to increase grain sizes and reduce loss of electron transport via annealing at high temperatures²⁴. If a phase pure FeS_2 pyrite film cannot survive the sulfurization processing, it decreases the possibility to get the correct phase for the ideal photovoltaic effect with the theorized performances. In addition, the impurity phases tended to have disadvantageous electric properties, combined with the low photocurrent and photovoltage performances shown in the past reports featuring the iron pyrite thin-films, it should be speculated that iron pyrite might lack the capability to function properly as an efficient photovoltaic material^{13,14,15,16,19,22,24,32}.

2.2.3. Iron Pyrite's Dependence on Material Morphology

In addition to the stoichiometric and phase instability, pyrite's lack of photovoltaic performance was also attributed to the heavy dependence of the conduction types on the material's morphology. In a Hall effect measurement study, Limpinsel et. al. had revealed the presence of a hole-rich inversion layer at the surface of a pyrite single crystal that could be responsible for limiting the photovoltage commonly observed in pyrite solar cells due to the tunneling effect²⁵. Pyrite also changes the electronic properties with a significant degree with the

change in crystal morphology; for instance, Macpherson et. al. discovered with the decrease in pyrite thin-film thickness, a stronger resonant light scattering signal was measured, which was indicative of the ease with electronic coupling between particles²⁹. In addition, acquiring a pyrite nanocrystal with a specific orientation displayed different electromagnetic absorption properties when compared to the irregular nanocrystals and demonstrated electronic behaviors closer to theoretical values^{29,33}.

2.3. Proposal of New Types of Iron Chalcogenide Photovoltaic Material

To avoid the phase coexistence and the history of poor performances observed in pyrite solar cells, Yu et. al. had proposed a new class of ternary iron chalcogenide compounds that would involve doping silicon and germanium into the pyrite structure, thus producing the olivine structured of Fe_2SiS_4 and Fe_2GeS_4 compounds¹⁷. The inclusion of a third element would create a ternary compound to adopt an olivine structure. The new structure was theorized to be very stable with respect to decomposition into binary phases and would obtain excellent band-gaps of 1.55 and 1.40 eV for Fe_2SiS_4 and Fe_2GeS_4 respectively. Shown in Figure 2.5, the lack of secondary band-gap absorption character suggested the structure does not share the phase coexistence commonly observed in pyrite solar cells. Lastly, these ternary iron chalcogenides also guaranteed the earth-abundance and low-cost of production traits that came with their binary predecessor.

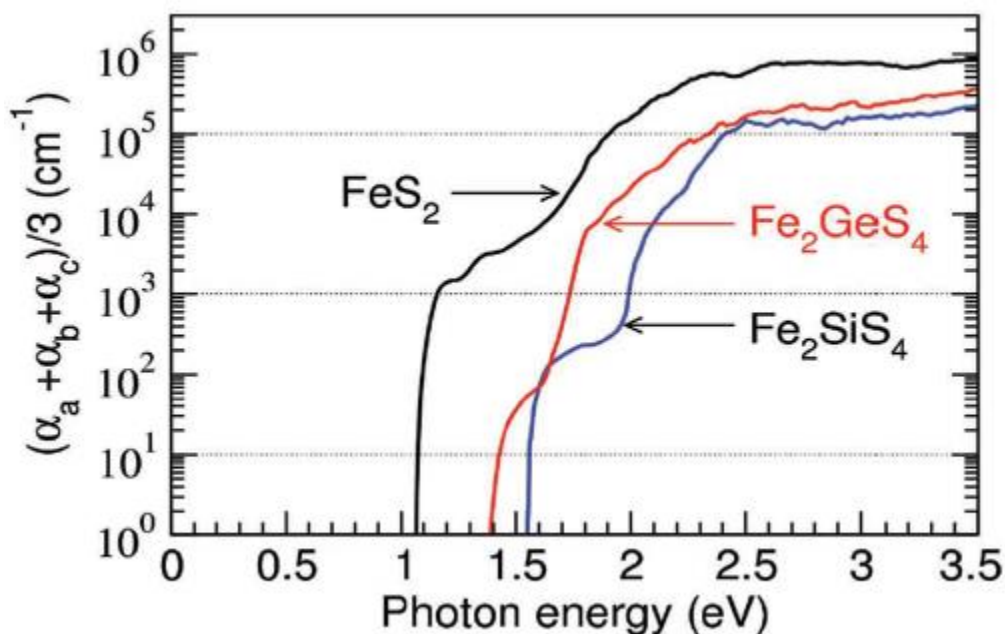


Figure 2.5. Calculated optical absorption coefficients for FeS_2 , Fe_2SiS_4 , and Fe_2GeS_4 ¹⁷.

2.4. Known Methods of Fe_2GeS_4 Syntheses

The proposal by Yu et. al. (2011) as the new class of photovoltaic absorbers had garnered new interests back to the field of iron chalcogenide solar research¹⁷. To date, a working Fe_2GeS_4 solar cell has been reported by fellow colleagues Liu et. al. with detections of low photocurrent³⁴.

2.4.1. Solution Synthesis of Colloidal Fe_2GeS_4 Nanocrystals

In 2013, Fredrick et. al. proposed a synthesis utilizing a typical hot-injection procedure that initially mixed a specific ratio of iron chloride (FeCl_2), germanium tetraiodide (GeI_4), hexadecylamine (HDA), and octadecene (ODE) at 320 °C in one pot. A mixture of

hexamethyldisilazane (HMDS) and hexamethyldisilathiane ((TMS)₂S) and ODE were injected, after which the system was allowed to react at 320 °C for 24 hr. Purification was done in a combination of acetone and hexanes to remove unreacted starting materials. Since the purpose of the colloids was to prepare ink for dip-coating processing, the colloid nanocrystal product was suspended in either hexane or toluene to obtain a light brown color solution. Afterward, the sample ink was characterized for XRD, XPS and TEM for phase stability and size distribution³⁵.

The ink was described to be very air-stable as the nanocrystals stayed suspended in solutions and no agglomeration was observed under inert atmosphere. Since the reaction needs to take place at 320 °C, GeI₄ was chosen as the germanium precursor for the higher temperature stability when compared to germanium tetrachloride (GeCl₄), which was observed to have left the reaction system in white residue covered the entire condenser column prior to reaching the reaction temperature³⁵. The design of the reaction temperature at 320 °C is critical as it was observed that only the binary phases, iron and germanium sulfides more specifically, were present if the reaction temperature was not met. The inclusion of HMDS was discussed to be important to obtain the desirable Fe₂GeS₄ product, but the mechanism involved was not understood. Using (TMS)₂S as a replacement of sulfur was also discussed to be vital because reactions with elemental sulfur would only end up synthesizing iron sulfides. The ratio of Fe:Ge:S was pointed out to be very crucial to a successful synthesis. The stoichiometric ratio of Fe:Ge:S = 2:1:4 would synthesize a mixture of Fe₂GeS₄ and FeS, but by increasing the germanium ratio to achieve the ratio of Fe:Ge:S = 2:1.5:4 could yield the phase pure product. Based on the XRD pattern, the Fe₂GeS₄ phase would begin to form at 1 h along with pyrite as the majority phase, and a phase pure product could be obtained at 24 h³⁵.

Based on the TEM, the nanocrystal products synthesized a plate-like structure of varying size and shape with a size distribution of 75.9 ± 30.9 nm. The deviation of the size is quite large, indicating a very inconsistent particle growth during the reaction. Fredrick et. al. (2013) has also observed the low reactivity of germanium with sulfur when compared to iron with sulfur, which the Fredrick group had concluded the planes containing germanium have slower growth rates overall and could have been the cause of inconsistent growth mentioned above.

Next, the Fredrick group had also conducted the air stability experiment by exposing the as-made Fe_2GeS_4 nanocrystals under ambient atmosphere for four different exposure times, 0, 2, 12, and 24 h³⁵. The 0 h represents the transferred for characterization without any exposure. These samples were characterized by X-ray Photoelectron Spectroscopy (XPS) to examine the binding environments of each element and the general trends that can be indicative of Fe_2GeS_4 's properties and stability under air. The Fe XPS data is shown in Figure 2.6, where many varieties of Fe binding environments as shown by the various peaks on the spectrum were observable even for the 0 h sample. This is indicative of the rapid oxidation of Fe species under air exposure, decomposing from the ternary structure down to the FeO phase³⁵.

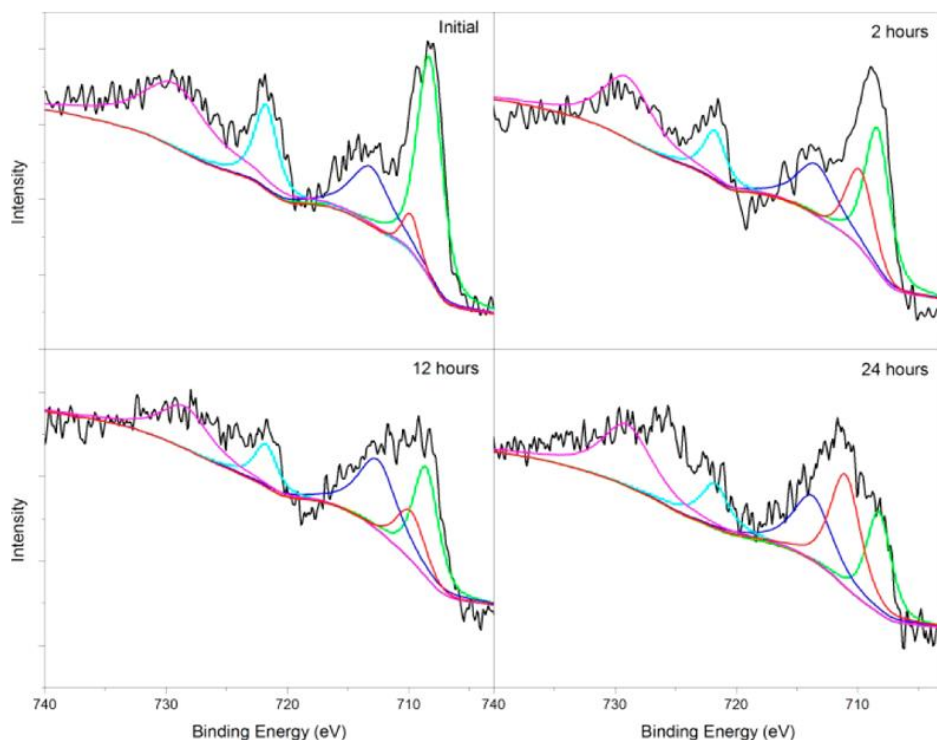


Figure 2.6. Fe XPS spectrum of the as-synthesized Fe_2GeS_4 nanocrystals from 0 h to 24 h air exposure³⁵.

The Ge XPS spectra shows a single peak at 0 h, indicating better binding at GeS_2 , but it quickly deteriorates into a mixture of two peaks that the Fredrick group had concluded to be germanium (IV) oxide (GeO_2) overtaking as the majority. TEM images of the exposed nanocrystals showed a significant growth of amorphous, oxidized layer approximately 10 nm in thickness on the particle. To address the oxidation issue, the Fredrick group had proposed a partial ligand exchange method to replace the capping agents on the surface, and it was observed that the oxidation of germanium species slowed down significantly post-procedure. It is here Fredrick proposed a post synthetic surface treatment utilizing a ligand exchange processing to promote air stability in future studies.

Fredrick et. al.'s publication indeed displays the phase stability strength of Fe_2GeS_4 as the iron sulfide phases could be removed entirely by controlling the reaction temperature and time even at moderate temperatures. Though, despite the successful synthesis, it was apparent that, at the point of publishing the report, the Fe_2GeS_4 solution synthesis mechanism was still not well-understood, as many questions were left unanswered in the publication stated many times by the authors. However, a successful and stable ink under inert atmosphere was also shown to be doable, which is proven to be more advantageous when compared to Puthussery et. al (2010).’s research as stated above, where agglomeration of the ink was a serious issue. Yet, similar to Puthussery’s result, Fredrick cannot determine the exact band-gap with the Fe_2GeS_4 sample and can only determine that a gradual absorption was observed in the visible region³⁵. The lack of understanding of the reaction mechanism through solution synthesis and the inconsistencies in the data show that many aspects of Fe_2GeS_4 could still be researched into, including the possibility to develop new and more stable synthetic route.

2.4.2. Mechanochemical Processing and Post-Heat Treatment of Fe_2GeS_4 Nanocrystals

A top-down approach involves in the breaking down of the large, bulk, and heavy materials into the smaller and individual units of the target structures with any means necessary. One of the most traditional and reliable method of a top-down approach for synthesis is the method of mechanical milling. Mostly known for its utilization in producing paint and preparation of ceramic ingredients in the industrial level, a high energy ball-miller is utilized in mixing, and with the different materials, ranges from stainless steels to ceramics such as zircon,

and sizes of the balls, or the medias, that would lead to the size reduction of the materials with the impacts created upon the balls cascading down toward the target material. Due to the its facile and reliable nature, mechanical ball-milling has also been explored and found in scientific research as a reliable method in reducing the bulk material down to the submicron sized fine powder that is ideal for chemical reactions and further processing. In 2015, a Park et. al. took this concept further and develop a solid-state synthesis route for Fe_2GeS_4 based on Mechanochemical processing³⁶.

As reported by Park et. al., a mixture of iron, germanium, and sulfur elemental powders were mixed in the $\text{Fe}:\text{Ge}:\text{S} = 2:1.5:4$ ratio, as identified by Fredrick et. al. (2013) as the optimal ratio in a separate report, inside a stainless-steel jar containing zirconia balls of two different diameters, which were utilized for grinding down the size of the particles³⁵. Described in the article as grinding to “to the certain point,” the mechanical stress applied by the mechanical milling motion was eventually able to overcome the activation energy, thus initiates mechanochemical process to synthesizing iron germanium sulfide (Fe_2GeS_4) nanocrystals with the dimension of 60 to 200 nm. Finally, the as-synthesized Fe_2GeS_4 NCs were post-annealed at 450 °C for 2 h under H_2S (1%) atmosphere to enhance the crystallinity and reduce impurity phases.

To examine the effect of the ball-milling over time, Park arranged a time trial examining the XRD patterns of the powders milled at 8 h, 10 h, and 12 h. The results are shown in Figure 2.7. Only the elemental precursors were detected at 8 h. At the 10 h, however, an abrupt and significant change to the XRD pattern was observed where a surge of peaks identified to be

Fe_2GeS_4 were observed at this time along with impurity phases such as the Ge elemental precursor and binary FeS phase. The 12 h milled powder sample had only a phase pure Fe_2GeS_4 XRD pattern left, and the phase purity continued for samples prepared with longer milling time. Park et. al. thus concluded that the elemental precursors added to the steel jar were gradually reduced in size by the mechanical milling from 0 to 8 h during the “pulverization” step, to which point the reduction size elemental was theorized to have reached submicron and the agglomerates of particles have also been further reduced to only a few diameters. Continuing the milling to 10 h had seen no further changes in morphology based on the XRD patterns nor the TEM images, indicating the top-down processing via mechanical milling was already completed at 8 h. Instead, the additional 2 h milling was theorized to have been providing the milled particles kinetic energy by the continuous mechanical stress as generated by the grinding media.

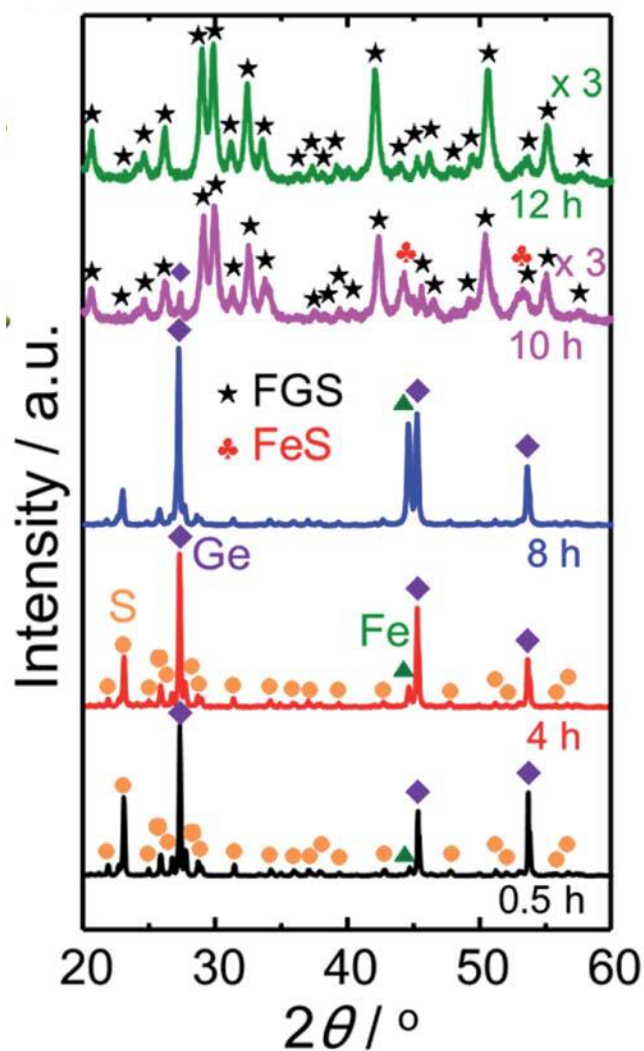


Figure 2.7. XRD patterns of the milled Fe₂GeS₄ product over various milling times³⁶.

Park et. al. thus concluded that when the particle size was decreased to “a certain point,” which was not clearly specified, the particle size became small enough where the additional energy provided from the 8 h to 10 h milling eventually was able to overcome the activation energy barrier to induce self-ignition and propagate the mechanochemical reaction to synthesize Fe₂GeS₄ at 10 h at the “chemical reaction” step. This was evident by the sudden appearance

Fe_2GeS_4 phase along with the gradual disappearance of secondary phases at this point was possibly the product of an incomplete reaction that had just been initiated a moment prior. The result observed at 12 h was consistent with the described mechanism.

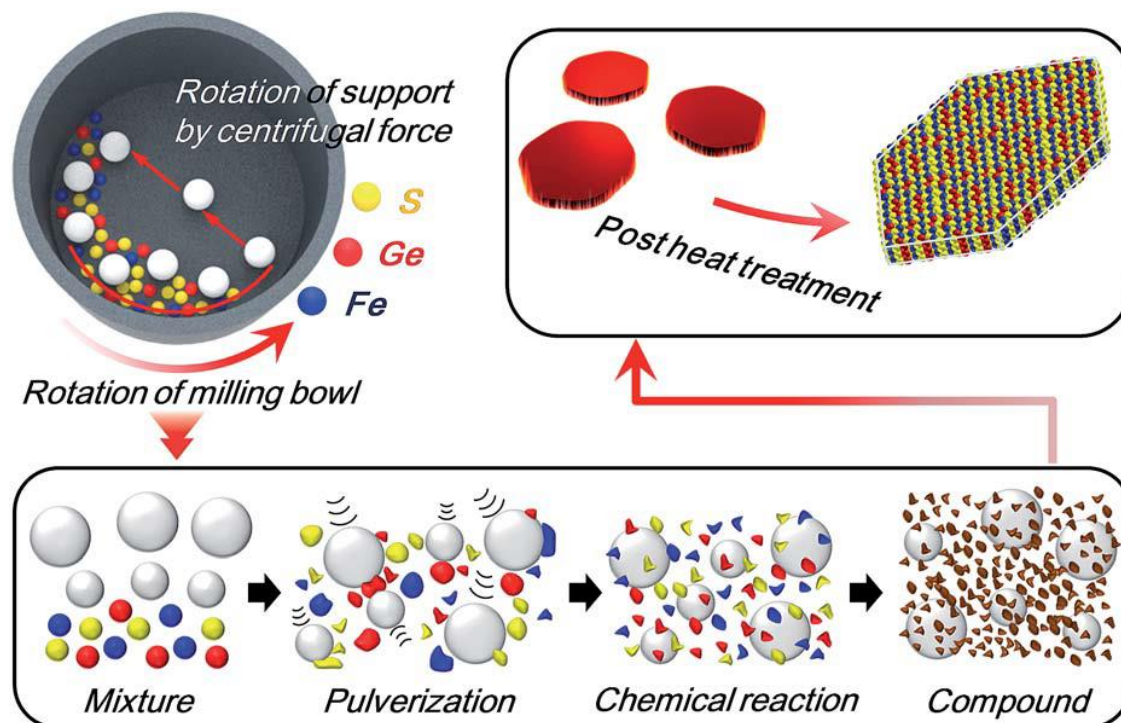


Figure 2.8. Schematic of the mechanochemical process utilized to synthesize Fe_2GeS_4 NCs³⁶.

To enhance the crystallinity of the as-synthesized Fe_2GeS_4 , Park proposed a post-annealing process under H_2S atmosphere at $450\text{ }^\circ\text{C}$. The obtained XRD pattern showed a nearly three-fold increase in the intensity peaks for Fe_2GeS_4 NCs. This was significant because the process had also proven the thermal stability of Fe_2GeS_4 at $450\text{ }^\circ\text{C}$ indirectly, thus alleviating the concern of decomposition during film processing in the future. As stated before, one inherent weakness of FeS_2 pyrite film was the phase instability and tendency to decompose at moderate

temperatures, especially when approaching 400 °C^{13,14,16,22,24}. Additionally, the TEM images captured were able to see a significant increase in NC size from 30 to 100 nm for the as-synthesized to 60-200 nm for the heat-treated sample. The plate-like morphology of the as-synthesized was observed to have changed into the well-defined hexagonal structure post-annealing. Park had contributed this factor to the post-treatment with an additional supply of sulfur atom had induced a rearrangement of atoms in the nanocrystals toward the most stable structure possible, thus resulting in the more well-defined morphology and enhanced crystallinity for the final product.

Another concern of any iron chalcogenide is the possibility of oxidation that ruins the band-gap entirely^{13,35}. As pointed out by Park, there were a few binary iron species revealed in the XPS spectrum for the as-synthesized Fe₂GeS₄ NCs that can be assigned to oxide-related Fe(II) ions. In addition, possible Ge-O peaks were also observed under XPS. The peaks associated to Fe-O and Ge-O bonds were observed to have reduced considerably after the heat treatment but was proposed that the oxidation of Fe₂GeS₄ is potentially reversible if the annealing procedure was supplied.

Park et. al.'s publication of Fe₂GeS₄ is a significant breakthrough. For starters, the author's group has provided a new synthetic route in the form of solid-state synthesis through mechanical milling, which is a rare method of formulating nanocrystals in the scientific community. As Park et. al. has stated, a typical Fe₂GeS₄ solution synthesis prior to this point requires an at least 24 h reaction time to produce the first onset of the desirable product, yet it would only take half of that if following Park's mechanochemical procedure via mechanical

milling. However, Park's publication has left out a few details unanswered, such as the "certain point" the report has mentioned during the mechanical milling process at 10 h. The "certain point" seems to be the key factor in the mechanism, whether it is the exact time or the exact particle size, to initiate the Fe_2GeS_4 synthesis with this setup. In addition, the temperature where the reaction initiated was also left out of the report, which could have been another important factor to examine since the temperature of the mill jar tends to increase under mechanical stress. It is perhaps due to the simplicity of the mechanical milling setup that potentially restricted Park et. al. from delving deeper into discussing these potential topics.

CHAPTER 3. EXPERIMENTAL METHODS

3.1. Materials

Table 3.1 lists all chemical reagents used in this dissertation, which was used as received and without further purification.

Materials	Chemical Formula	Purity (%)	Supplier
Iron (III) acetylacetonate	$\text{Fe}(\text{C}_5\text{H}_7\text{O}_2)_3$	97%	Alfa Aesar
Iron (II) chloride	FeCl_2	98%	Alfa Aesar
Iron (III) chloride	FeCl_3	98%	Alfa Aesar
Germanium (IV) tetraiodide	GeI_4	99.99%	Gelest Inc.
Germanium (IV) oxide	GeO_2	99.99%	MSE Supplies
Sulfur	S	99.5%	Alfa Aesar
Glycolic Acid	$\text{C}_2\text{H}_4\text{O}_3$	99%	Sigma-Aldrich
Toluene	C_7H_8	99.7%	VWR International
α – terpineol	$\text{C}_{10}\text{H}_{18}\text{O}$	96%	Alfa Aesar
Ethyl cellulose	$\text{C}_{20}\text{H}_{38}\text{O}_{13}$	48.0 – 49.5%	Sigma Aldrich
Ethyl alcohol	$\text{C}_2\text{H}_6\text{O}$	99.5%	VWR International
Molybdenum-coated soda lime glass (Mo-SLG)	N.A.	N.A.	The Institute of Energy Conversion, University of Delaware

Table 3.1. Materials used in this dissertation

3.2. Experimental Methods

The research displayed in this dissertation consisted of two stages. First stage involves molecular precursor based solid-state synthesis of Fe_2GeS_4 nanoparticles and the optimization of molecular precursor combinations and annealing conditions. Second stage is the optimization of

nanoparticle ink processing and thin-film fabrication of the Fe_2GeS_4 thin-films, which is characterized to examine its phase and mechanical properties.

3.2.1. Molecular Precursor Solid-State Synthesis of the Fe_2GeS_4 Nanoparticles

The solid-state synthesis of the Fe_2GeS_4 nanoparticles using the molecular precursor was a three-step process. The first step involves the preparation of $\text{Ge}[(\text{C}_2\text{H}_2\text{O}_3)_2(\text{H}_2\text{O})_2]$ precursor based the publication by Chiang et. al.³⁷. Second step is the preparation of the precursor combination series through a hand-grind procedure. Third step is the sulfurization procedure to manufacture the Fe_2GeS_4 nanoparticles. A schematic of the synthesis overview is illustrated in Figure 3.1.

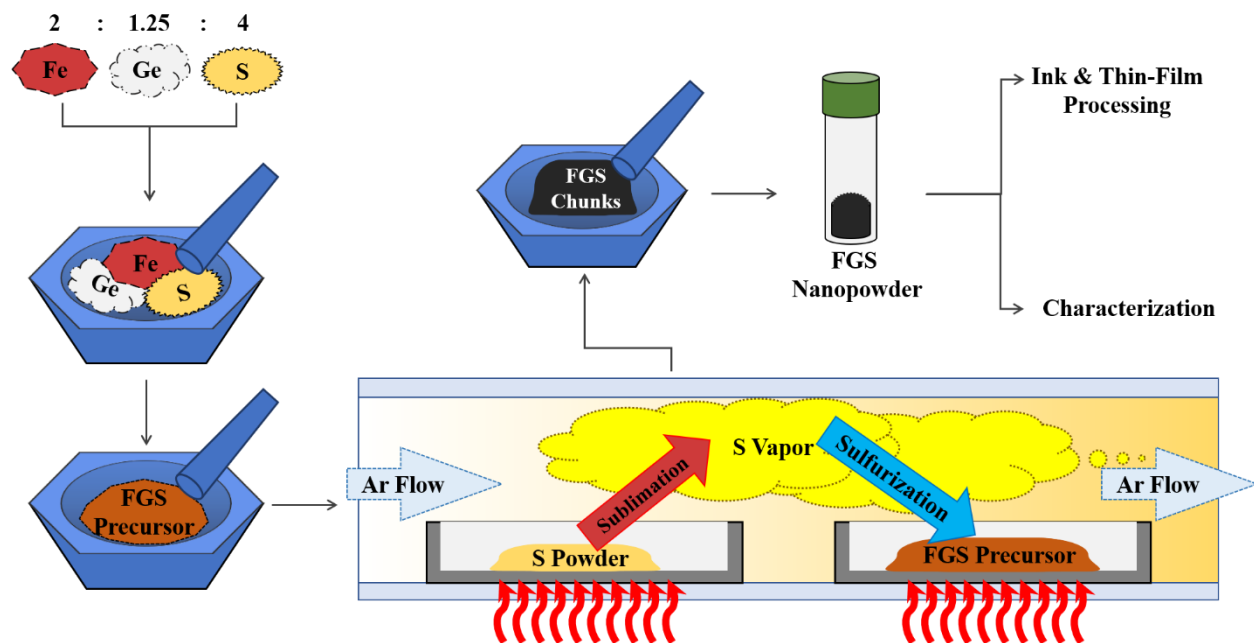


Figure 3.1. Schematic of the molecular precursor based solid-state approach utilized to synthesize Fe_2GeS_4 NPs.

Preparation of Diaquabis(oxoacetato-O,O")germanium (IV)Precursor

The $\text{Ge}[(\text{C}_2\text{H}_2\text{O}_3)_2(\text{H}_2\text{O})_2]$ compound was synthesized through a modified procedure based on the publication by Chiang et. al.. In a typical experiment, 20.0 mmol (1.52 g) of glycolic acid was dissolved in 100 mL of nanopore water in a 250 mL one necked round bottom flask with vigorous stirring at 1000 RPM under room temperature. Once the solids were dissolved, 5.0 mmol (0.52 g) of germanium dioxide (GeO_2) was added into the glycolic acid solution slowly under stirring to ensure no solute agglomeration. The reaction mixture was further refluxed for 4 hours and reduced to a 5 mL aliquot via rotary evaporation. The $\text{Ge}[(\text{C}_2\text{H}_2\text{O}_3)_2(\text{H}_2\text{O})_2]$ powder product was precipitated by adding up to 50 mL of the 1:1 mixture of diethyl ether and ethyl alcohol and was collected via vacuum filtration. The collected product was then dried and stored in a vacuum oven for the next step.

Preparation of Molecular Precursor

- The ***Acac-I₄*** series consists of 4 mmol (1412 mg) of $\text{Fe}(\text{acac})_3$, 2.5 mmol (1450 mg) of GeI_4 and 8 mmol (256 mg) of S.
- The ***Cl₂-I₄*** series consists of 4 mmol (507 mg) of FeCl_2 , 2.5 mmol (1450 mg) of GeI_4 and 8 mmol (256 mg) of S.
- The ***Acac-Gly*** series consists of 4 mmol (1412 mg) of $\text{Fe}(\text{acac})_3$, 2.5 mmol (640 mg) of $\text{Ge}[(\text{C}_2\text{H}_2\text{O}_3)_2(\text{H}_2\text{O})_2]$ and 8 mmol (256 mg) of S.

- The *Cl₂-Gly* series consists of 4 mmol (507 mg) of FeCl₂, 2.5 mmol (640 mg) of Ge[(C₂H₂O₃)₂(H₂O)₂] and 8 mmol (256 mg) of S.
- The *Cl₃-Gly* series consists of 4 mmol (648 mg) of FeCl₃, 2.5 mmol (640 mg) of Ge[(C₂H₂O₃)₂(H₂O)₂] and 8 mmol (256 mg) of S.

Heat Treatment via Sulfurization with Tube Furnace

A precursor mix of any combination mentioned above was grounded on an agate mortar and pestle for 10 min under air. The mix post-grounding should have of high homogeneity with a single color and phase state (depending on the precursor mix combination) was produced. The precursor mix was then collected and packed loosely in a ceramic boat, which was placed into a tube furnace for the sulfurization process at selected elevated temperatures with the ramp of 5 °C/min under constant argon gas flow for 2 hours and allowed to be cooled down naturally. After, the sulfurized material should resemble dark gray colored chunks, which were further grounded on a separate agate mortar and pestle to produce fine Fe₂GeS₄ nanoparticle powder, ready for characterization and ink formation.

3.2.2. Fabrication of the Fe₂GeS₄ Thin-Films

The part of the research involving the fabrication of the Fe₂GeS₄ thin-film is a three-step process. The first step involves the formulation of the Fe₂GeS₄ nanoparticle ink. The second step

is the thin-film processing via bar-coating. The third step is the adhesion test to determine the mechanical strength properties of the thin-films produced.

Ink Formation

Two precursor solutions were prepared prior to the Fe₂GeS₄ ink formation. Solution A was prepared with 1:3 ratios of α -terpineol and anhydrous toluene, and the Solution B prepared by dissolving 6 wt% of ethyl celluloses into a solvent of 1:4 ratios of ethanol and anhydrous toluene. Both solutions underwent vigorous stirring to ensure high homogeneity. A detailed illustration is shown in Figure 3.2.

- ***Ink 1*** was prepared by dispersing Fe₂GeS₄ nanoparticle materials in anhydrous toluene at a 200 mg/ml concentration with 20 min of ultrasonication.
- ***Ink 2*** was prepared by dispersing the material in Solution A at a 200 mg/ml concentration with 20 min of ultrasonication.
- ***Ink 3*** was prepared with two solutions. 1 ml of solution A and 50 μ l solution B were mixed and 200 mg of Fe₂GeS₄ powder was added. The powder was then dispersed by 20 min of ultrasonication.
- ***Ink 4*** followed the same preparation as Ink 3, but the mixing step was performed using a Flacktek Speedmixer (DAC 150.1 FVZ0K) in vacuum mode. The dispersion underwent 5 min of mixing at 2500 RPM under air, followed by 30 sec at 3000 RPM under vacuum.

Additional mixing under vacuum was conducted if the ink congealed or lost homogeneity due to agglomeration of nanoparticles.

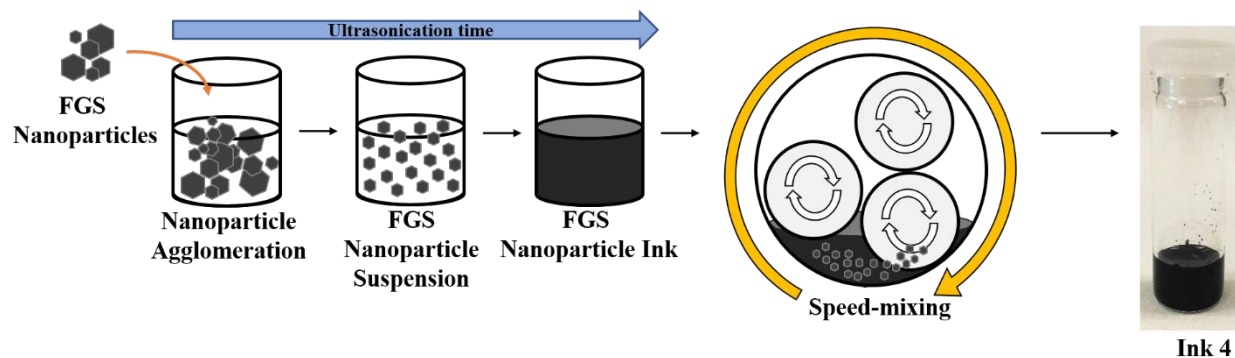


Figure 3.2. Schematic of the processing of Fe_2GeS_4 nanoparticle ink.

Film Processing

For the film processing, the Fe_2GeS_4 inks were applied onto quartz substrates via a bar-coating procedure. The bar utilized is modified based on a disposable soda-lime glass Pasteur pipet. The substrates were then soft baked at $120\text{ }^\circ\text{C}$ on a hotplate for 5 min under air to increase film adhesion. Next, the soft baked substrates were placed into a tube furnace for the sulfurization step with constant argon gas flow for 2 hours, in the presence of elemental sulfur at selected elevated temperatures with a $5\text{ }^\circ\text{C}/\text{min}$ ramp. Afterward, the annealed products were cooled down naturally. A detailed illustration is shown in Figure 3.3.

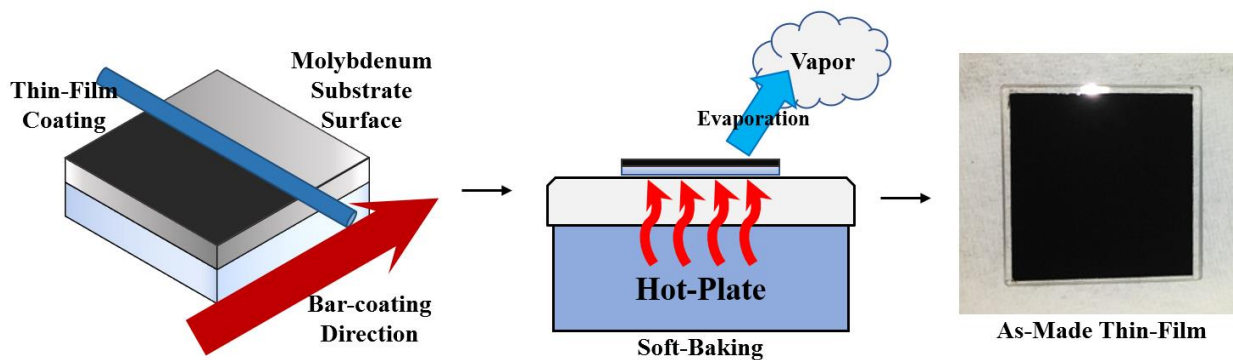


Figure 3.3. Schematic of the processing of Fe_2GeS_4 thin-films.

Adhesion Test

The adhesion test utilized home-built pull tester, as illustrated in Figure 3.4(a), was designed used to quantify the vertical film adhesion strength. In short, the sample substrate produced from the above step was glued securely on a platform. A glued pin was adhered onto the coated surface of the sample substrate, so a vertical force could apply pulling force away

from the surface. A steady increase of vertical force was applied over time until the pin detached from the surface entirely, which was then deemed the maximum lift-off pressure and recorded as the adhesion strength for the sample substrate.

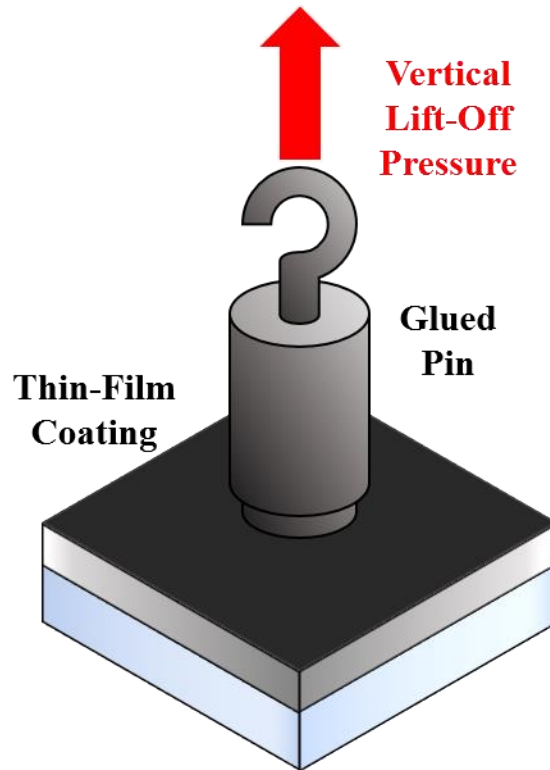


Figure 3.4. Schematics of the glued pin apparatus designed for the adhesion test.

3.3. Characterization of Fe₂GeS₄ Nanoparticle Properties

In this dissertation, we characterized the Fe₂GeS₄ nanoparticle and thin-film samples using the following methods: the X-ray diffraction (XRD), Rietveld refinement, Raman spectroscopy, Thermogravimetric analysis (TGA), Transmission electron microscopy (TEM) and a home-built pull tester.

X-Ray Diffraction (XRD)

The crystal structures and the XRD patterns were characterized by the Rigaku Miniflex 600, which equipped with the Cu K α radiation ($\lambda = 1.5418 \text{ \AA}$). The measurement conducted with a rate of 1°/min from the range of 10° to 70° with the condition of 30 mV and 10 mA. The nanoparticle powder samples was loaded onto a silicate sample holder during the measurement.

Rietveld Refinement

The XRD patterns measured by the Rigaku Miniflex 600 were individually loaded into the PDXL software (Version 2.4.2.0) by Rigaku Corporation for the Rietveld Refinement. Each loaded pattern was then matched with the literature reflection of phases that are comprised of combinations of the elements Fe, Ge and/or S that were suggested by the International Centre of Diffraction Data (ICDD) database. When all the phases of a selected XRD pattern were accounted for by selecting all the reasonable suggestions made by the ICDD database, the whole

pattern was simulated based on the phases selected utilizing the built-in Rietveld refinement procedure included in the PDXL software. For all simulations, the options of lattice constants and the profiles were refined while the crystal structure and the orientation were kept fixed. The steps of selecting the suitable phases that could account for all measured phases within a XRD pattern were to be repeated countless times until the optimal refinement within the physical boundaries were reached. If any phase was not accounted for based on the previous result, exiting out of the refinement and manually selecting more suitable phase candidates was necessary to ensure the quality of the refinement. From the optimal refinement, the percentage phase composition (% Phase) and the crystalline size were extracted for the purpose of this research.

Raman Spectroscopy

The Raman spectroscopy in this dissertation utilizes the Horiba Scientific XploRA PLUS Raman spectrometer. The laser setting utilized is the Ar-laser source with 532 nm with the range setting 250 cm^{-1} to 450 cm^{-1} . The as-made thin-films were placed onto the sample platform without further processing.

Thermogravimetric Analysis (TGA)

The determination of mass loss at elevated temperature for the Fe_2GeS_4 nanoparticle samples synthesized in this research was conducted using the Hitachi STA7200. The analysis setting has

the ramp condition set to 5 °C/min across the temperature range of 25 °C to 850 °C, under constant Ar gas flow of 20 psi to ensure inert atmosphere throughout the analysis.

Transmission Electron Microscopy (TEM)

The JEM-2100F Transmission Electron Microscope (TEM) is provided by the Delaware Biotechnology Institute (DBI) and is utilized to display the morphology and dimensions of the synthesized Fe₂GeS₄ nanoparticles for this dissertation.

Home-built Pull Tester

As illustrated in Figure 3.4, a home-built pull tester is designed and utilized for this dissertation. The goal is to determine the mechanical strength of the thin-film deposited by obtaining maximum lift-off vertical pressures. It utilizes a high-strength spring to exert the vertical force and determine the force exerted onto the thin-film sample itself.

CHAPTER 4. RAPID MOLECULAR SOLID-STATE SYNTHESIS TO CRYSTALLINE Fe_2GeS_4 NANOPARTICLES

Introduction

The natural disadvantages of FeS_2 iron pyrite have been observed by many previous publications, wherein the original FeS_2 phase, when under elevated temperatures, could easily decompose into the numerous and less favorable S-deficient binary phases including the Fe_7S_8 pyrrhotite phase, which have been characterized to have less useful optical, electronic, and magnetic properties that are not favorable traits in the manufacturing of efficient photovoltaic devices. Previous literatures have explored problem of phase instability, but no clear solution was provided. Instead, a ternary compound in the form of Fe_2GeS_4 was proposed and successfully demonstrated yet it left many questions as regard to the reaction mechanism unanswered. A key aspect to this research is the utilization and exploitation of the phase instability nature by incorporating the would-be disadvantageous factor into the reaction mechanism as an intermediate, thus providing a workable platform to introduce germanium into the binary phase of pyrrhotite, resulting in the creation the olivine structured, ternary phase Fe_2GeS_4 . This report details the successful synthetic approach, utilizing the above concept, via a facile and highly scalable solid-state chemistry to manufacture high phase stability and purity iron germanium sulfide (Fe_2GeS_4) nanoparticles and thin-films ready for photovoltaic device assembly. Further analyses on the phase shifts across different annealing temperatures and precursor combinations provides strong evidences that are in consistency with the nature of pyrite phase shifts at elevated temperatures as reported in previous literatures as well as the reaction mechanism proposed in this report.

Background and Significance

Solar energy is one of the iconic and the more applicable renewable energies that has seen steady growth of developments and interests over the past decades. Harnessing directly from the sun of our very own solar system itself, solar energy is a unique renewable energy like none others because the source of energy is seemingly unlimited that will continue the consistent solar radiation output for billions of years to come. It is unique also for the methods of power generation it uses. Unlike the typical power generators that relies on turning kinetic energy into electricity, a solar cell utilizes the photovoltaic effect, a mechanism when an absorber material absorbs photons from the sun's radiation and exciting electrons within the semiconductor device and, quickly afterward, the electrons would lose charges to generate electric potential, which could be stored as electricity that becomes a usable form of energy for humans.

Solar energy is a relative new field of power generation when compared to the other methods, such as fossil or nuclear, and, as a result, still have many aspects that need further optimization. One of the most important aspects that can improve solar energy's efficiency output is the development of high performance absorber material. Over the past few decades of solar research, numerous materials over three generations of solar cell materials have been researched, but all of them suffers from one flaw or another, whether it be mechanical, economical or environmental, that has prevented a successful widespread implementation of solar panels in the civilian market. Then comes the introduction of FeS₂ iron pyrite based thin-film solar research that has been proposed to have the capability to address all previous problems. FeS₂ thin film as the absorber material was theorized to be a low-cost, earth abundant, low

toxicity and lightweight design on top of the useful bandgaps had garnered tremendous interests. However, FeS_2 suffers severely for its phase instability and tendency to shift into S-deficient binary phases that have disadvantageous optical and electronic properties that are unsuitable for the photovoltaic effects. Many researches have been conducted to resolve this shortcoming, and attempts have been made to understand the cause of the phase instability. The introduction of silicon and germanium via doping to synthesize the ternary compound of Fe_2SiS_4 and Fe_2GeS_4 was proposed by Yu et. al. (2011) as an alternate product to promote phase stability in an iron chalcogenide thin-film, and significant stability increase was observed for the latter. Though the possibility to synthesize Fe_2GeS_4 nanocrystals was successfully demonstrated by Fredrick et. al. (2013) and Park et. al. (2015) with the solution-based synthesis mechanochemical reaction respectively, some of the details as regard to the analysis of the reaction mechanism and optimizing the reactions to obtain of the ternary Fe_2GeS_4 was not thoroughly explored in these publications.

This chapter will be delving into three important subjects to address these questions. First, this chapter will thoroughly analyze the effect of the choices of precursors and the different thermal conditions have in generating the ternary phase of Fe_2GeS_4 . Second, this chapter aims to provide a thorough insight of the reaction mechanism behind a successful synthesis of Fe_2GeS_4 by answering the phase shifting mechanism that is commonly observed in iron chalcogenide binary phases under elevated temperatures. Third and last, this chapter will demonstrate a rapid and highly scalable approach of an optimized solid-state synthesis route to produce high phase stability and high purity Fe_2GeS_4 nanocrystals. The aim is to demonstrate the possibility of utilizing phase instability, a factor commonly considered as weakness in material science, and

turning it into an advantageous design to a successful synthetic route in generating the desired product.

Solid-state chemistry fundamentally has a different approach to the synthesis requirements than that of the solution-based procedures, thus a thorough reevaluation of the experimental parameters that are typically used for a solution-based approach is required. The reevaluated parameters featured in this report are the precursor combinations and the annealing temperatures necessary for the adaptation to the new solid-state approach.

4.1 Precursor Combination Test

A precursor mix designed to synthesize Fe_2GeS_4 nanoparticles for this experiment has three reagent components: one is the source of iron, another is the source of germanium and lastly the source of sulfur. The mole ratio of the reagent components chosen for the experiment was the ratio of $\text{Fe}:\text{Ge}:\text{S} = 2:1.5:4$, which was reported to be an optimal ratio to synthesize phase pure Fe_2GeS_4 by Fredrick et. al. (2013) and Park et. al. (2015) in their individual reports. This reagent ratio was fixed for the entirety of the research for consistency. In addition, no other reagents were added into the precursor mixes to ensure no additional outside influences could occur during the synthesis, these consistencies provide an isolated environment where only the effects of using a different reagent source would be observed and analyzed at each separate instance.

The selected annealing temperature for the first phase of the research, the determination of the optimal precursor mix combination, was decided to be at 600 °C for two reasons. Previous experiments have shown that FeS₂ could be synthesized at very low temperature, thus is most likely to be the first phase to form during sulfurization. With this information considered, we intended to fully capitalize the phenomena previously reported by Zhang et. al. (2015) that the transition from FeS₂ pyrite to the S-deficient phase Fe_{1-δ}S generally starts close to 410 °C and finishes the conversion fully when the annealing temperature reaches 425 °C, and to avoid it. The initial goal was to raise the annealing temperature to be high enough to fully incorporate germanium into the iron chalcogenide complex to synthesize Fe₂GeS₄ prior to the occurrence of the full conversion between FeS₂ to Fe_{1-δ}S, and 600 °C, a straight 200 °C increase above the conversion temperature was thus selected as a controlled parameter for the first part of the research in order to weed out the possibility of generating undesirable S-deficient phases, so the focus will be solely on whether a precursor mix combination is possible for the designed solid-state route.

The first precursor mix chosen for the experiment was, in fact, based on the literature reported by Fredrick et. al. (2013), and it was the FeCl₂ as the source of iron, GeI₄ as the source of germanium, and elemental sulfur as the source of sulfur³⁵. Since this specific precursor combination has been previously proven in a solution-based route, the precursor mix labeled Cl₂-I₄ was chosen with the goal in mind to examine if there are any compatibility issues when transferring the exact parameters utilized by a typical solution-based approach to a solid-state synthesis scenario. The precursor mix post grinding on an agate mortar and pestle produced large sized dark colored crumbs of powders and does not separate from each other very well upon

additional grinding applied. This was noted as potentially had significantly decreased the surface area of the reagents' exposure to the heated environment during the sulfurization step. The $\text{Cl}_2\text{-I}_4$ product produced was a crude powder of black color with various sizes of crumbs. The XRD pattern collected, as shown in Figure 4.1, shows a mostly flat pattern, except for a few observable peaks with very low intensity, but these peaks that were observed do match with the pattern of Fe_2GeS_4 in literature³⁸. Thus, it could be argued that this experiment has successfully synthesized a minor phase of Fe_2GeS_4 ; however, the precursor mix was ultimately dropped due to too many missing peaks making the confirmation of the desirable product impossible.

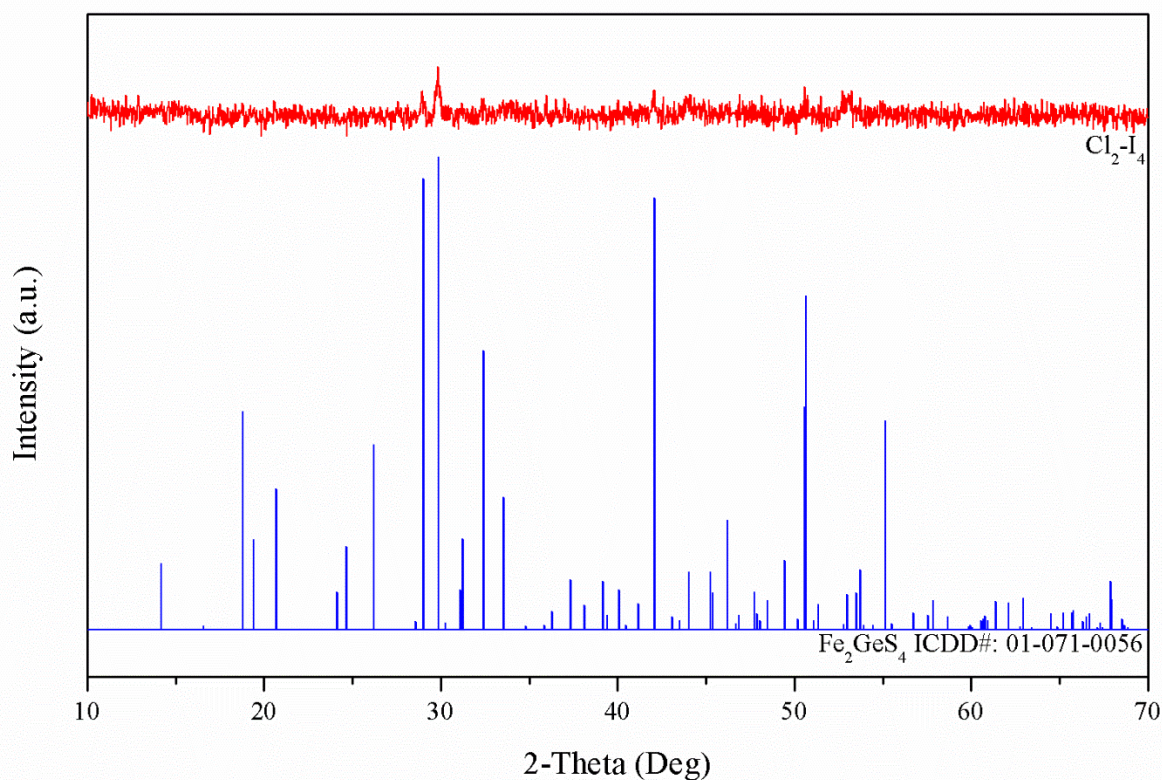


Figure 4.1. Comparison of the XRD pattern of $\text{Cl}_2\text{-I}_4$ product and Fe_2GeS_4 literature.

In comparison to the Cl₂-I₄, the Acac-I₄ precursor mix changed the source iron to Fe(acac)₃ but retained the same germanium and sulfur source in order to study the effect of changing the iron source in a solid-state route. Upon grinding the precursors together, a mixture of dark red powder was obtained with a significant reduction of particle size where no large size aggregate was produced. Post-annealing result produced gray crumbs that could be reduced to fine powder via grinding on an agate mortar and pestle. The XRD pattern, as shown in Figure 4.2, obtained for Acac-I₄ showed a great improvement over the Cl₂-I₄ with a significant increase in peak intensity overall and many were identified as Fe₂GeS₄ based on the literature pattern³⁸.

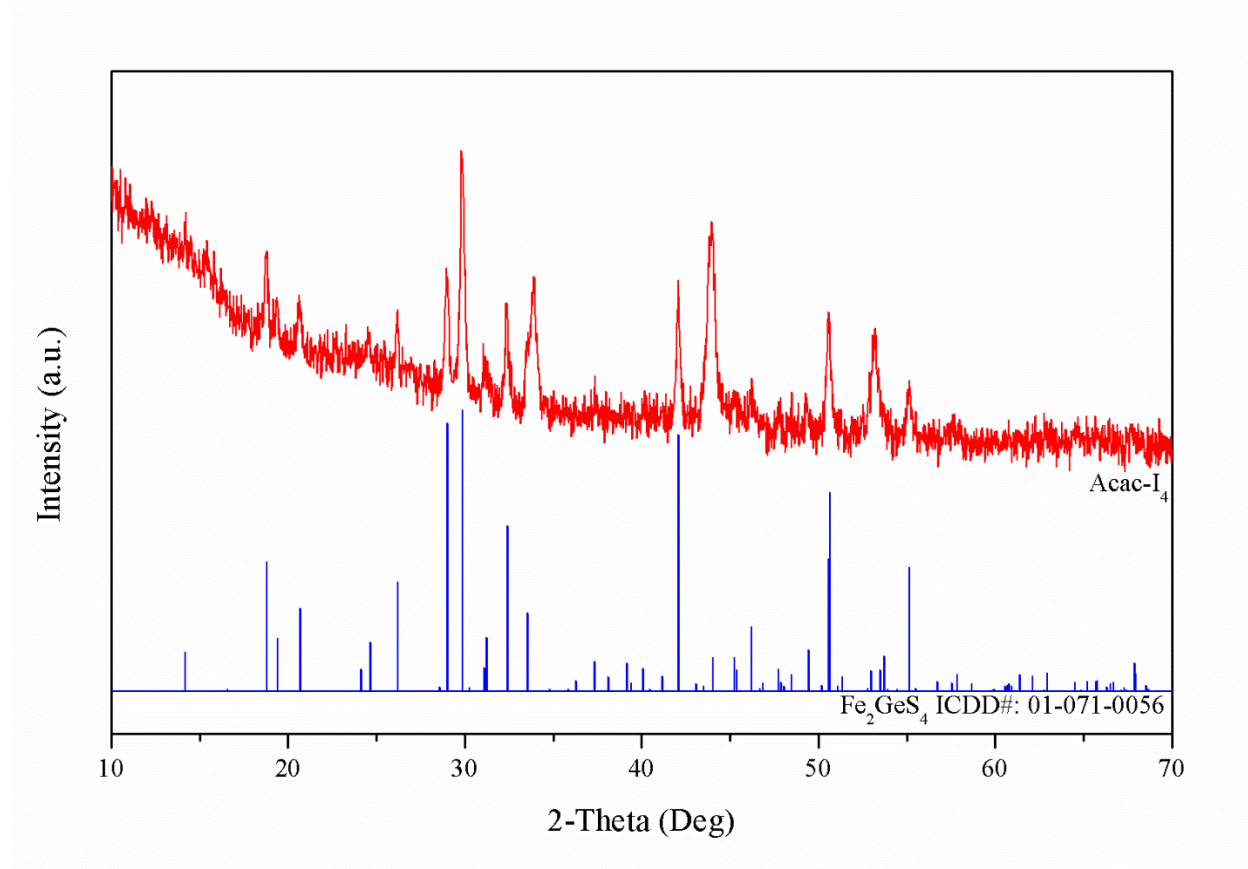


Figure 4.2. Comparison of the XRD pattern of Acac-I₄ product and Fe₂GeS₄ literature.

However, the Acac-I₄ also displayed unfavorable and concerning characteristics. First, some of the peaks were observed to have merged with each other, which was a sign of peak elongation as a result of the less angular defined, amorphous crystalline formation. Second, a significant ratio of impurities, where many peaks shown could be identified as pyrrhotite, the S-deficient phase that had plagued previous pyrite photovoltaic researches. Regardless of which iron source was utilized, both the FeCl₂ and Fe(acac)₃ variants showed the low peak intensity that could be greatly attributed to less angular defined, amorphous crystalline formation, which strongly indicated the possibility that the lack of nucleation was taking place during the annealing process. Possible solutions moving forward were either, first, increase the annealing temperature to further the nucleation process so crystalline formation would be more completed or, second, change the precursor materials, so to change the rate of diffusion, to allow for more robust solid-state reactions. The latter was chosen so a new line of precursor combinations with a different source of germanium, Ge[(C₂H₂O₃)₂(H₂O)₂], could be examined for its effect in synthesizing Fe₂GeS₄.

The first of the new line of precursor combination tested was the Acac-Gly. Coming from the Acac-I₄, the only change in the precursor mixture is the change in the source of germanium and, by retaining the same source of iron and sulfur, the effect to synthesize using a different germanium source could be examined. Upon grinding on an agate mortar and pestle under air, a mixture of bright red powder was obtained with slight aggregations. It was noted that the mixture would begin to build up adhesion to each other toward aggregating slightly near the end of the grinding step, near the 9th min. Following the sulfurization, the post-annealed product of Acac-Gly obtained was coarse chunks of light gray color, which was successfully reduced to fine

powder after grinding. The physical appearance of the Acac-Gly product is a great departure from any of the precursor combination involving GeI_4 as a reagent most significantly in the color change. As shown in Figure 4.3, the XRD pattern obtained for Acac-Gly displayed the desired phase purity with only the phase of Fe_2GeS_4 being picked up. In addition, the overall peak intensity of Acac-Gly has also increased significantly from what the Acac- I_4 could offer. Despite the fact of merging peaks displayed, indicating the less angular crystalline feature due to incomplete annealing, the Acac-Gly trial confirmed that utilizing $\text{Ge}[(\text{C}_2\text{H}_3\text{O}_2)_2(\text{H}_2\text{O})_2]$ was a step in the right direction in successfully obtaining a phase pure product³⁸.

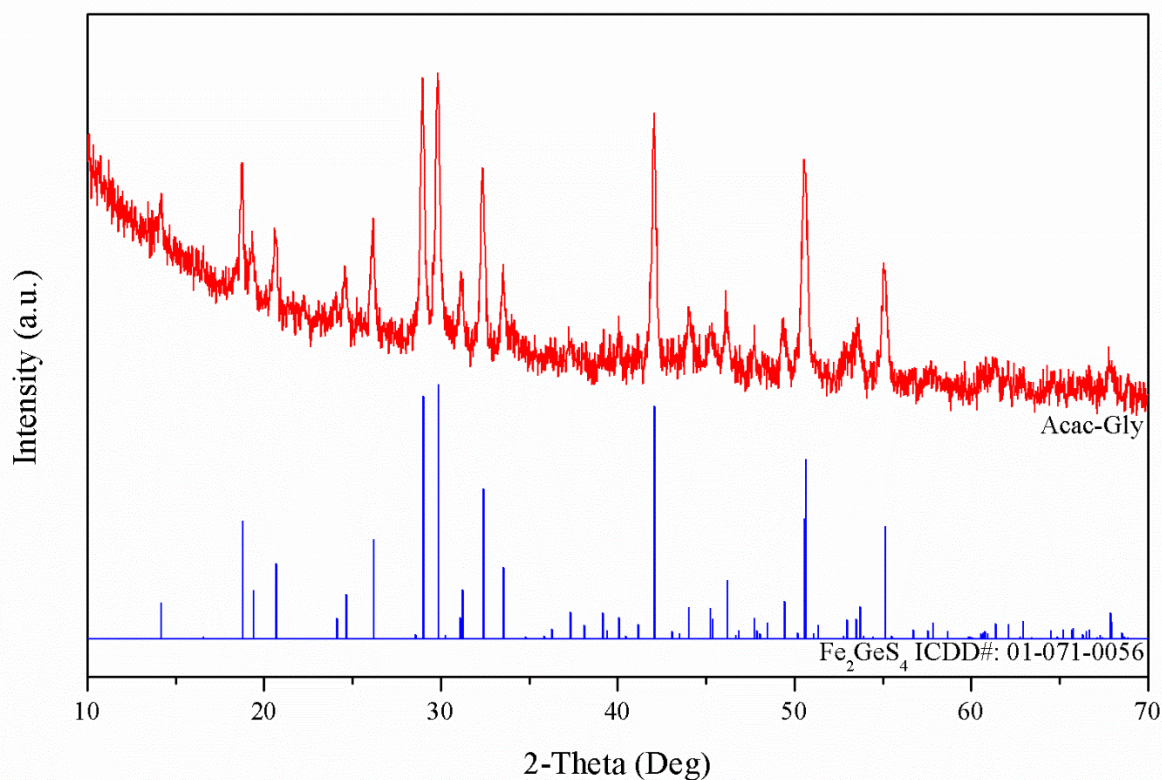


Figure 4.3. Comparison of the XRD pattern of Acac-Gly product and Fe_2GeS_4 literature.

The next step of the research changed the iron precursor to study its effect; FeCl_2 was utilized in the stead of $\text{Fe}(\text{acac})_3$ in combination with the $\text{Ge}[(\text{C}_2\text{H}_2\text{O}_3)_2(\text{H}_2\text{O})_2]$ that had previously yield satisfactory results of obtaining phase pure Fe_2GeS_4 product. The FeCl_2 , $\text{Ge}[(\text{C}_2\text{H}_2\text{O}_3)_2(\text{H}_2\text{O})_2]$ and sulfur precursor combination, labeled as Cl_2 -Gly, had produced a mixture of fine powder of brown color, typically with little to no aggregation. The sulfurized product of Cl_2 -Gly produced was coarse chunks of light gray colored, sharing great resemblance to the Acac-Gly product both in color and the fact that, upon grinding, a very fine powder could be produced. The XRD pattern obtained for Cl_2 -Gly, as shown in Figure 4.4, shared the same phase purity that was also observed in Acac-Gly³⁸. The increase in peak intensity when compared to Acac-Gly, indicating the more completed nucleation process, was also observed. Moreover, the peaks were more defined, and the merging peaks problems shared by previous combinations was less significant. The Cl_2 -Gly combination could be regarded as a straight upgrade in performance coming from Acac-Gly.

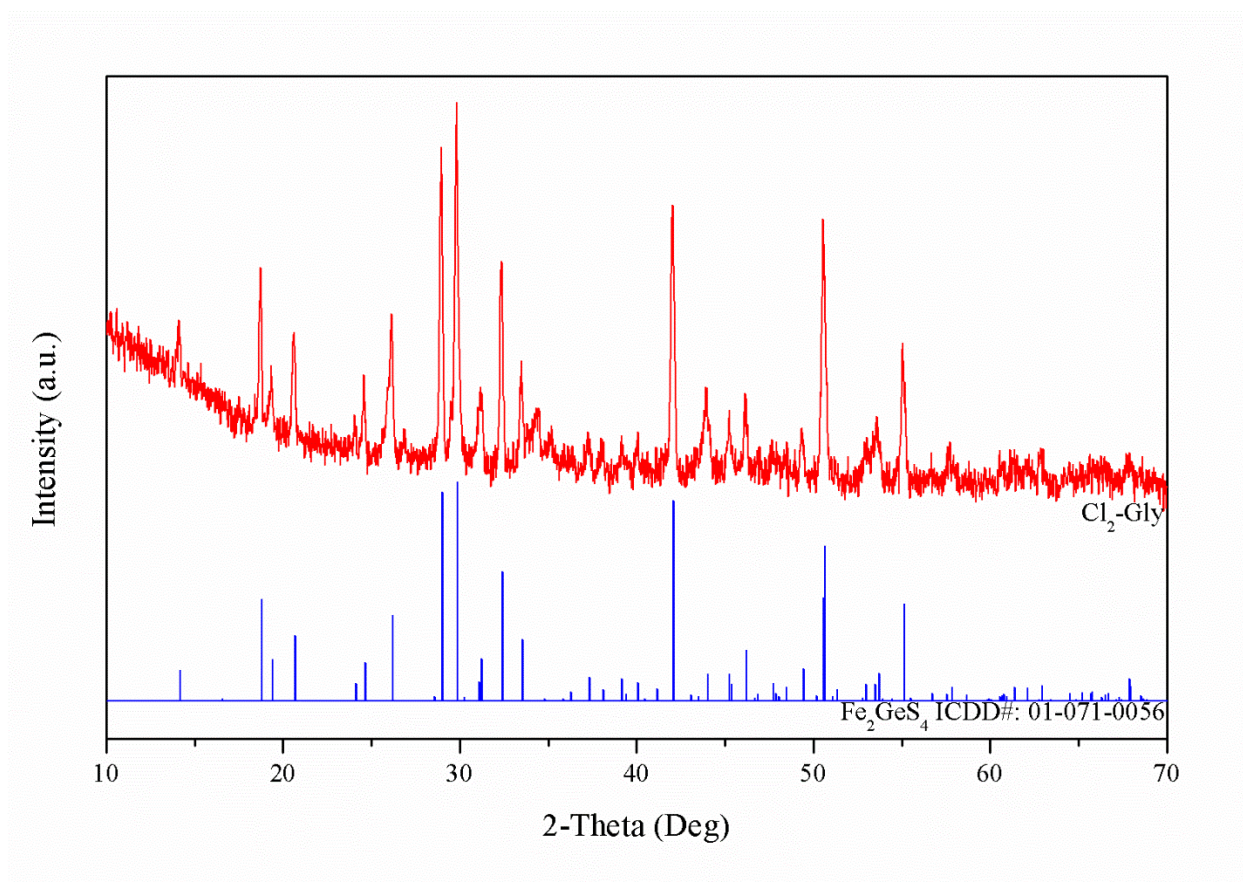


Figure 4.4. Comparison of the XRD pattern of Cl₂-Gly product and Fe₂GeS₄ literature.

By choosing FeCl₃ as the iron precursor, the labeled Cl₃-Gly was designed to determine the effect of additional chlorine in an annealing procedure, as previous literature has suggested the addition of chlorine during sulfurization was beneficial in accelerating the annealing procedure, thus obtaining better crystal formation. As Cl₂-Gly, though already a significant improvement over Acac-Gly, still displayed a few merging peaks that still suggested further improvement was required. Upon grinding FeCl₃, Ge[(C₂H₂O₃)₂(H₂O)₂] and sulfur together, it was realized at once the tremendous humidity that FeCl₃ could absorb, evident by the powders wetting instantly, from ambient atmosphere as soon as the grinding had started. Further grinding

would produce a very thick paste of mixture that was viscous and sticky to any surface. The paste produced was dark brown color. Unlike the previous precursor combinations, transferring $\text{Cl}_3\text{-Gly}$ to the ceramic boat required manually spreading with a spatula motion similar to a “spreading butter to toast” due to the high viscosity behavior the paste had, making it difficult to be transferred from the agate mortar and pestle it was previously ground and produced. Spreading was done to ensure the paste would have a better surface area to react to the sulfurization procedure. Also because of the high viscosity, a large portion of the paste material was not recoverable simply due its preference to adhere to the agate mortar surface more than spatula. The post-annealed $\text{Cl}_3\text{-Gly}$ product was thin slates of light gray color, which was typical to Fe_2GeS_4 physically based on the above experiments. The thin slate morphology was most likely the result of the spreading method the paste material was transferred, unlike the powder materials previously that had been transferred as one would typically do with powder and weighing paper. In addition, the thin slate product of $\text{Cl}_3\text{-Gly}$ had the iconic coarse texture shared by the Fe_2GeS_4 nanoparticles produced with Acac-Gly and $\text{Cl}_2\text{-Gly}$ precursor combinations.

The XRD pattern of $\text{Cl}_3\text{-Gly}$, shown in Figure 4.5, confirmed the existence of Fe_2GeS_4 and no other iron binary phases were detected, ensuring the phase purity of the product. Shown in Figure 4.6, a combining pattern of the XRD patterns collected for the precursor combination test, the pattern for the $\text{Cl}_3\text{-Gly}$ series had displayed a significant increase in peak intensity of about three-fold increase when compared to Acac-Gly and about two-fold increase to $\text{Cl}_2\text{-Gly}$. The $\text{Cl}_3\text{-Gly}$ product also showed much sharper peaks with no visible peak merging, which had been a problem for the previous precursor combination tests. Figure 4.7 shows the TEM image of the Fe_2GeS_4 nanoparticles produced using $\text{Cl}_3\text{-Gly}$, the average dimension of these

nanoparticles ranges from 150 nm – 250 nm. Considering the above factors, Cl₃-Gly produced the best result with high quality and phase pure product in comparison to all the other precursor combination proposed in this report, thus was determined to be the ideal material to be utilized in the ink processing and thin-film production portion of the experiment.

Analyzing the results of the Precursor series reveals that the series with Ge[(C₂H₂O₃)₂(H₂O)₂] as the germanium precursor performs better than the series utilizing GeI₄ with stronger peak intensity and better peak resolution, both characteristics indicating higher crystallinity for the Fe₂GeS₄ nanoparticle products because of the more completed annealing procedure. It was thought that the water molecules in Ge[(C₂H₂O₃)₂(H₂O)₂] have served the role as a surfactant that has accelerated the annealing process. During the hand-grinding process of FeCl₃ and Ge[(C₂H₂O₃)₂(H₂O)₂], it was observed that the precursor mixture has acquired additional moisture to create a wet-gel mixture. The moisture was most likely obtained from air since the hand-grind process was on bench-top exposed to ambient atmosphere, but the additional water molecules provided in Ge[(C₂H₂O₃)₂(H₂O)₂] has likely added to that effect and allowed the additional folding and condensing of the precursor powders further increasing the density of the precursor materials than the other series. By increasing the density of the materials, the annealing reaction will have increased surface to work with, thus guaranteeing the faster and more completed reaction overall, which could explain the superior results shared by the precursor series with Ge[(C₂H₂O₃)₂(H₂O)₂] over GeI₄.

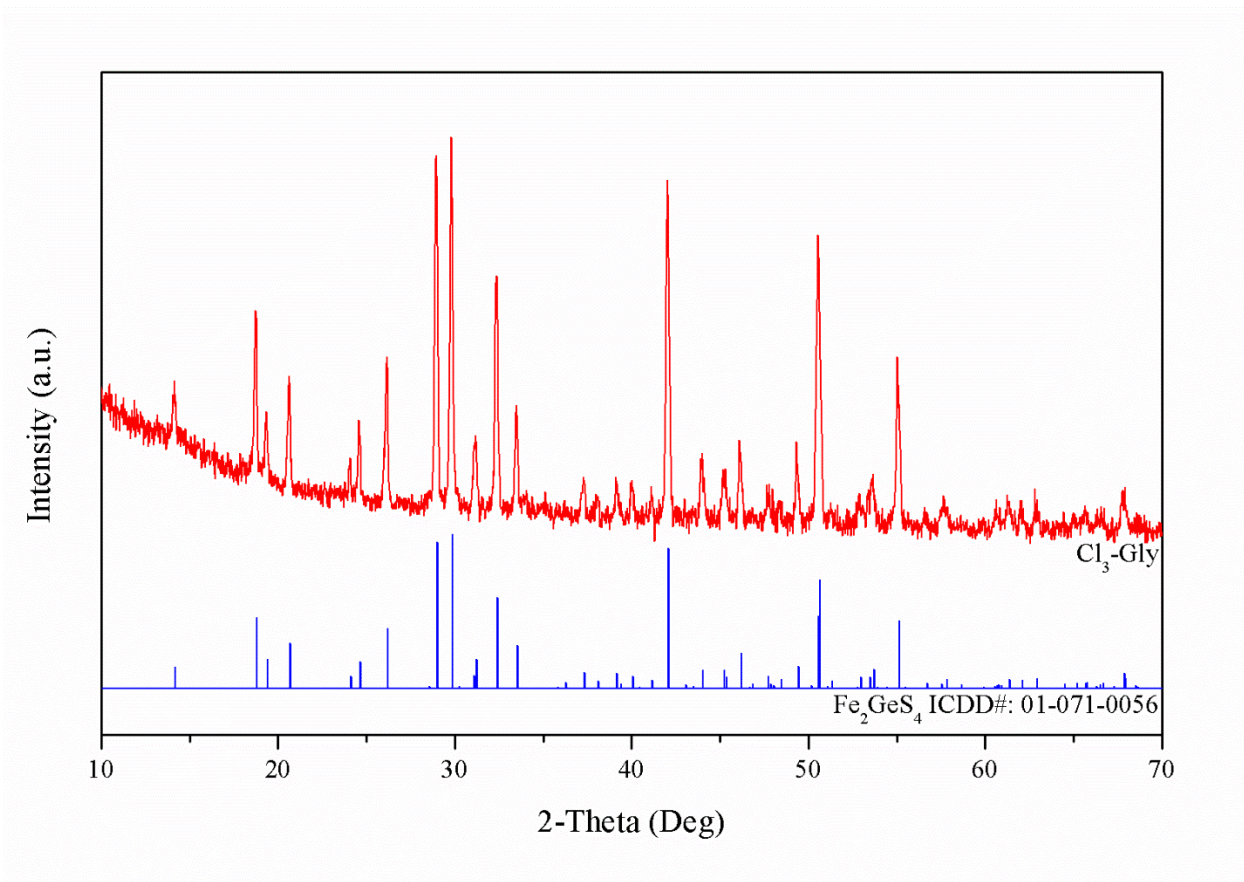


Figure 4.5. Comparison of the XRD pattern of Cl₃-Gly product and Fe₂GeS₄ literature.

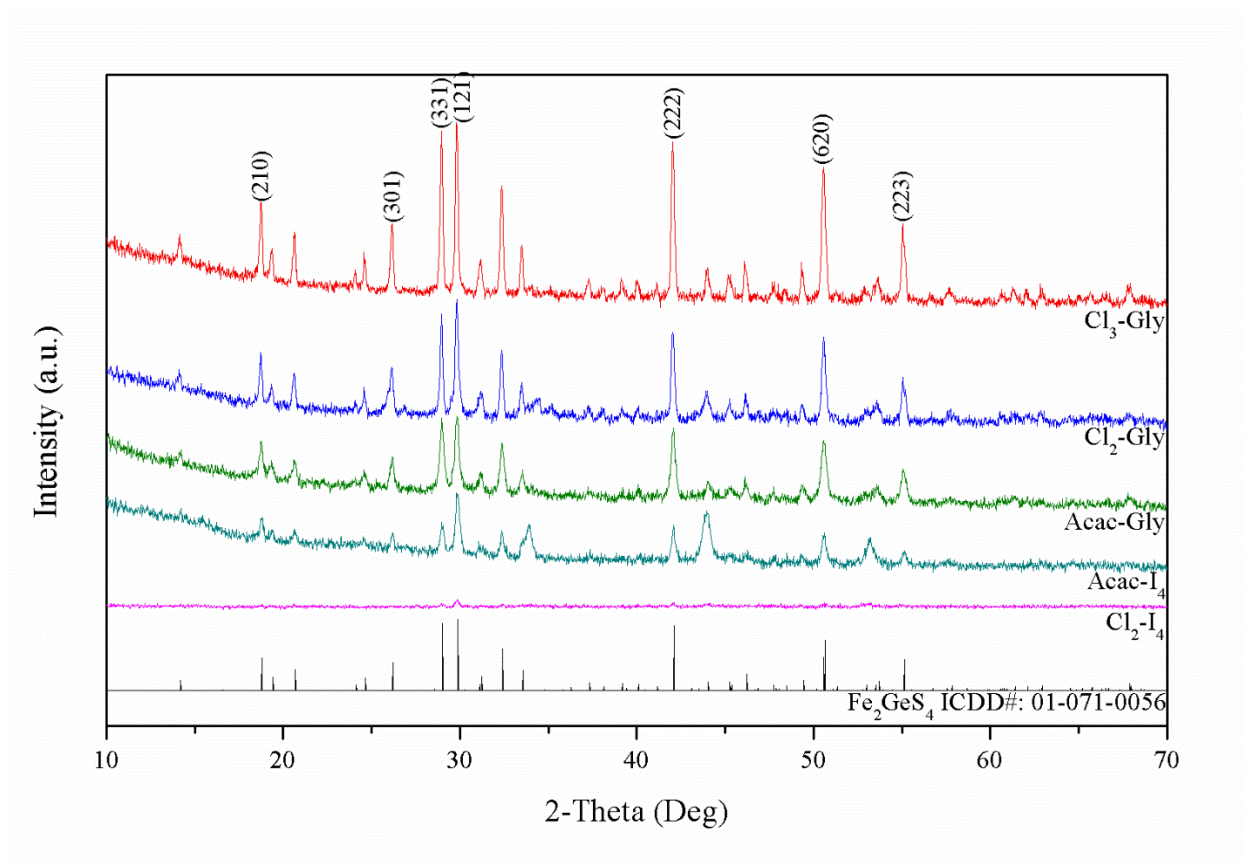


Figure 4.6. Comparison of the XRD pattern measured for the precursor combination test.

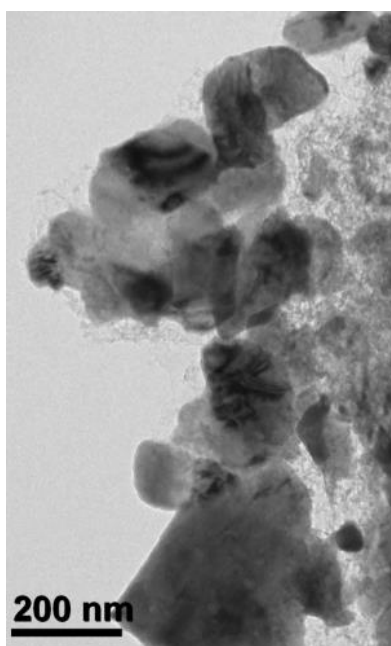


Figure 4.7. TEM image of Fe_2GeS_4 nanoparticles produced with $\text{Cl}_3\text{-Gly}$.

4.2. Annealing Temperature Test

For this part of the research, the primarily goal of the annealing temperature test was to determine the optimal temperature necessary to produce the desirable phase pure, high quality Fe_2GeS_4 nanoparticle product. To achieve this target, a thorough study of the iron chalcogenide phase shifting mechanism in the presence of germanium was a necessity. Thus, the experiment was designed to characterize the ratio and crystalline sizes of the detectable phases, both pure and impure, across the selected annealing temperatures from 400 °C to 600 °C in 50 °C increments in order to capture the effect of the rising annealing temperature has over the precursor materials. The 400 °C annealing stage was chosen as the lowest of the annealing temperature examined in this specific part of the research due to that it was the highest temperature that a FeS_2 iron pyrite would remain the majority phase just prior to the rapid conversion to $\text{Fe}_{1-\delta}\text{S}$ pyrrhotite at 410 °C, as suggested in the report by Zhang et. al. (2015) in their study of pyrite phase stability²⁴. By examining the conversion before, at 400 °C, and after, at 450°C, we aimed to observe if a general trend was shared between Zhang's report, which only concerned the elements of iron and sulfur, to this very report of ours, which germanium was added with the iron chalcogenides²⁴. Three sets of annealing temperature tests using the Acac-Gly, Cl_2 -Gly and Cl_3 -Gly precursor series were conducted to determine whether a shared phase shift mechanism for iron chalcogenide in the presence of germanium could be observed.

To accurately analyze the mechanism of phase shift, one crucial data that is required to build the model is be the percentage phase composition (% Phase) over the entire sample, which could be utilized in obtaining the trend of phase shift by examining the increase or decrease of a

specific phase over the selected annealing temperatures. In this report, the % Phase data for all three sets of XRD patterns obtained in the annealing temperature tests were extracted by simulating the XRD patterns of the Fe₂GeS₄ products using Rietveld refinement mentioned previously under the Method section of this report.

4.2.1. Acac-Gly Series Annealing Temperature Tests

The Acac-Gly series was the first of three series of XRD patterns being simulated by Rietveld refinement for extracting the % Phase and the crystalline size data. Shown in Figure 4.8, the XRD patterns for Acac-Gly series when annealed at 400 °C displayed a single phase of FeS₂ pyrite. Table 4.1 tabulated the Rietveld refinement result and the FeS₂ pyrite as the only detectable phase at 400 °C with the % Phase at 100 ± 30%, which was in consistency with the measured XRD pattern. This result comes as no surprise as, in the 2015 report by Zhang et. al., the FeS₂ pyrite phase would stay as the majority phase at 400 °C until rapid conversion to Fe_{1-δ}S begins as the annealing temperature reaches 410 °C²⁴. The large standard deviation value for the %Phase for this temperature was probably the cause of part of the XRD patterns that could not be matched by any literature reflection from the ICDD database, leaving the refinement calculation concluded with ±30% uncertainty of the possibility of other binary phases.

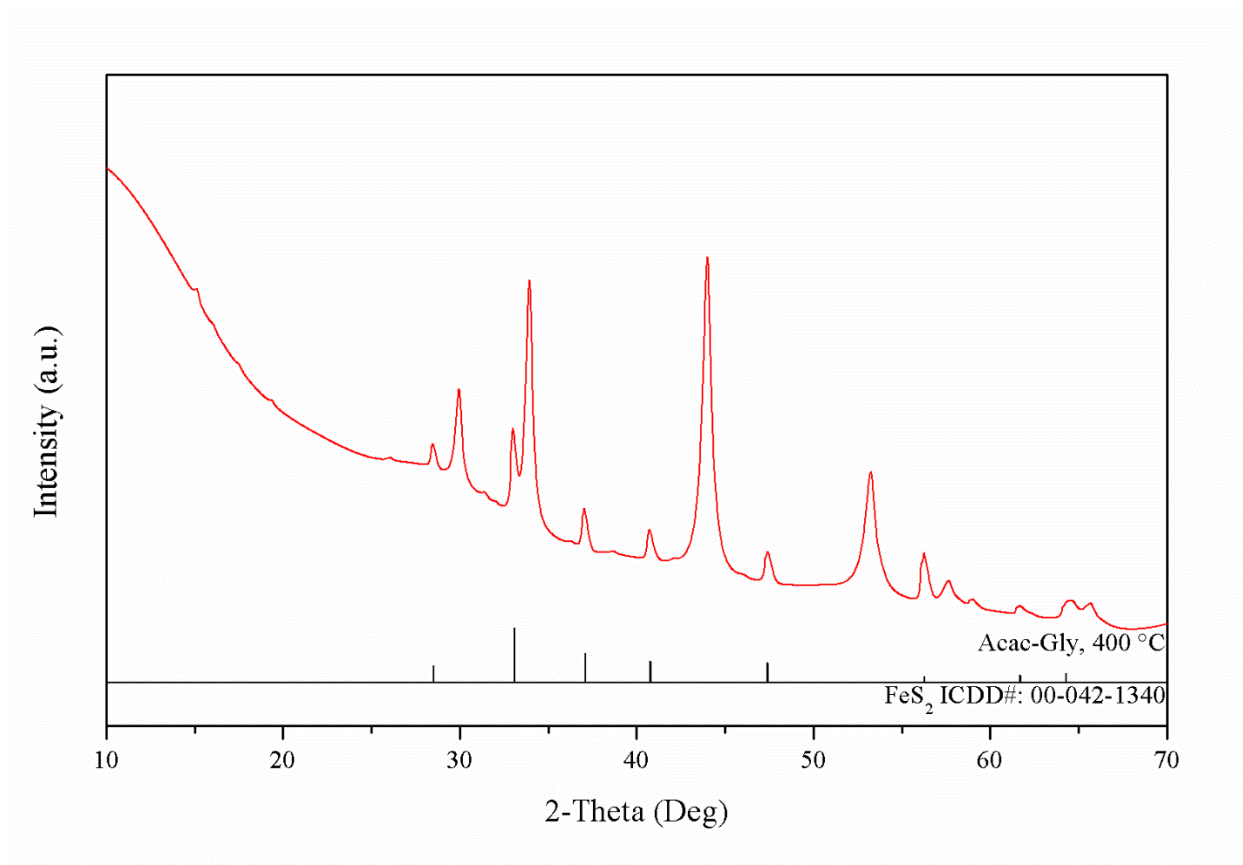


Figure 4.8. XRD patterns of the Acac-Gly series when annealed at 400 °C.

Acac-Gly, 400 °C				
Annealing Temperature	Observed Phases	ICDD No.	% Phase	Crystallite Size (nm)
400 °C	FeS ₂	00-042-1340	100 ± 30	26.7 ± 1.3

Table 4.1. Rietveld refinement data of the Acac-Gly series when annealed at 400 °C.

With the annealing temperature increases to 450 °C for the Acac-Gly series, it was observed that three phases total were synthesized following the experiment, as shown in the refinement data in Table 4.2. The majority phase that took over $45 \pm 7\%$ was the Fe₇S₈, which was an expected result in consistency with the previous report by Zhang et. al. (2015) that had

suggested the conversion between FeS_2 to $\text{Fe}_{1-\delta}\text{S}$ would begin at 410°C ²⁴. Yet, unlike Zhang's report, we observed that the addition of germanium has delayed the conversion between pyrite to pyrrhotite phase as the detected FeS_2 phase retained $16 \pm 6\%$ of percentage phase composition instead of being completely converted into the S-deficient phases like previously suggested. In fact, FeS_2 that took up the entirety of the phase composition at 400°C was now placed the least in the composition after a 50°C increase, suggesting a significant percentage of elements had been converted to the other phases following the increase in annealing temperature. Some of these elements that were converted but had begun their reaction with germanium had led up to the phase that was placed the second most by percentage phase composition was Fe_2GeS_4 with $39 \pm 3\%$. The increase in temperature was just enough to initiate the germanium to react with iron and sulfur to form the desirable product, yet the condition was still more suitable for the formation to the majority phase in the S-deficient phase Fe_7S_8 . However, it should be noted that the XRD pattern of the measured product, shown in Figure 4.9, already had great resemblance to the pattern specific to Fe_2GeS_4 due to the significant percentage it had taken in the product mixture³⁸.

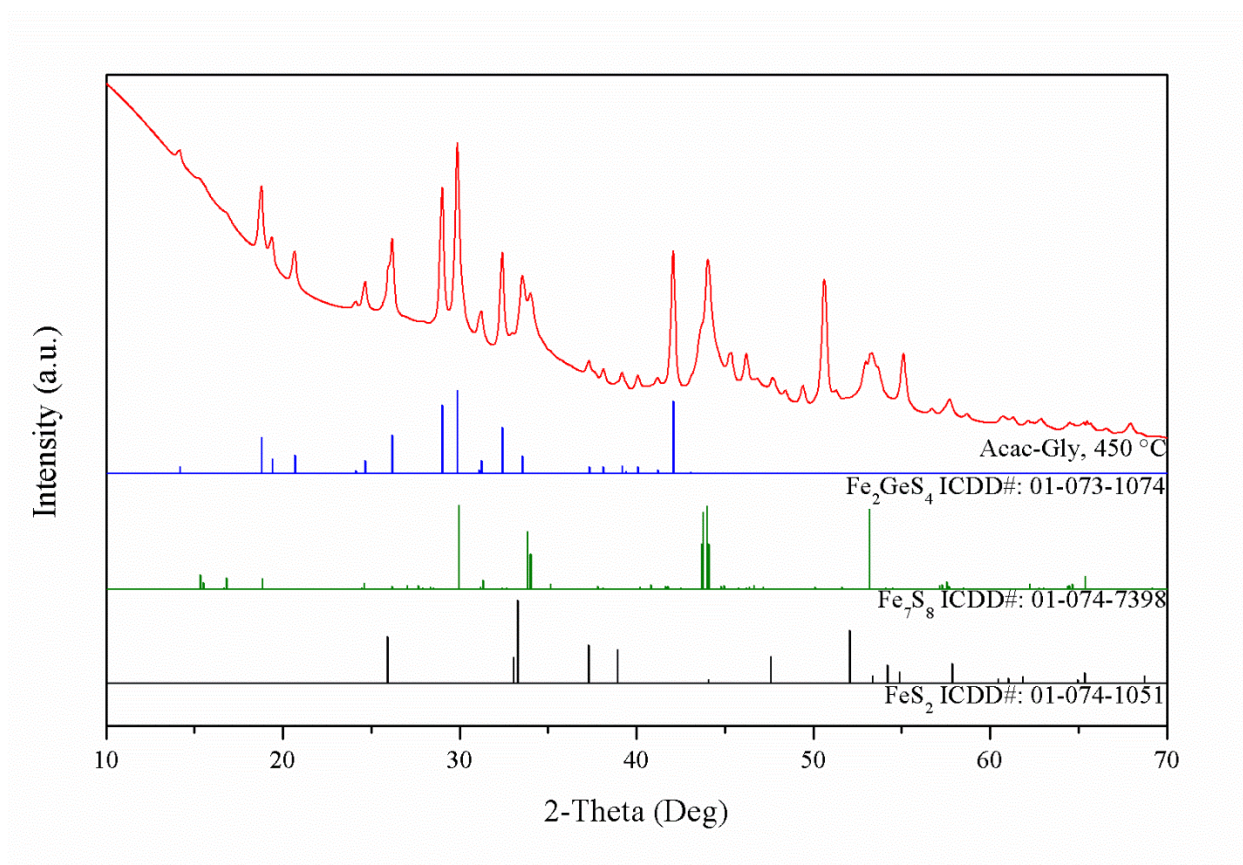


Figure 4.9. XRD patterns of the Acac-Gly series when annealed at 450 °C.

Acac-Gly, 450 °C				
450 °C	Fe ₂ GeS ₄	01-073-1074	39 ± 3	21.8 ± 0.3
	Fe ₇ S ₈	01-074-7398	45 ± 7	7.3 ± 1.4
	FeS ₂	01-074-1051	16 ± 6	72.5 ± 8.2

Table 4.2. Rietveld refinement data of the Acac-Gly series when annealed at 450 °C.

Increasing the annealing temperature from 450 °C to 500 °C observed a few important trends amongst the phases. First, as shown in Table 4.3, Fe₂GeS₄ had become the majority phase of the mixture with the percentage phase composition increase to 45 ± 3%, thus a conclusion

could be drawn that an increase in annealing temperature was proportional to the synthesis of Fe_2GeS_4 . Second, while the FeS_2 phase stayed much the same in % Phase value (although a slight increase from $16 \pm 6\%$ to $17 \pm 7\%$ but could be considered as systematic error by the Rietveld refinement due to the increase was well within the standard deviation), a significant reduction of Fe_7S_8 phase was observed from $45 \pm 7\%$ to $38 \pm 6\%$. The XRD pattern for this stage of the experiment, shown in Figure 4.10, displayed the Fe_2GeS_4 phase becoming more prominent as the intensity of the peaks that belonged to Fe_2GeS_4 increased overall. Even with the increase in annealing temperature, the % Phase for pyrite remained mostly unchanged and was suspected that it had taken no part in the reaction at this stage. Instead, it was believed that only the iron and sulfur elements from Fe_7S_8 phase could react with the germanium in the mixture as a significant reduction in % Phase was observed only on the Fe_7S_8 phase.

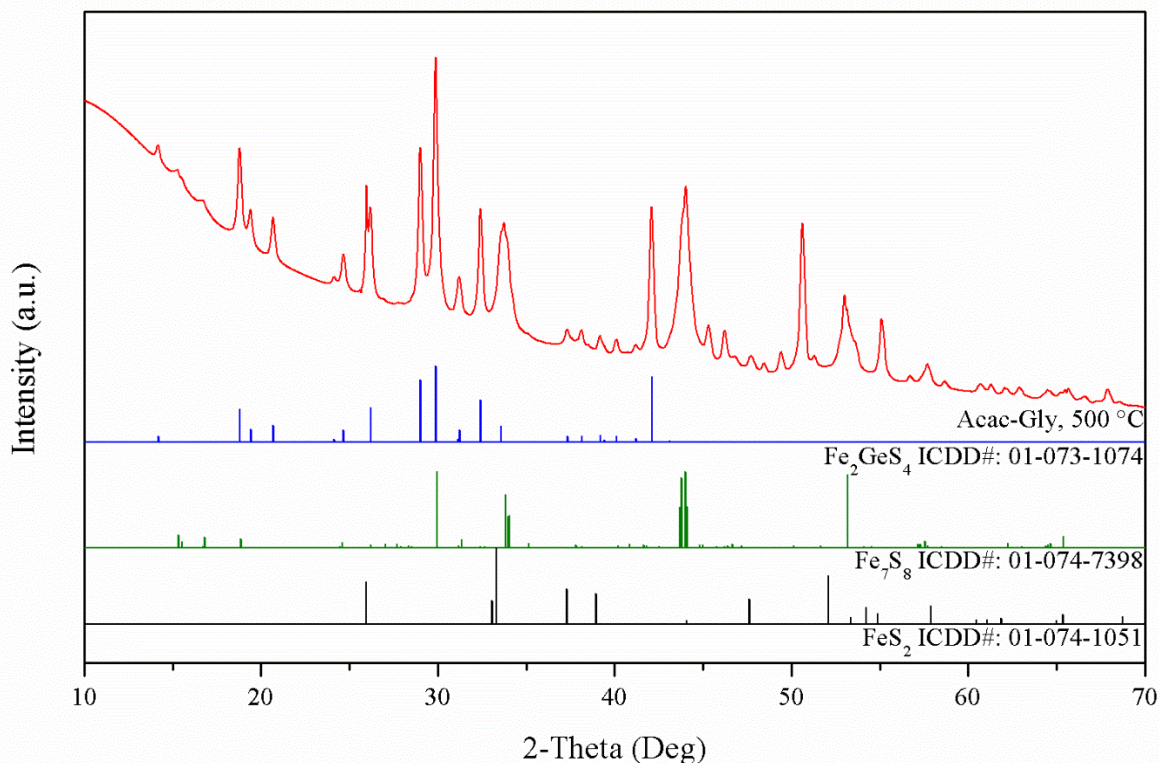


Figure 4.10. XRD patterns of the Acac-Gly series when annealed at 500 °C.

Acac-Gly, 500 °C				
Annealing Temperature	Observed Phases	ICDD No.	% Phase	Crystallite Size (nm)
500 °C	Fe ₂ GeS ₄	01-073-1074	45 ± 3	4.5 ± 0.3
	Fe ₇ S ₈	01-074-7398	38 ± 6	10.8 ± 0.4
	FeS ₂	01-074-1051	17 ± 7	44.3 ± 5.3

Table 4.3. Rietveld refinement data of the Acac-Gly series when annealed at 500 °C.

The next 50 °C increment pushed the annealing condition of Acac-Gly series to 550 °C. This was the first temperature stage where the FeS₂ phase was completely converted into other

iron chalcogenide phases. Contrary to Zhang et. al., whose report had shown that phase pure pyrite's full conversion would finish at 425 °C, it had appeared that the inclusion of germanium in the reaction had the effect of delaying the rate and the point to full conversion to pyrrhotite by 125 °C higher²⁴. According to the refinement result shown at Table 4.4, the percentage phase composition obtained at 550 °C showed an equal split where both Fe₂GeS₄ and Fe₇S₈ phase has the exact same % Phase value of 50 ± 4% based on the simulation obtained via Rietveld refinement, though bearing in mind the values may not be entirely accurate due to error inherent to the simulation. Over the 50 °C increase, the Fe₂GeS₄ phase had a slight 5% increase while Fe₇S₈ saw a significant 12% increase in % Phase out of the 17 ± 7% of FeS₂ from 500 °C. Based on these values, FeS₂ was more readily to be converted into Fe₇S₈ than Fe₂GeS₄, if at all, since it was entirely possible that the 5% addition of Fe₂GeS₄ came solely from the reaction using the elements of Fe₇S₈ phase instead of the FeS₂ phase. This theory was also more coincide to the phenomena observed for Acac-Gly series at 500 °C where the growth of Fe₂GeS₄ was observed at the same stage with the reduction of Fe₇S₈ phase while the FeS₂ phase remained similar % Phase. Figure 4.11 showed the XRD patterns of Acac-Gly series at 550 °C to have a slightly improved peak sharpness as observed at peak (3 0 1).

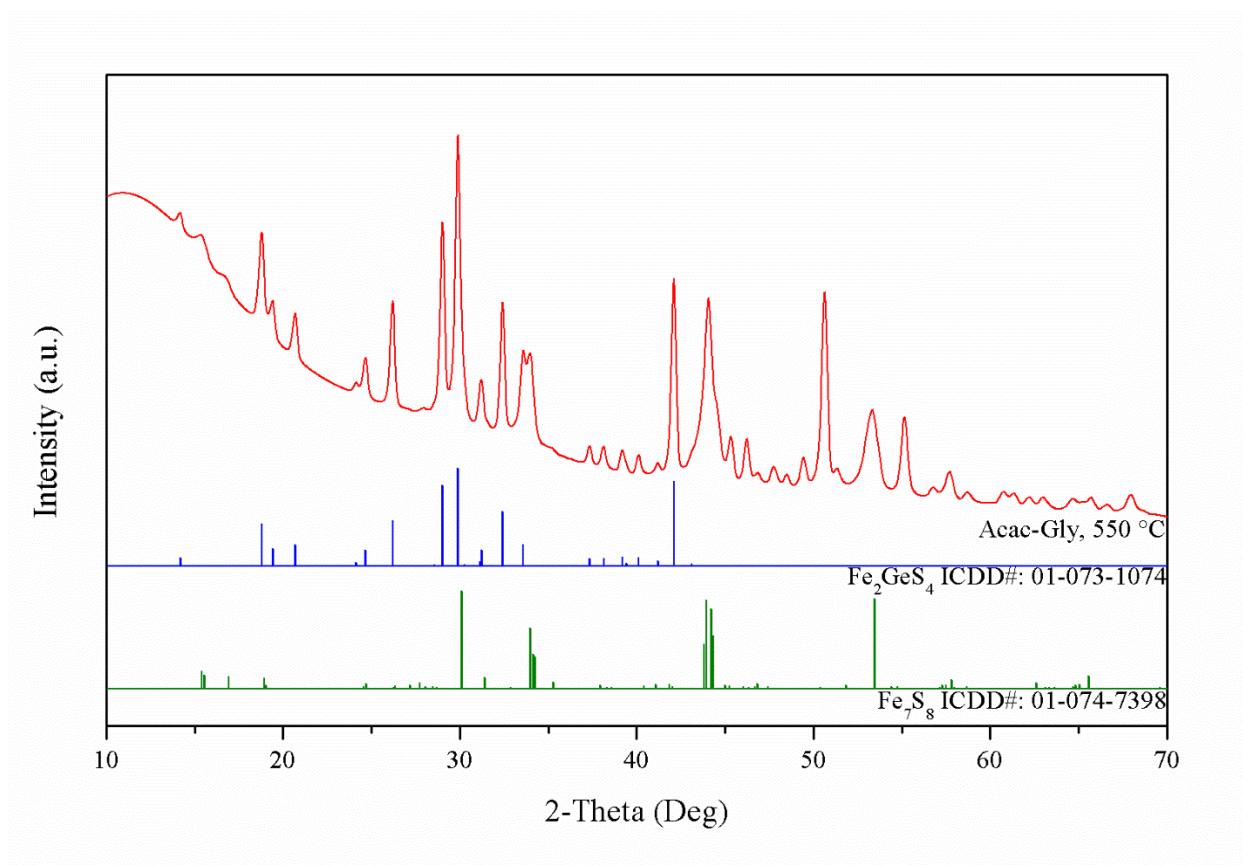


Figure 4.11. XRD patterns of the Acac-Gly series when annealed at 550 °C.

Acac-Gly, 550 °C				
Annealing Temperature	Observed Phases	ICDD No.	% Phase	Crystallite Size (nm)
550 °C	Fe ₂ GeS ₄	01-073-1074	50 ± 4	19.2 ± 3.0
	Fe ₇ S ₈	01-074-7397	50 ± 4	9.9 ± 0.8

Table 4.4. Rietveld refinement data of the Acac-Gly series when annealed at 550 °C.

As shown in Table 4.5, the 600 °C annealing temperature test, also the last test for Acac-Gly series, resulted in the increase in % Phase for Fe₂GeS₄ phase at 72.5 ± 0.8%. The S-deficient Fe₇S₈ phase was calculated to have a reduction and had a % Phase at 27.5 ± 1.9 %.

Shown in Figure 4.12, the XRD pattern obtained for Acac-Gly series at 600 °C displayed yet another increase in peak intensity for the Fe_2GeS_4 phase, yet many of the peaks that belong to the impurity phase, the Fe_7S_8 phase, remained but with a significant reduction of its peak intensities as well as when comparing the peak ratio of the two peaks. A general trend was observed that the growth of Fe_7S_8 and Fe_2GeS_4 was inverse of one another. Considering that the % Phase for both phases were equal when the annealing temperature was at 550 °C and no other phases were present, it was assumed that Fe_7S_8 was a source providing the iron and sulfur elements necessary to react with germanium in the mixture that had attributed to the synthesis of Fe_2GeS_4 . In another word, Fe_7S_8 was consumed during the annealing reaction with elevated temperatures and used as a reagent to synthesize Fe_2GeS_4 . This assumption was strongly supported by the numerous occurrences where the Fe_2GeS_4 phase grew along with the reduction of Fe_7S_8 phase that were observed for the annealing temperature stages from 450 °C to 500 °C and from 550 °C to 600 °C.

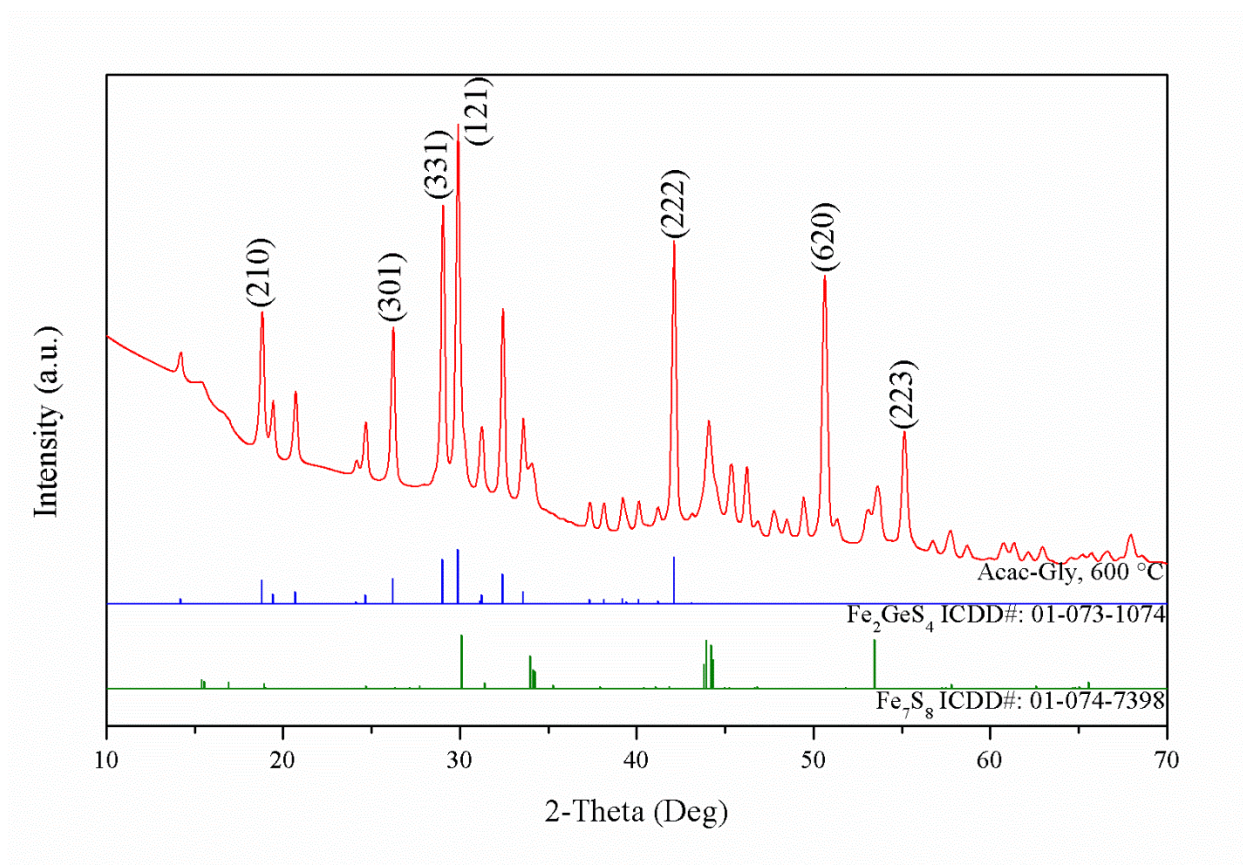


Figure 4.12. XRD patterns of the Acac-Gly series when annealed at 600 °C.

Acac-Gly, 600 °C				
Annealing Temperature	Observed Phases	ICDD No.	% Phase	Crystallite Size (nm)
600 °C	Fe ₂ GeS ₄	01-073-1074	72.5 ± 0.8	22.2 ± 3.0
	Fe ₇ S ₈	01-074-7397	27.5 ± 1.9	11.2 ± 8.0

Table 4.5. Rietveld refinement data of the Acac-Gly series when annealed at 600 °C.

Overall, the annealing temperature test for the Acac-Gly series across the elevated temperatures from 400 °C to 600 °C had indeed produced the desirable product of Fe₂GeS₄, but with a severe shortcoming: the solid-state synthesis procedure with this specific precursor

combination could not yield a single-phase product even at the highest annealing temperature set at 600 °C. The reaction to synthesize the phase pure product was incomplete, but it was suspected at this point of the research that a better precursor combination may yield yet a better result as it was already observed that Cl₂-Gly and Cl₃-Gly at the precursor combination test already displayed cleaner pattern with better peak intensities in comparison. Regardless, the Acac-Gly series confirmed with the report proposed by Zhang et. al., about the temperature required to initiate the conversion from pyrite to pyrrhotite, and it was despite with the delay of the temperature required to complete full conversion of pyrite by approximately 125 °C possibly due to the influence of germanium in the reaction mixture²⁴.

4.2.2. Cl₂-Gly Series Annealing Temperature Test

The Cl₂-Gly series annealing test was designed to have the exact same solid-synthesis procedures utilized by the Acac-Gly series except changing the precursor combination, and more specifically changing the iron precursor from Fe(acac)₃ to FeCl₂, so to study the effect of a different ligand on the phase shift mechanism. Based on the XRD pattern obtained for Cl₂-Gly in Figure 4.4, which had displayed a cleaner Fe₂GeS₄ pattern with stronger peak intensity than the Acac-Gly series, a simply better experimental result with better peak intensity and stronger ternary phase presence was expected, but the actual result was not the case whatsoever due to a unique binary phase detected and the different temperature requirement to cause certain phase formation.

Based on the Rietveld refinement result, the Cl₂-Gly series at 400 °C annealing temperature yields three iron chalcogenide phases, FeS₂, Fe₇S₈ and Fe₃S₄ in order of percentage composition. The XRD patterns obtained for this stage of experiment, shown in Figure 4.13, was consistent with the refinement showing the three detected phases. In contrary to the phase purity shown in the Acac-Gly series, where the FeS₂ phase was at 100 ± 30% as the sole phase existing at 400 °C, the FeS₂ phase at Cl₂-Gly had only 18 ± 3% as also the least in % Phase in the product mixture. On the other hand, the S-deficient phase, Fe₇S₈, took up 35 ± 7% in phase composition at this stage while it was not detected by XRD at this annealing temperature previous in the Acac-Gly series. The Cl₂-Gly series had already shown a great departure from expectation by changing into a different iron precursor, but what sets this specific series apart was the detection of the Fe₃S₄, a phase unique to only the Cl₂-Gly series in the scope of this experiment. Fe₃S₄, also known as greigite, was also a S-deficient phase of an iron chalcogenide similar to pyrrhotite. It has 47 ± 5% in phase composition, close to half of the entire product was greigite, but, as it was quickly realized, greigite only existed at 400 °C in the Cl₂-Gly and not to be detected ever again for the rest of the research.

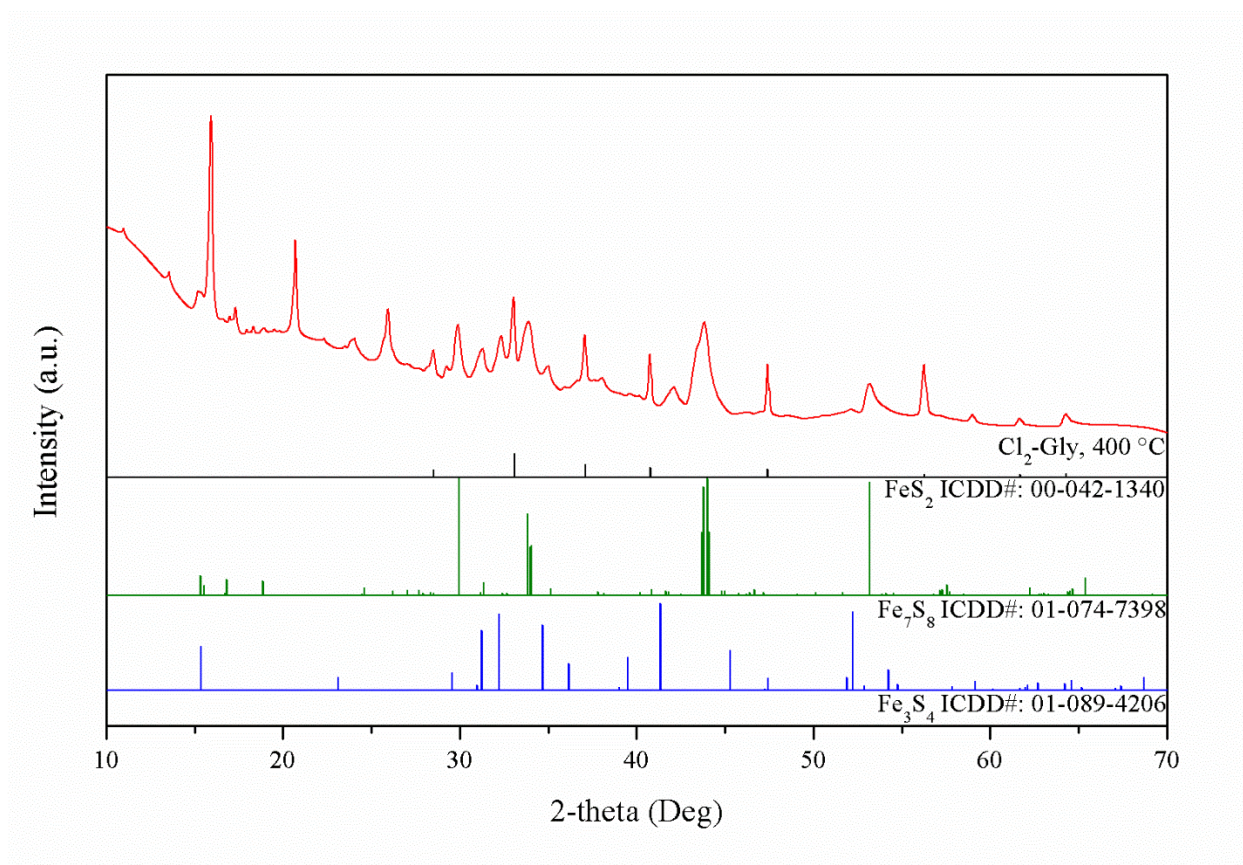


Figure 4.13. XRD patterns of the Cl₂-Gly series when annealed at 400 °C.

Cl ₂ -Gly, 400 °C				
Annealing Temperature	Observed Phases	ICDD No.	% Phase	Crystallite Size (nm)
400 °C	FeS ₂	00-042-1340	18 ± 3	14.0 ± 0.2
	Fe ₇ S ₈	01-074-7398	35 ± 7	15.1 ± 0.3
	Fe ₃ S ₄	01-089-4206	47 ± 5	16.0 ± 8.6

Table 4.6. Rietveld refinement data of the Cl₂-Gly series when annealed at 400 °C.

Increasing the annealing temperature from to 450 °C for Cl₂-Gly observed the full elimination of the Fe₃S₄ gregite phase. Based on the Rietveld refinement shown in Table 4.7 and the associated XRD pattern in Figure 4.14, however, it doesn't reduce the number of phases in

the mixture from three to two, instead we had observed the instance where two phases of FeS₂ coexisted in the product. The two phases of FeS₂, though sharing the same chemical formula, had been assigned with different ICDD No. in the database due to the differences in crystalline and lattice parameters. Among the three phases shown at this stage, FeS₂ had an overall 66.3% in % Phase when adding up the two phases together, a significant increase from 18 ± 3% at 400 °C. The Fe₇S₈ pyrrhotite phase was observed to have a slight reduction down to 30.0 ± 3%. With the significant increase in % Phase for FeS₂ and a slight but relatively insignificant % Phase reduction for Fe₇S₈, it was a possible conclusion that the majority of the Fe₃S₄ phase had been converted into FeS₂ along the increase in annealing temperature.

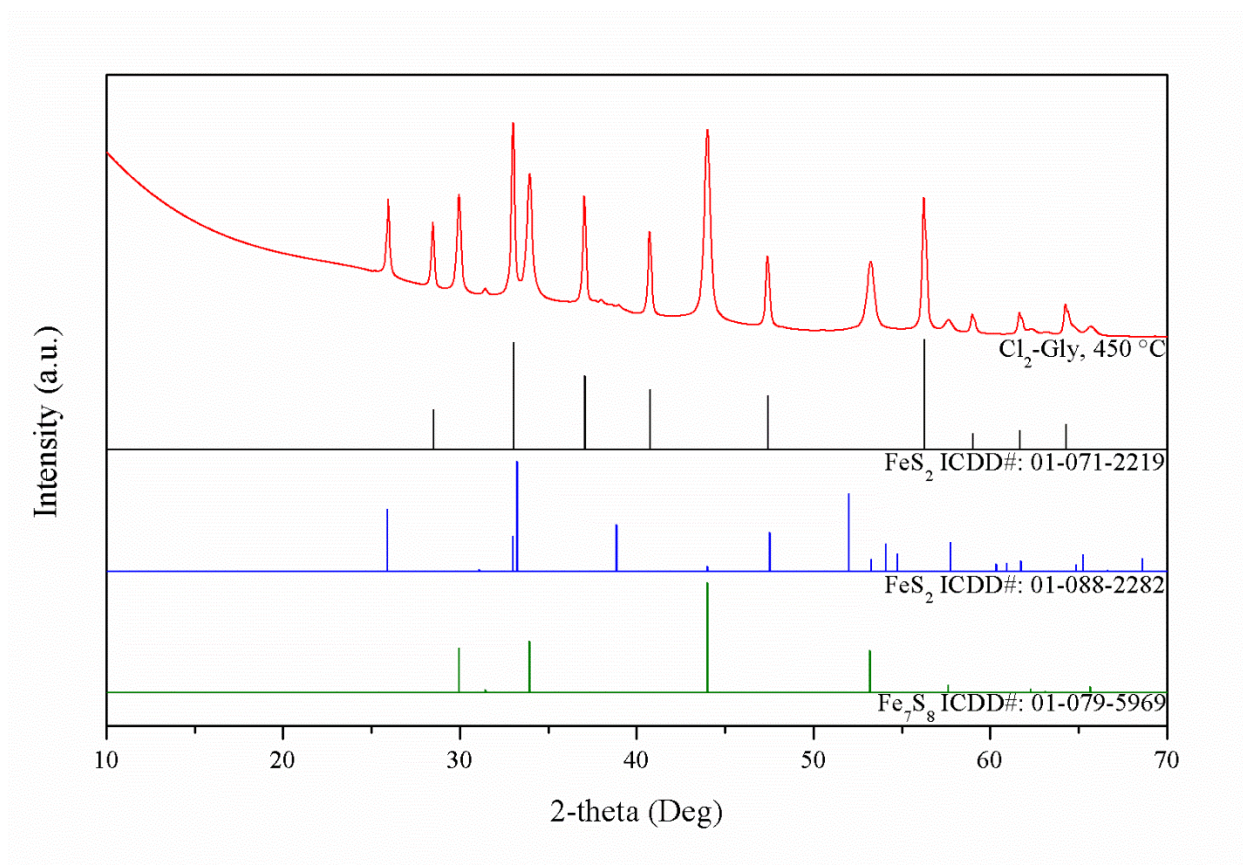


Figure 4.14. XRD patterns of the Cl₂-Gly series when annealed at 450 °C.

Cl ₂ -Gly, 450 °C				
Annealing Temperature	Observed Phases	ICDD No.	% Phase	Crystallite Size (nm)
450 °C	FeS ₂	01-071-2219	26.3 ± 1.8	42.9 ± 1.6
	Fe ₇ S ₈	01-079-5969	30.0 ± 3	145.9 ± 8.9
	FeS ₂	01-088-2282	43.0 ± 3	36.1 ± 21.1

Table 4.7. Rietveld refinement data of the Cl₂-Gly series when annealed at 450 °C.

At 500 °C, the Cl₂-Gly series displayed the familiar phase shift mechanism that was also observed in the Acac-Gly series. According to the refinement result in Table 4.8, FeS₂ went from

the majority phase at 450 °C to the minority phase with the least percentage phase composition at 10.2 ± 0.7 %. Fe_7S_8 phase enjoyed a significant increase in phase composition at 66.0 ± 0.7 % and took over as the majority phase of this stage of the experiment. Lastly, Fe_2GeS_4 , the desired product phase, became detectable at 500 °C with the percentage phase composition at 23.8 ± 1.4 %. Shown in Figure 4.15, the measured XRD pattern was in consistency with the Rietveld refinement results and had already adopted the reflection of Fe_2GeS_4 with impurity peaks dotting across the pattern. Based on the % Phase tabulated, it was observed that once again Fe_7S_8 increased, from the minority to the absolute majority phase, with the drastic decrease in FeS_2 phase, from the majority down to the minority. The same trend was observed in the Acac-Gly series across two ranges of temperatures, 400 °C to 450 °C and 500 °C to 550 °C. In addition, 500 °C for Cl_2 -Gly was the first and the only temperature stage where FeS_2 , Fe_7S_8 and Fe_2GeS_4 coexisted, which was slightly delayed when compared to the first temperature stage of three-phase coexistence that was observed to have occurred at 450 °C.

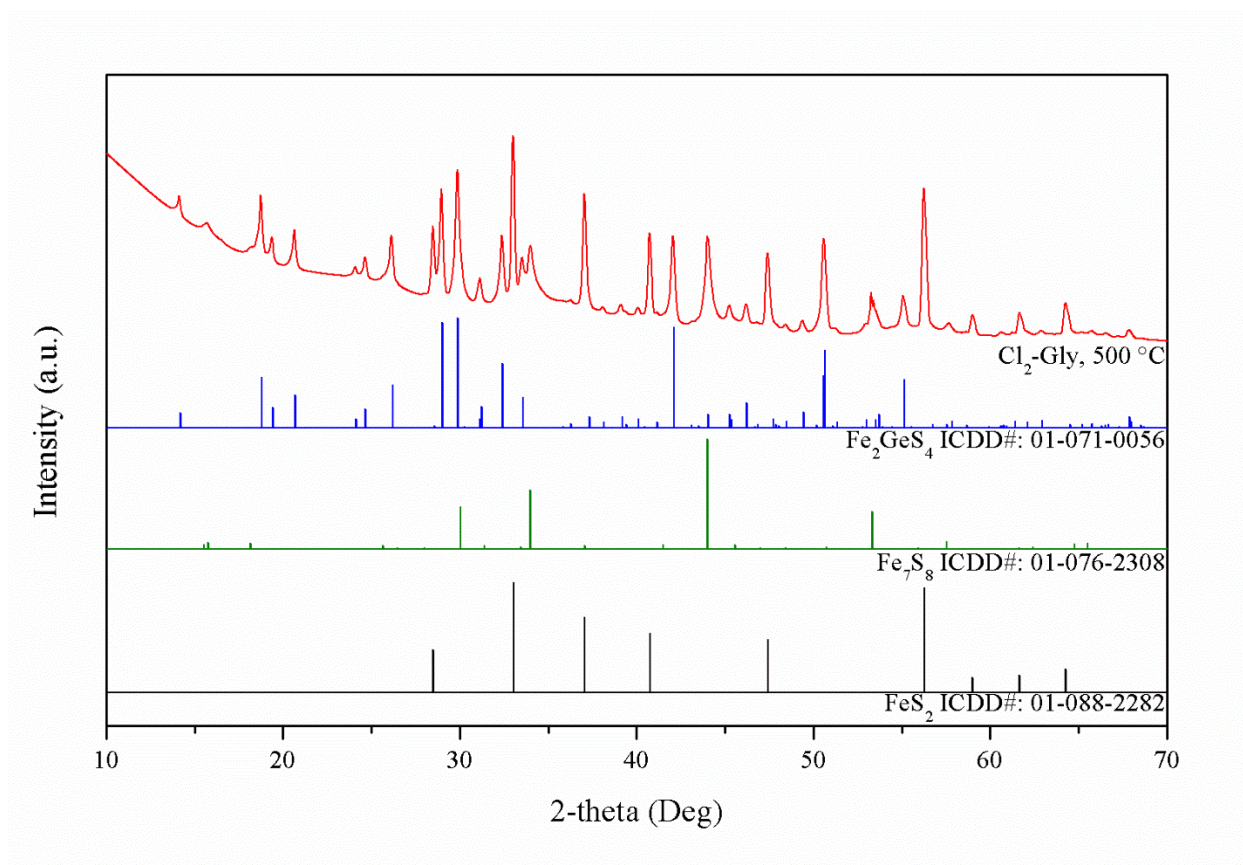


Figure 4.15. XRD patterns of the Cl₂-Gly series when annealed at 500 °C.

Cl ₂ -Gly, 500 °C				
Annealing Temperature	Observed Phases	ICDD No.	% Phase	Crystallite Size (nm)
500 °C	Fe ₂ GeS ₄	01-071-0056	23.8 ± 1.4	27.4 ± 0.3
	Fe ₇ S ₈	01-076-2308	66.0 ± 0.7	8.0 ± 0.9
	FeS ₂	03-065-3321	10.2 ± 0.7	43.4 ± 0.5

Table 4.8. Rietveld refinement data of the Cl₂-Gly series when annealed at 500 °C.

Regardless of the delay, Cl₂-Gly series behaved very similarly when it comes to the phase shift mechanism, and it was very much evident at the 550 °C annealing temperature stage. Based on the Rietveld refinement result shown in Table 4.9, the three-phase coexistence had once again

ceased to be as the pyrite phase FeS_2 converted fully following the $50\text{ }^\circ\text{C}$ increment in annealing temperature. Both series of precursor combination showed the similar trend to have removed FeS_2 completely and left only Fe_7S_8 and Fe_2GeS_4 phases at $550\text{ }^\circ\text{C}$. In addition, the two phases were determined by the refinement to be close to equal in % Phase with Fe_7S_8 at $57.6 \pm 0.7\%$ and Fe_2GeS_4 at $42.4 \pm 1.1\%$, a trend that was also shared by the Acac-Gly series. The XRD pattern, shown in Figure 4.16, was observed to have a significant reduction in the peak intensity to those belonged to Fe_7S_8 with the increase in annealing temperature to $550\text{ }^\circ\text{C}$. Reaction mechanism wise, both series has shared much in common despite the delayed conversion from FeS_2 to Fe_7S_8 . As stated above, the Fe_7S_8 and Fe_2GeS_4 was only close to equal with the % Phase for former slightly higher than the latter when compared to the exact same % Phase shared by both phases in the Acac-Gly series. It was possible that the delayed conversion of FeS_2 had also led to the delay in reaction that would cause the phase shift from Fe_7S_8 to Fe_2GeS_4 .

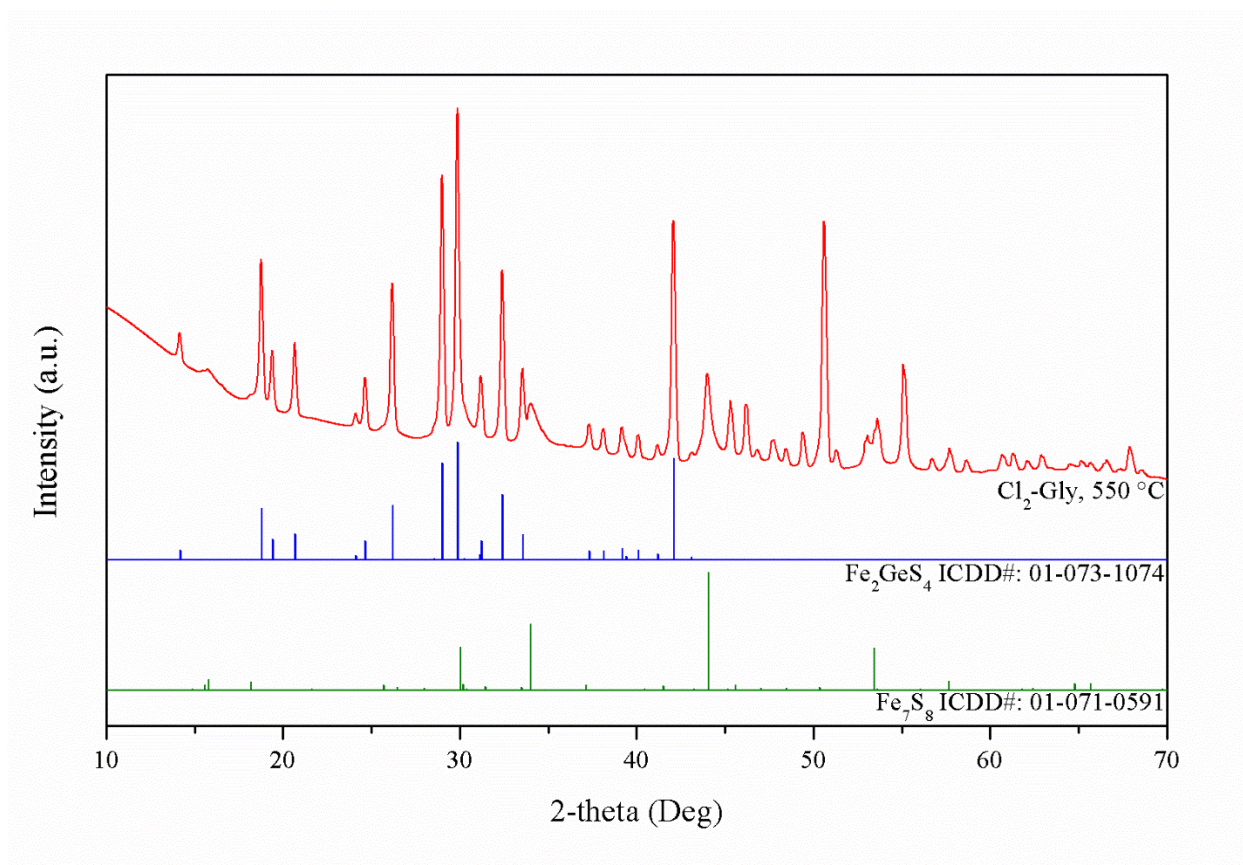


Figure 4.16. XRD patterns of the Cl₂-Gly series when annealed at 550 °C.

Cl ₂ -Gly, 550 °C				
Annealing Temperature	Observed Phases	ICDD No.	% Phase	Crystallite Size (nm)
550 °C	Fe ₂ GeS ₄	01-073-1074	42.4 ± 1.1	31.75 ± 1.8
	Fe ₇ S ₈	01-071-0591	57.6 ± 0.7	6.7 ± 0.5

Table 4.9. Rietveld refinement data of the Cl₂-Gly series when annealed at 550 °C.

The 600 °C annealing temperature stage for the Cl₂-Gly series confirmed the delay in the reaction that was brought to attention with the smaller formation of the Fe₂GeS₄ phase. As shown in Figure 4.17, the XRD pattern of the Cl₂-Gly product, although still exhibited the Fe₂GeS₄

reflection, still contain a few peaks that belonged to another binary phase. Comparing the results of the Rietveld refinement, it was simulated that the Fe_2GeS_4 phase had increased to $63.9 \pm 1.8\%$ and become the majority phase of the product. An unexpected phase, once again unique to the Cl_2 -Gly series only, was detected was the emergence of the FeS phase, also known as troilite, which was determined to have $36.1 \pm 0.5\%$ in phase composition at this stage of the experiment. As stated above, the delay in the phase shift mechanism that was on display throughout the entire annealing temperature test in the Cl_2 -Gly series had also manifested at this specific stage as well. When comparing to the % Phase of Fe_2GeS_4 of the Acac-Gly series, with $72.5 \pm 0.5\%$, of the same annealing temperature stage, the Cl_2 -Gly was decidedly the lesser product with a smaller formation of Fe_2GeS_4 phase with only $63.9 \pm 1.8\%$ at $600\text{ }^\circ\text{C}$. Yet, despite the significant 8.6% difference between the two series, it was worth noting that both series had very similar growth in % Phase during the same $50\text{ }^\circ\text{C}$ increment, with the Acac-Gly series seeing a 22.5% increase while the Cl_2 -Gly series seeing a 21.5% increase in the formation of Fe_2GeS_4 phase, which had only 1% difference in percentage growth. With only the precursor combinations changed while retaining the exact same experimental setup, it was concluded that Cl_2 -Gly series, with the replacement of $\text{Fe}(\text{acac})_3$ to FeCl_2 , had delayed the phase shift between FeS_2 to Fe_7S_8 and the formation of Fe_2GeS_4 by at least $50\text{ }^\circ\text{C}$. A more precise temperature effect could be studied if a narrower temperature increment was implemented for the experiment.

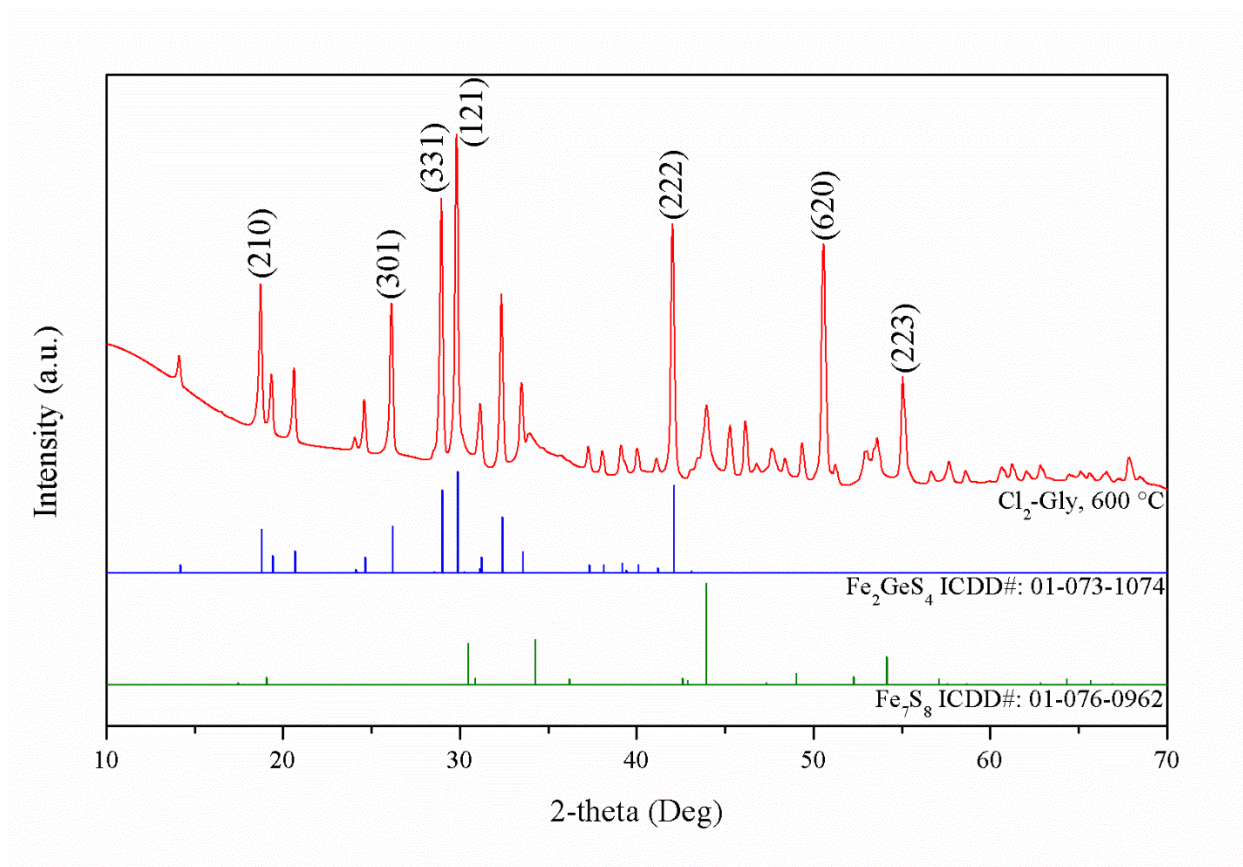


Figure 4.17. XRD patterns of the Cl₂-Gly series when annealed at 600 °C.

Cl ₂ -Gly, 600 °C				
Annealing Temperature	Observed Phases	ICDD No.	% Phase	Crystallite Size (nm)
600 °C	Fe ₂ GeS ₄	01-073-1074	63.9 ± 1.8	34.2 ± 0.3
	FeS	01-076-0962	36.1 ± 0.5	5.0 ± 0.3

Table 4.10. Rietveld refinement data of the Cl₂-Gly series when annealed at 600 °C.

4.2.3. Cl₃-Gly Series Annealing Temperature Test

In the previous section of the research, the XRD pattern for the Cl₃-Gly series, shown in Figure 4.5, had displayed a pattern with no detectable impurity peaks and overall sharper and more intensified peaks, which were all the signs of a high quality and phase pure product. The Cl₃-Gly series posed as becoming the best of the precursor combinations proposed in this research that would produce the Fe₂GeS₄ nanoparticles suitable for the photovoltaic effects. Much like the previous two annealing temperature tests, the same examination with XRD in combination of the Rietveld refinement were done to study the effect of utilizing FeCl₃ as the iron precursor has on the phase shift mechanism in 50 °C increments from 400 °C to 600 °C and to determine the quality of the product overall. Detailed comparisons with the previous two series were also analyzed to determine if a general trend between the three precursor combinations could be realized.

At the 400 °C annealing temperature stage, the XRD pattern obtained for Cl₃-Gly, as displayed at Figure 4.18, has shown a mixture of two phases. One phase could be assigned to FeS₂ as similar reflections has been observed previously, while another phase, more specifically the peak showing at $\theta = 44^\circ$, could not be easily assigned to any specific iron binary phases. Typically, a $\theta = 44^\circ$ could be assigned to Fe₇S₈ as it was one of the iconic pyrrhotite peaks, which would be shown in later patterns in the series. In this case, however, since the peak was on its own without other pyrrhotite peaks present to support the presence of a pyrrhotite phase, it was considered an outlier and we instead referred to the refinement for answer. The simulated result provided by the Rietveld refinement concluded that there were two phases at this stage of

the experiment, and both phases belonged to FeS₂ pyrite and together attributed to the entirety of the phase composition. This result somewhat echoed the Acac-Gly series, where a single-phase FeS₂ was detected for the 400 °C experiment. This is the first and only instance that the Rietveld refinement does not entirely agree with the measured XRD pattern that the simulation was based on. Regardless, the general phase composition of this phase was concluded to be the phase of FeS₂ that had attributed to $66 \pm 8\%$, which matched very well with the rest of the reflection.

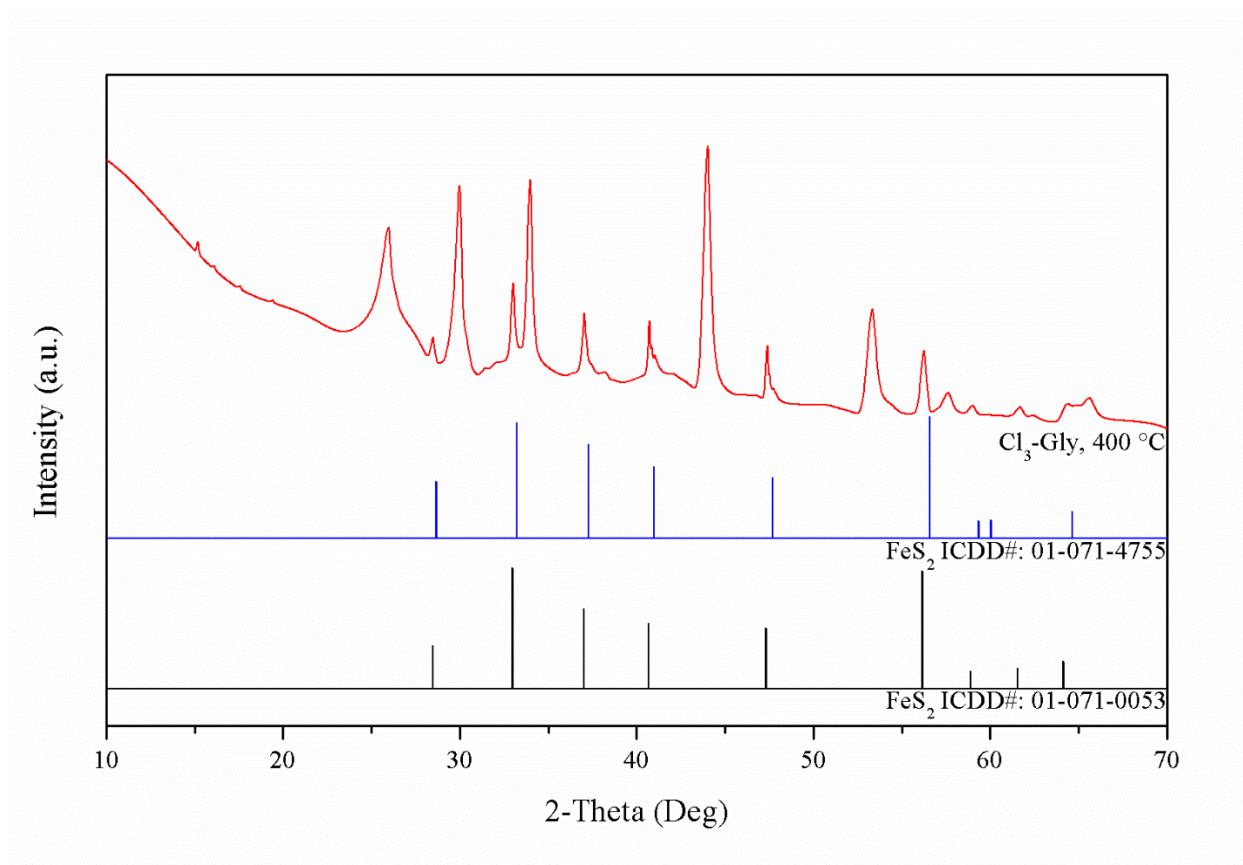


Figure 4.18. XRD patterns of the Cl₃-Gly series when annealed at 400 °C.

Cl₃-Gly, 400 °C				
Annealing Temperature	Observed Phases	ICDD No.	% Phase	Crystallite Size (nm)
400 °C	FeS ₂	01-071-0053	34 ± 4	77.1 ± 26.7
	FeS ₂	01-071-4755	66 ± 8	12.9 ± 2

Table 4.11. Rietveld refinement data of the Cl₃-Gly series when annealed at 400 °C.

Increasing the annealing temperature to 450 °C for the Cl₃-Gly series saw the removal of two peaks at 37.27° and 40.98° on the XRD pattern, shown in Figure 4.19, that had previously belonged to both of the FeS₂ phases assigned by the Rietveld refinement. Thus, it should be

concluded that either phases of FeS₂ from the previous stage was converted into other phases. The Rietveld refinement data, shown in Table 4.12, for this stage of the experiment showed an even more complex phase composition with up to four phases present at this annealing temperature stage, two phases of FeS₂, one phase of FeS and one phase of Fe₇S₈. The two phases FeS₂ that was observed to have attributed as the majority phase of this product with $0.2 \pm 0.1\%$ and $73.6 \pm 10.00\%$ as their percentage phase composition. The FeS phase was determined to have $17.3 \pm 1.1\%$ as the second most iron binary phase while the Fe₇S₈ phase as the minority phase with the least percentage phase composition at $8.9 \pm 0.5\%$. Although complicated on the outlook, the four phases could essentially be narrowed down into simply two umbrella categories of iron chalcogenides, one was assumed to be the pyrite material with the iron disulfide molecular formula and structure while the rests could be assumed to be the S-deficient phases as part of the pyrrhotite materials, which was shared by FeS and Fe₇S₈. With this assumption in mind, the Cl₃-Gly product at 450 °C essentially had been converted from a solely FeS₂ product at 400 °C to a product with a majority phase of pyrite and minority phases of pyrrhotite at 450 °C. This observation was consistent with the experimental results seen in previous precursor combinations as well as agreeable based on the proposal by Zhang et. al. (2012), with delay in phase shift mechanism possibly due to the inclusion of germanium²⁴.

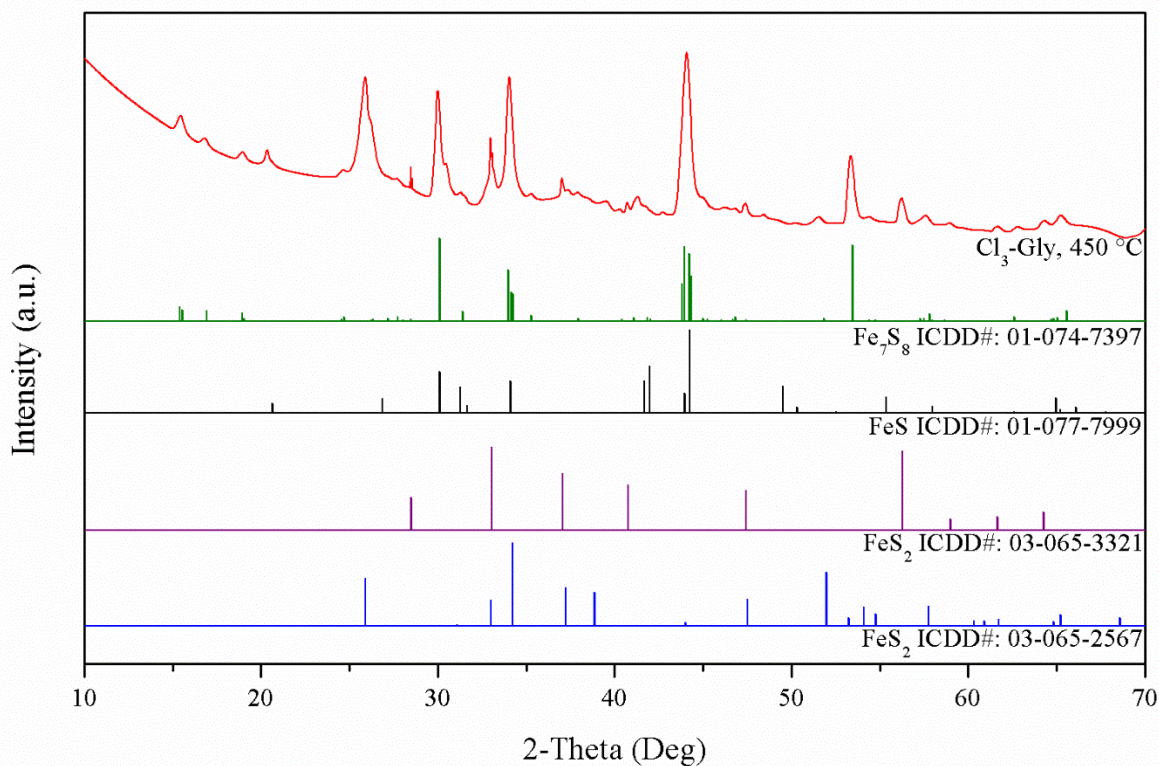


Figure 4.19. XRD patterns of the Cl₃-Gly series when annealed at 450 °C.

Cl ₃ -Gly, 450 °C				
Annealing Temperature	Observed Phases	ICDD No.	% Phase	Crystallite Size (nm)
450 °C	FeS ₂	03-065-3321	0.2 ± 0.1	53.3 ± 2.6
	Fe ₇ S ₈	01-074-7397	8.9 ± 0.5	15.1 ± 2.0
	FeS ₂	03-065-2567	73.6 ± 10.0	8.3 ± 4.6
	FeS	01-077-7999	17.3 ± 1.1	21.1 ± 0.7

Table 4.12. Rietveld refinement data of the Cl₃-Gly series when annealed at 450 °C.

The 500 °C annealing temperature stage for Cl₃-Gly continued to display unique phase shift behaviors when comparing to the previous two series. First and foremost, the Cl₃-Gly series still had not produced any phase of Fe₂GeS₄ yet while the Acac-Gly series had already achieved a majority phase of Fe₂GeS₄ and the Cl₂-Gly at least had a minority phase in the product. This discovery only confirmed with the previous delay assumption of the delay in phase shift mechanism due to the change in precursor combinations that was observed of the Cl₂-Gly series. Instead, shown in Table 4.13, the majority phase for 500 °C was taken by Fe₇S₈ at 53 ± 4%. The product had two other remaining phases, both were assigned as pyrites by the Rietveld refinement but one with 11 ± 1% and the other with 36 ± 2% for their associated phase compositions. Figure 4.20 showed the XRD pattern obtained for the Cl₃-Gly series at 500 °C, and the reflection was shown to be consistent with the refinements since the peaks shown could be assigned to both pyrrhotite and pyrite. This annealing temperature stage for the Cl₃-Gly series, when condensing the phases by their associated material phase, displayed an almost equivalent phase composition between the pyrrhotite with 53 ± 4% and the pyrite with an overall of 47 ± 2%. The pyrrhotite phase saw an massive 44.1% increase in phase composition by increasing the annealing temperature from 450 °C. Even though the annealing temperature stage was different, the stages where the massive increase in Fe₇S₈ pyrrhotite phase that were observed all shared the similarity that they were the specific annealing temperature stage just prior to the synthesis of Fe₂GeS₄. The same behavior was found to be true for the Cl₃-Gly series as well.

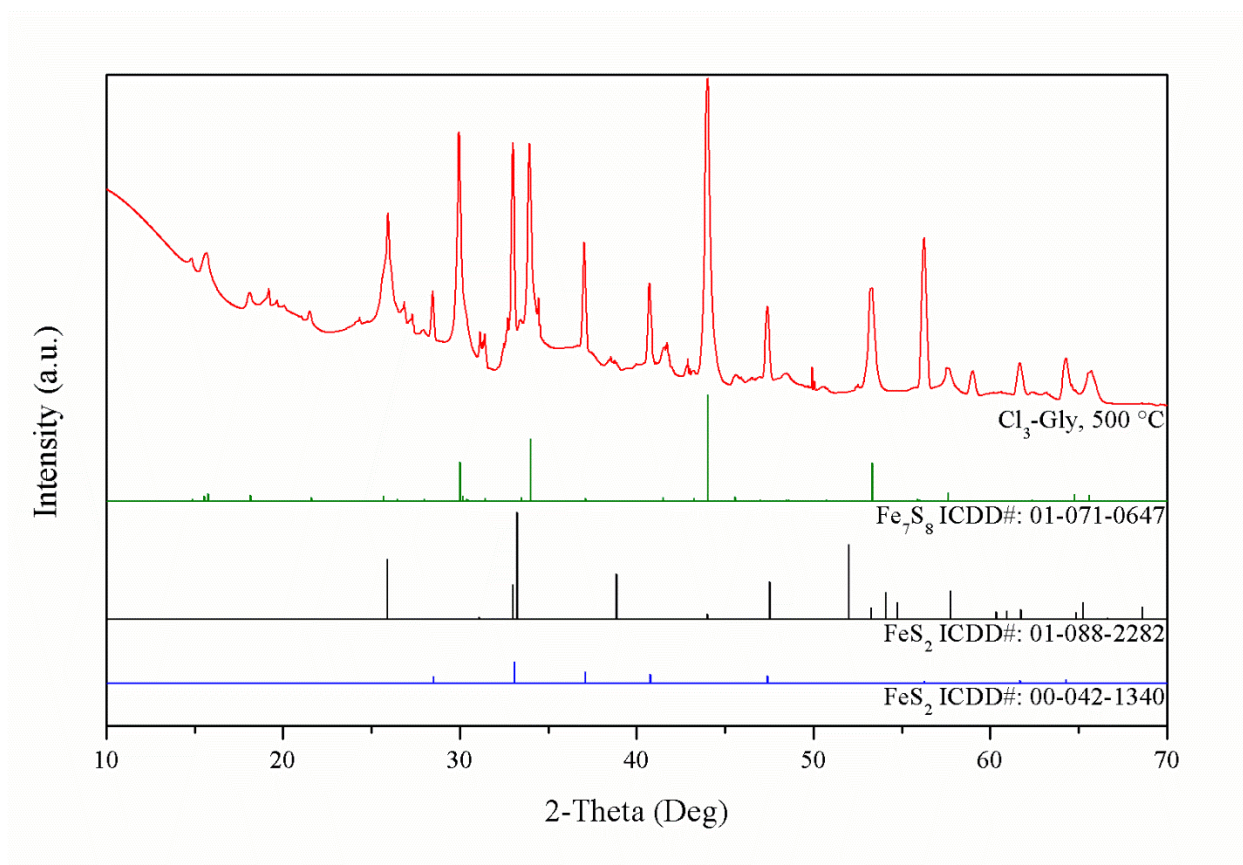


Figure 4.20. XRD patterns of the Cl₃-Gly series when annealed at 500 °C.

Cl₃-Gly, 500 °C				
Annealing Temperature	Observed Phases	ICDD No.	% Phase	Crystallite Size (nm)
500 °C	FeS ₂	00-042-1340	11 ± 1	44.9 ± 0.9
	Fe ₇ S ₈	01-071-0647	53 ± 4	13.9 ± 0.7
	FeS ₂	01-088-2282	36 ± 2	70.5 ± 22.3

Table 4.13. Rietveld refinement data of the Cl₃-Gly series when annealed at 500 °C.

The Cl₃-Gly series, although previously showing different behaviors including the emergence of multiple pyrite phases at lower annealing temperatures, had shown to share the

same trend that was in consistency with the previous two precursor combinations. At 550 °C annealing temperature stage, which followed right after the massive increase in pyrrhotite phase at 500 °C, produced the desired product, the Fe₂GeS₄ phase. It was noted that the synthesis of Fe₂GeS₄ at 550 °C was a rapid reaction as it attributed to 71.9 ± 1.2% of the phase composition of the product with only 50 °C of temperature increment from the previous annealing stage. The only minority phase for this product was assigned to the Fe₇S₈ phase by the Rietveld refinement with 28.1 ± 1.9%. The lack of presence of any pyrite phases observed at previous annealing temperature stages was speculated to have been rapidly converted into the Fe₇S₈ phase following the temperature increase, which had very rapidly reacted with germanium to form Fe₂GeS₄ during the reaction. Figure 4.21 illustrated the XRD pattern obtained for the Cl₃-Gly series at 550 °C with a significant change to the reflection that heavily resembled Fe₂GeS₄ with only three identifiable minority peaks dotted across the pattern, thus the pattern was consistent with the Rietveld refinement result.

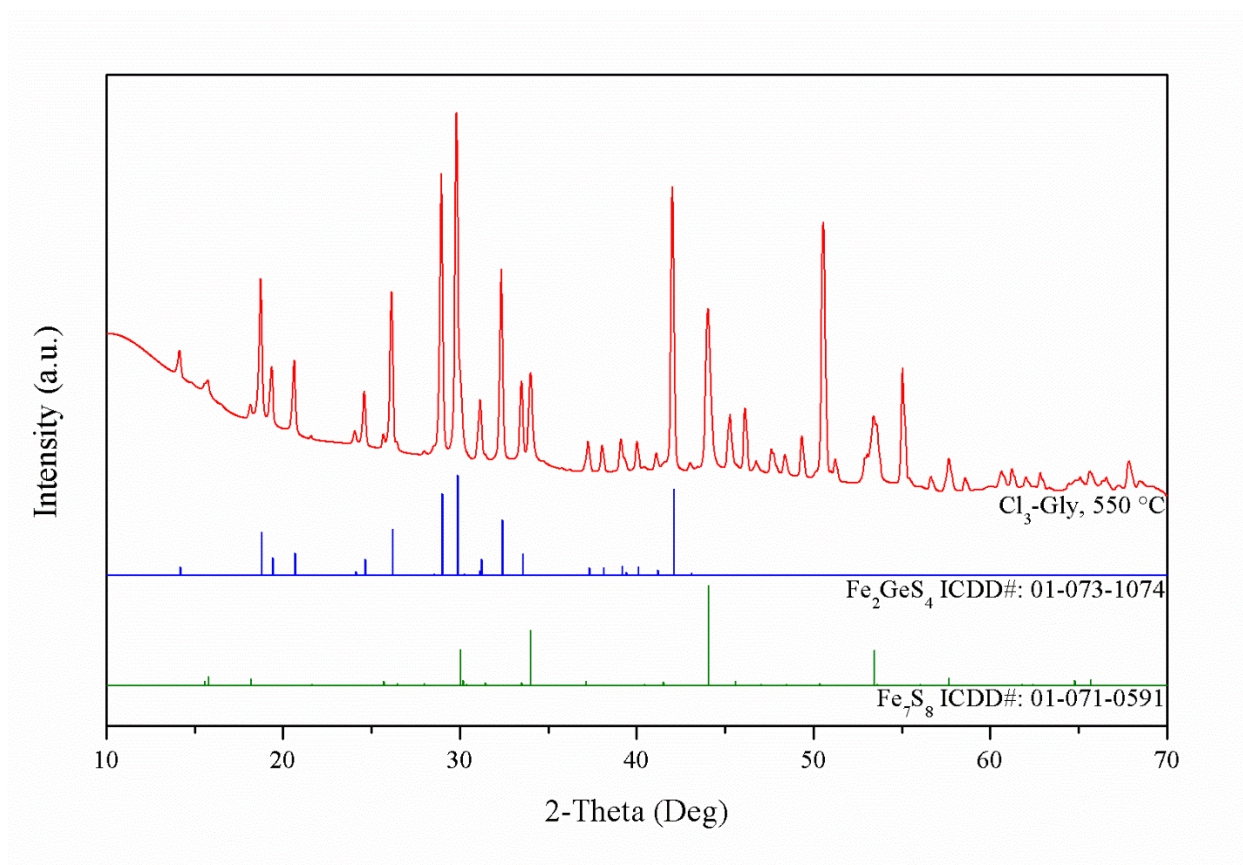


Figure 4.21. XRD patterns of the Cl₃-Gly series when annealed at 550 °C.

Cl ₃ -Gly, 550 °C				
Annealing Temperature	Observed Phases	ICDD No.	% Phase	Crystallite Size (nm)
550 °C	Fe ₂ GeS ₄	01-073-1074	71.9 ± 1.2	32.7 ± 0.4
	Fe ₇ S ₈	01-071-0591	28.1 ± 1.9	27.1 ± 0.8

Table 4.14. Rietveld refinement data of the Cl₃-Gly series when annealed at 550 °C.

Increasing the annealing temperature by 50 °C to reach for 600 °C for the Cl₃-Gly series saw the formation of the pure Fe₂GeS₄ product. The XRD pattern obtained for this stage of the experiment was shown in Figure 4.22, had found that all identifiable peaks could be assigned to

the literature Fe_2GeS_4 phase in the ICDD Database. The high peak intensity of the XRD pattern as well as the sharpened peaks was evident that the synthesized product was of high crystallinity. These speculations were confirmed by the Rietveld refinement as the result in Table 4.15 showed a phase pure Fe_2GeS_4 product with the percentage phase composition assigned at $100 \pm 1.8\%$. The last 50°C increment saw the complete reaction of Fe_7S_8 with germanium to form the high quality, phase pure product of Fe_2GeS_4 synthesized with the precursor combination of the $\text{Cl}_3\text{-Gly}$ series at 600°C for 2 hr.

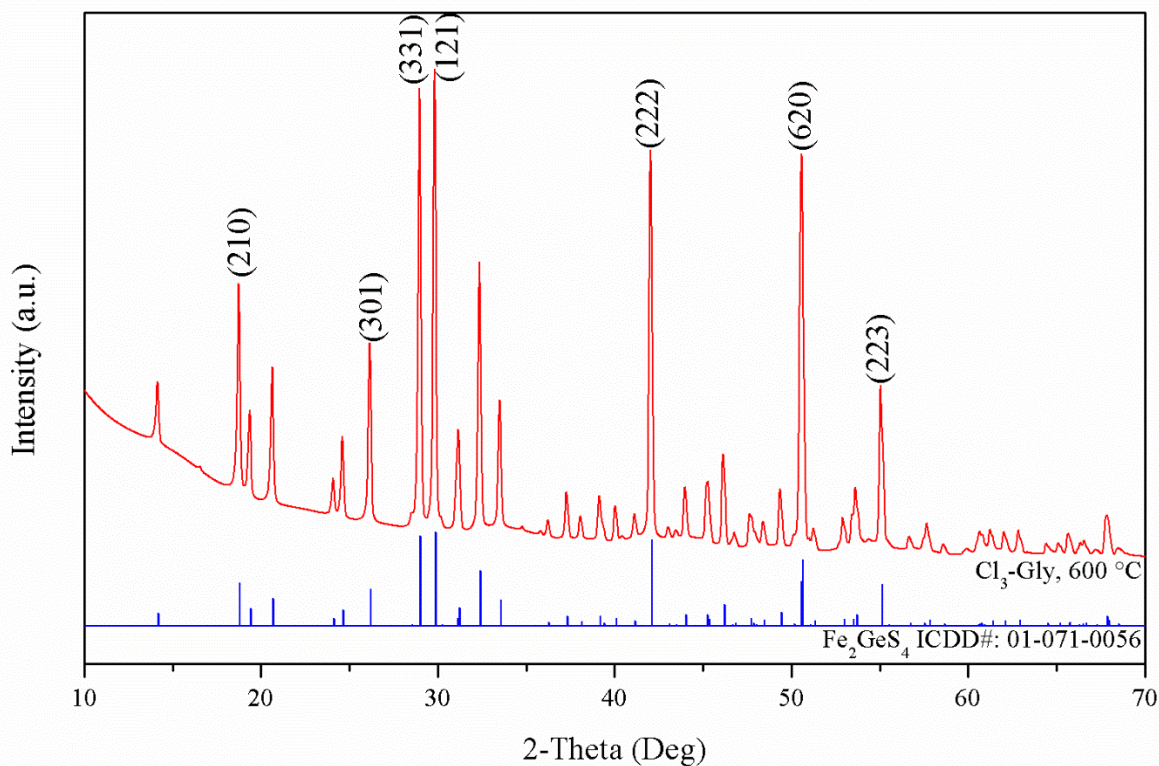


Figure 4.22. XRD patterns of the $\text{Cl}_3\text{-Gly}$ series when annealed at 600°C .

Cl ₃ -Gly, 600 °C				
Annealing Temperature	Observed Phases	ICDD No.	% Phase	Crystallite Size (nm)
600 °C	Fe ₂ GeS ₄	01-071-0056	100 ± 1.8	35.8 ± 0.4

Table 4.15. Rietveld refinement data of the Cl₃-Gly series when annealed at 600 °C.

The Cl₃-Gly series data that was obtained for this research painted a clear picture of yet another phase shift pattern unique to this specific precursor combination over 400 °C to 600 °C. However, a shared mechanism that drove these solid-state syntheses of Fe₂GeS₄ was realized when comparing the overall change of phase compositions to one another. The Cl₃-Gly series had a very delayed reaction to synthesize Fe₂GeS₄ when comparing to its predecessors, hinting the high activation energy required to initiate the reaction. Considering the change of oxidation state from Fe³⁺ to Fe²⁺ necessary due to the latter state was used to synthesize Fe₂GeS₄, an additional energy requirement was required to make the transition and thus a higher annealing temperature stage was suspected to be crucial in order to meet higher activation energy requirement for the Fe₂GeS₄ phase to appear for the Cl₃-Gly series. Yet, once the reaction had been initiated, the synthesis was rapid and robust, as shown in the rapid growth of 71.9 ± 1.2% of the Fe₂GeS₄ phase at 550 °C. This growth speed was unmatched by the two other series we had examined previously in this research. In addition, the percentage phase composition of the Cl₃-Gly series at 550 °C was found to be very similar to that of the Acac-Gly series at 600 °C but had only achieved the % Phase in mere 50 °C raise, indicating that the trichloride precursor series could form a far more robust reaction than the acetylacetonate precursor series. Lastly, the Cl₃-Gly series was the only series out of the three that had successfully yielded the high quality,

single-phase Fe_2GeS_4 product in the selected annealing temperature range, thus, as a result, has shown the full capability of providing the ideal material for the manufacturing of highly efficient photovoltaic devices at moderate temperature in short reaction time, which will be further discussed in the next chapter.

The phase-pure $\text{Cl}_3\text{-Gly}$ product was analyzed with TGA to determine its thermal stability, and the result was shown in Figure 4.23 below. After a slight loss of mass at lower temperatures, indicating the removal of excess organics left over by the $\text{Ge}[(\text{C}_2\text{H}_2\text{O}_3)_2(\text{H}_2\text{O})_2]$ precursor, the analysis displayed the onset temperature of thermal decomposition of the Fe_2GeS_4 product was at $625.8\text{ }^\circ\text{C}$, which is a significant improvement from the low onset temperature for decomposition of FeS_2 , which is $160\text{ }^\circ\text{C}$ ²⁶. One thing worth noting is also the high scalability and high yield the solid-state synthesis practiced in this specific research can provide. On average, a batch of Fe_2GeS_4 nanoparticle powder utilizing $\text{Cl}_3\text{-Gly}$ method has the yield of 612.275 mg with the percent yield at 97.94 %. The considerable large yield of materials is significant for future commercial adaptation as a single batch of nanoparticle powders could produce up to three batches of nanoparticle ink, as it will be discussed in the next chapter.

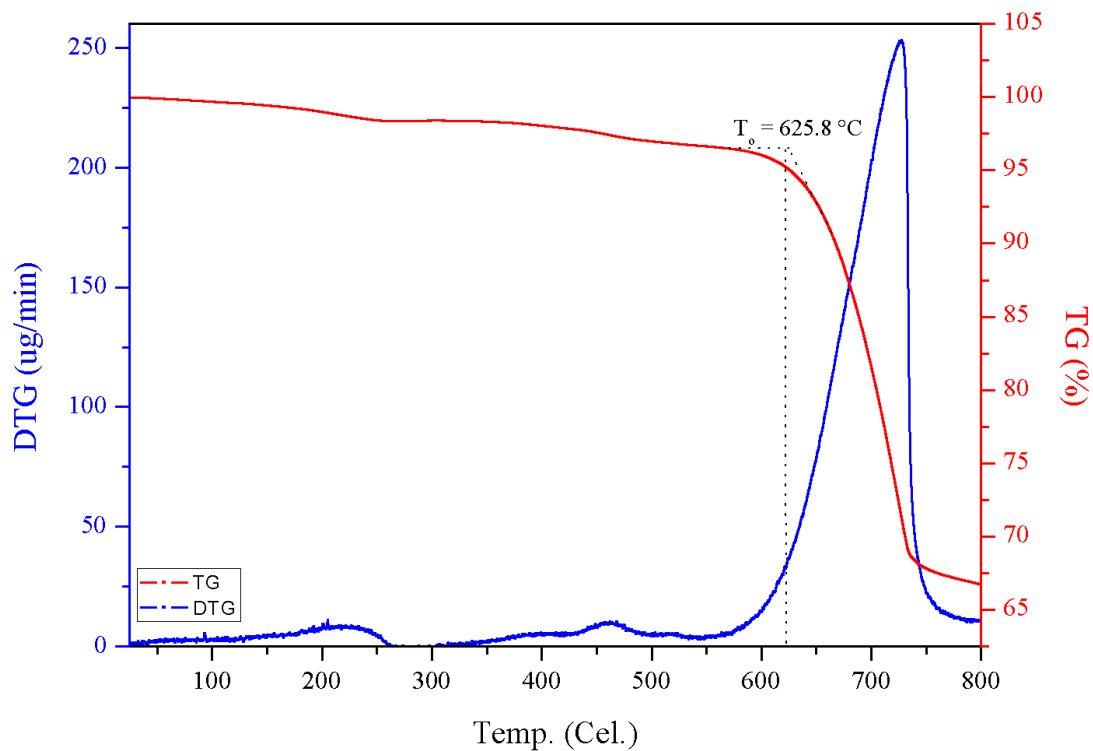


Figure 4.23. Thermalgravimetric analysis of the 600 °C Cl₃-Gly product of Fe₂GeS₄.

4.3. Discussion of Iron Sulfides Phase Shift Paradigm

Despite operating under the same procedures and conditions, the three precursor combination series, the Acac-Gly, Cl₂-Gly and the Cl₃-Gly series, had shown many differences when it comes to the variety of the detectable phases at each annealing temperature stages. Some phases were even unique to their specific series. Yet, throughout this research, many shared trends and similarities of were observed across all three series, and their repeating occurrences were strongly believed to be not merely coincidental to their respective experimental setup but fundamental to the phase shift mechanism of iron sulfides or even iron chalcogenides in general.

Pyrite was theorized to be an ideal photovoltaic product but was plagued by the phase instability issue, where a phase pure FeS_2 pyrite has the tendency to phase change into the S-deficient $\text{Fe}_{1-\delta}\text{S}$ pyrrhotite phases that had many disadvantageous electronic properties. This trend was further studied by Zhang et. al. and it was discovered that FeS_2 would begin the conversion into $\text{Fe}_{1-\delta}\text{S}$ as early as $160\text{ }^\circ\text{C}$ on the surface and a rapid and full conversion would take place from $410\text{ }^\circ\text{C}$ to $425\text{ }^\circ\text{C}$ ²⁴. Although Zhang's study covered only the conversion of the phase pure FeS_2 , many similarities in the trends were found in the scope of this very study as well with the inclusion of germanium to produce Fe_2GeS_4 via solid-state synthesis²⁴.

For the Acac-Gly series, it was observed that the phase composition begun as a single-phase FeS_2 product at $400\text{ }^\circ\text{C}$. The phase purity was gone with the increase of annealing temperature by $50\text{ }^\circ\text{C}$, which Fe_7S_8 became the majority phase, Fe_2GeS_4 phase attributed to the second most and FeS_2 phase became the minority. Further annealing up to $500\text{ }^\circ\text{C}$ observed the increasing of Fe_2GeS_4 at the cost of the diminishing Fe_7S_8 phase while the FeS troilite phase took a back seat in the conversion process and stayed almost the same % Phase. The complete elimination of FeS_2 at $550\text{ }^\circ\text{C}$ left only the Fe_2GeS_4 and Fe_7S_8 phase with equal % Phase in the product. By the $600\text{ }^\circ\text{C}$, the Fe_2GeS_4 phase was observed to have increased at the cost of the Fe_7S_8 phase.

For the Cl_2 -Gly series, it was observed Fe_7S_8 had already begun to form at $400\text{ }^\circ\text{C}$, and the experiment started with the product being a mixture of pyrite phases and Fe_7S_8 phases for both the $400\text{ }^\circ\text{C}$ to $450\text{ }^\circ\text{C}$ stages. At $500\text{ }^\circ\text{C}$, Fe_7S_8 phase took over as the majority phase of the product and it was observed in the same product that Fe_2GeS_4 had begun to form, delayed by

50 °C when compared to the Acac-Gly series. Increasing the annealing temperature to 550 °C once again saw the elimination of FeS₂ phase completely and leaving only the Fe₇S₈ and Fe₂GeS₄ phases. The end of the study for this series at 600 °C showed the Fe₂GeS₄ had a very similar phase growth for the last 50 °C temperature increments as the Acac-Gly series at the cost of the S-deficient phase, FeS.

For the Cl₃-Gly series, it was observed that FeS₂ pyrite, although divided into two phases by the refinement, was the only existing material at 400 °C. Increasing the annealing temperature to 450 °C showed the emergence of the S-deficient phases as the minority while FeS₂ phases stayed as the majority. The role swapped with the increase in annealing temperature to 500 °C and it was observed the increase of pyrrhotite phase becoming the majority phase was again at the cost of the pyrite phases. The elimination of FeS₂ phases entirely in the occurred at 550 °C, which left only the Fe₂GeS₄, as the majority phase, and Fe₇S₈, as the minority phase. At the 600 °C annealing temperature stage, the reaction was completed and a phase pure Fe₂GeS₄ was acquired, which was evident in the complete elimination of the Fe₇S₈ phase in the product.

The phase shift between the three phases all followed the same pattern. FeS₂ pyrite phase, with its low temperature requirement to synthesize, was always the first detectable phase in the solid-state synthesis. For the Acac-Gly series, the phase composition of the product began as a single-phase FeS₂ product at 400 °C. For the Cl₃-Gly series, the FeS₂ pyrite, although divided into two phases by the refinement, was the only iron chalcogenides present at 400 °C. Disregarding the outlier shown at 400 °C, Cl₂-Gly series displayed a combination of FeS₂ as the

majority phase and Fe_7S_8 as the minority phase at 450 °C, where the former phase was speculated to be undergoing the conversion into the latter phase at 450 °C.

The FeS_2 pyrite majority phase would always be replaced by a Fe_7S_8 pyrrhotite majority with the increase in annealing temperature. From the Acac-Gly series, it was observed that the phase purity of FeS_2 was removed once the annealing temperature was raised to 450 °C, when Fe_7S_8 became the majority phase and FeS_2 phase became the minority. The Cl_3 -Gly series observed the same trend at 500 °C where the Fe_7S_8 took over as the majority phase with a 44.1% phase growth. Similar trend was displayed by the Cl_2 -Gly series with the increase of Fe_7S_8 at 500 °C, becoming the majority phase in the process. In consistency with the report by Zhang et. al., this study observed multiple cases where signs of the conversion from FeS_2 and Fe_7S_8 had taken place across multiple annealing stages of the solid-state synthesis²⁴. The phase shift was one direction in most cases, and the temperature stages where the elimination of FeS_2 had occurred were also the last stages where this iron binary phase would present in the product in each own perspective precursor combinations.

The Fe_2GeS_4 product phase was always the last of phases to be synthesized and it utilized the Fe_7S_8 as the molecular precursor required for solid-state synthesis. In many instances, it was observed that it was during the reduction of Fe_7S_8 phase which the Fe_2GeS_4 phase was generated, thus it was theorized that, by increasing the annealing temperature, the Fe_7S_8 pyrrhotite phase would begin to start the reaction with the germanium present in the molecular precursors. It was observed in the Acac-Gly series, the equal percentage phase composition of the Fe_2GeS_4 and Fe_7S_8 phases at 550 °C changed into Fe_2GeS_4 majority following the reduction of the Fe_7S_8 phase

at 600 °C. Similarly, for the Cl₃-Gly series, a phase pure Fe₂GeS₄ was finally formed after eliminating the Fe₇S₈ phase altogether when moving the annealing temperature stage from 550 °C to 600 °C. In both instances, it was at the final stage of the annealing temperature test, we had observed the rapid reduction of Fe₇S₈ and the robust generation of Fe₂GeS₄ that followed it.

At the beginning of the research, it was hypothesized that FeS₂ could act as the precursor to react with germanium to form Fe₂GeS₄ in a solid-state synthesis condition. This was disputed as there was no direct evidence of FeS₂ phases were the sole contributor to the growth of Fe₂GeS₄ phase. During the Acac-Gly series, it was even observed that the FeS₂ phase remained similarly in phase composition, with a slight growth of 1%, while the Fe₂GeS₄ took over as the majority phase from Fe₇S₈ following the increase in annealing temperature from 450 °C to 500 °C. Accompanied by the fact that Fe₂GeS₄ was typically detected at higher temperature stages, especially so for the Cl₃-Gly series, and FeS₂ tended to be eliminated prior to that stage, it was concluded that the FeS₂ phase does not act as a direct precursor to the formation of Fe₂GeS₄, rather it was an indirect reaction.

Another finding that was discovered based on the acquired data was the inclusion of chloride has the delay effect on the solid-state synthesis of Fe₂GeS₄ when comparing the two chloride-based precursor series. The Acac-Gly series yielded Fe₂GeS₄ as a detectable phase at as early as 450 °C, but the Cl₂-Gly was first detected to have a Fe₂GeS₄ presence at 500 °C and the Cl₃-Gly series detected its at 550 °C. However, the chloride-based precursors had shown to provide a more robust reaction to form highly crystalline Fe₂GeS₄ product, which was observed in the robust reaction shown in the Cl₃-Gly series that the formation of the Fe₂GeS₄ phase from

500 °C to 550 °C had displayed a 71.9 ± 1.2 % growth and the eventual single-phase, high purity product formed at 600 °C.

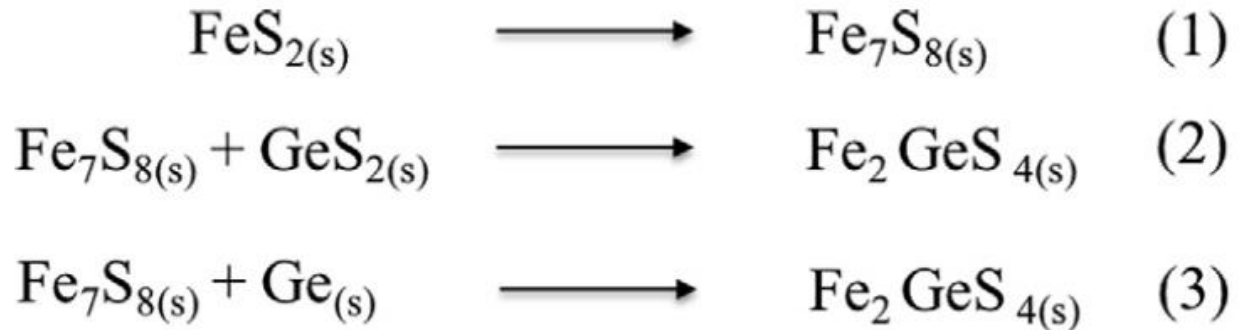


Figure 4.24. Proposed mechanism of Fe_2GeS_4 formation.

In summary, the conversion of the pyrite phase occurred with the increase in temperature, but the conversion would only attribute to the pyrrhotite phase. The formed pyrrhotite phase, with further increase in temperature, became reactive with the germanium in the mixture, either GeS_2 or Ge , to form the desired product Fe_2GeS_4 phase. Figure 4.24 above is the proposed mechanism of Fe_2GeS_4 formation based on the data and the hypothesis provided above. Despite the delay effect that came with the inclusion of chloride-based precursors, the $\text{Cl}_3\text{-Gly}$ series showed the rapid reaction that was capable to form the highly crystalline and phase pure product of Fe_2GeS_4 .

CHAPTER 5. FACILE APPROACH TO Fe_2GeS_4 NANOPARTICLE INK AND THIN-FILM PROCESSING

Introduction

Prior FeS_2 pyrite experiments were plagued with the formation of impurity phases, which shared disadvantageous electronic properties, that had undermined their capability to achieve photovoltaic effect. Despite the phase purity that the FeS_2 material could achieve as-synthesized, the issues of impurity phases tend to derive from the heat treatment, or annealing, that the thin-film devices need to undergo to be ready for further processing. Annealing is an important step in thin-film processing because it is typically used to remove the excess carbon in the ink and reduce the grain boundaries that had negative impacts on a photovoltaic device's performance. In the case of pyrite, the conversion could be initiated at relatively low to moderate temperatures, and previous attempt to perform the annealing under vacuum still could not deny the reaction to form pyrrhotite from happening. The inclusion of Fe_2GeS_4 was theorized to increase phase stability for the iron chalcogenide structure and should be capable to hold better against the heat treatment, but no temperature data so far had shown the appearance of the impurity to Fe_2GeS_4 at higher temperatures.

Background and Significance

The expectation of this stage of the experiment was to discover the ideal annealing temperature for Fe_2GeS_4 without the structure to collapse and generate pyrrhotite or other less advantageous phases. To this end, the process to produce a high-quality ink and thin-film device

was needed. Of the three precursor combination series that were examined in the previous sections, the Cl₃-Gly series Fe₂GeS₄ nanoparticles had been chosen as the powder material that was utilized for the ink processing because of its phase purity. This ensured that the experiment began with a phase pure product that had previously been examined with confidence and any changes to the thin-film's phase property was the result of either the ink or the thin-film processing. To ensure the Fe₂GeS₄ thin-film could survive further solution-based treatment in photovoltaic device processing, an adhesive vertical pull test was performed to determine the mechanical strength of the coated service. In doing so, this report will also be demonstrating a facile approach to produce high quality thin-films ready for PV cell assembly

5.1. Ink Quality Test

A photovoltaic device, which typically utilizes similar techniques to semiconductor manufacturing, tend to deposit the nanoparticle materials onto the substrates in layers via various ways, and a nanoparticle ink with agglomeration of the materials would create sizable uneven sites on the thin-film surface that could compromise the structural integrity of the layers of materials above it and the functionality of the entire device with it. Thus, quality of a nanoparticle ink is typically determined by the ability of the solvent to suspend the nanoparticles and to create a homogeneous ink solution.

The ink formation methods in this experiment were comprised of four samples and were designed in chronological orders as the latter samples were the improvements of the formers. The design of Ink 1 was based on the typical nanoparticle inks that were utilized for CZTS and

FeS₂ nanoparticles, but the result was not up to standard. The anhydrous toluene solvent could not properly disperse the Fe₂GeS₄ nanoparticle material as an obvious participation of materials were observed in Ink 1, shown in Figure 5.1(a). Many sizable agglomerates were also observed on the surface of the ink vial. Ink 2, shown in Figure 5.1(b), utilized the combination of α -terpineol and anhydrous toluene in a 1:3 volumetric ratio to produce a solution that have been reported to adjust viscosity, and it saw an increase in homogeneity as no obvious separation was observed³⁹. However, sizable agglomerates could still be observed on the surface. Shown in Figure 5.1(c), Ink 3 utilized the combination of the α -terpineol and anhydrous toluene solution and a mixed solvent of ethanol and anhydrous toluene to promote nanoparticle suspension. The ink produced was observed to have smaller sized agglomerates, with slightly better homogeneity, but was eventually uneven surface created due to the low homogeneity of the ink. From Ink 1 to 3, ultrasonication was utilized, but no significant improvement was observed. Ink 4 utilized the same ink solvents as Ink 3, but the mixing was done with a combination of ultrasonication and vigorous mixing with Speedmixer. The produced product was a smooth and homogeneous ink with no observable agglomerates, shown in Figure 5.1(d).

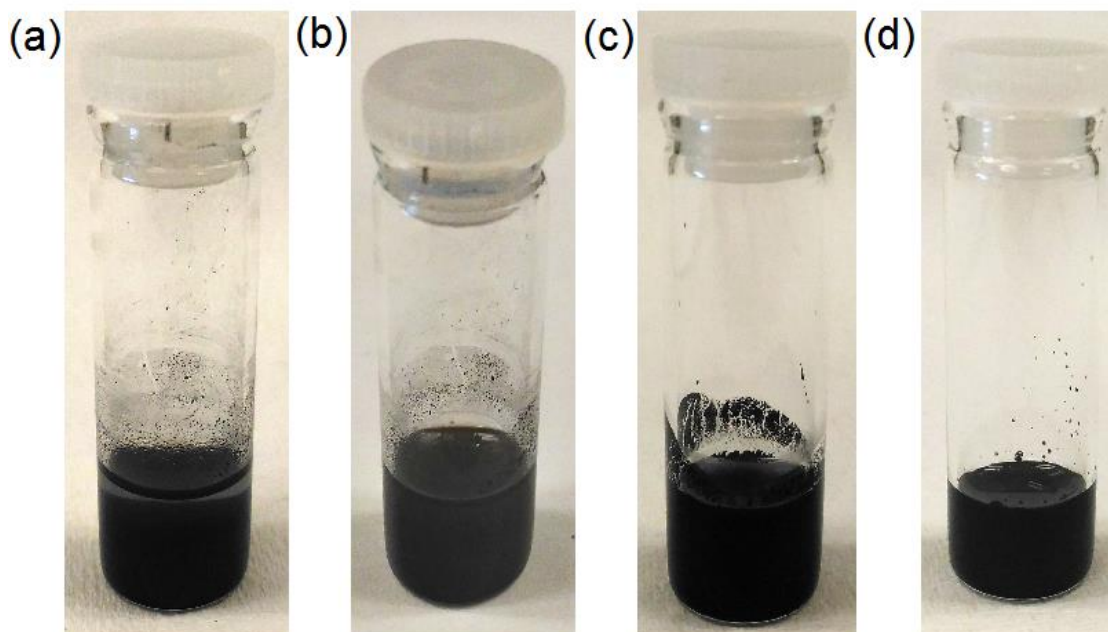


Figure 5.1. Photos of the Fe_2GeS_4 nanoparticle inks made (a) Ink 1, (b) Ink 2, (c) Ink 3 and (d) Ink 4.

5.2. Adhesion Test

The inks were then deposited onto quartz substrates with a typical bar-coating procedure and was placed under adhesion tests. A typical diagram of the lift-off pressure is illustrated in Figure 5.2. The adhesion test was designed to determine the maximum lift-off pressure, in 10^6 N/m^2 , of the thin-films the moment the glued pin had taken off from the coated surface, and the result of the test was listed in Table 5.1. For the adhesion tests for Ink 2 and 4, the quartz substrates had snapped or bent before the pined glue could take off, thus the lift-off pressure values were recorded at the maximum pressure that it was recorded just prior to the destruction of the substrates. It was noted that Ink 4 had displayed the strongest mechanical strength in comparison of other ink preparation methods, and was selected for the Thin-Film Annealing Test.

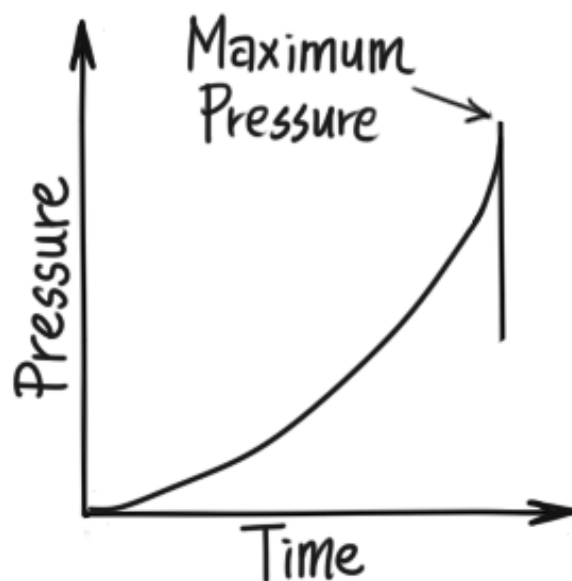


Figure 5.1. Typical diagram of lift-off pressure over time to determine the maximum pressure.

Sample	Components	Lift-Off pressure / Adhesion ($\cdot 10^6 \text{ N/m}^2$)
Ink 1	Toluene. 200 mg/ml.	4.3 ± 3
Ink 2	Toluene: α -Terpineol (v/v = 3:1). 200 mg/ml.	$> 54 \pm 36$
Ink 3	Toluene: α -Terpineol (v/v = 3:1), Toluene: Ethanol (4:1) + EC (6 wt%). 200 mg/ml.	7 ± 5
Ink 4	Toluene: α -Terpineol (v/v = 3:1), Toluene: Ethanol (4:1) + EC (6 wt%). 200 mg/ml.	$> 76 \pm 11$

Table 5.1. Comparison of the lift-off pressure of the sample ink 1 – 4 for the Adhesion Test.

5.3. Thin-Film Composition Test

As the previous steps of thin-film processing were conducted under air, the risk of creating impurity phase due to exposure to humidity, oxidation, decompose due to mechanical and thermal stress as an effect of ultrasonication and speedmixing, or the combination of the above factors, it was proposed to examine if the as-made Fe_2GeS_4 thin-film could retain the phase purity post thin-film processing. The measured XRD pattern of the as-made thin-film, as shown in Figure 5.3, and the Rietveld refinement data, shown in Table 5.2, details the phase analysis of the product. Based on the data shown, the Fe_2GeS_4 thin-film was able to remain the phase purity with % Phase at $100 \pm 3\%$. Raman spectroscopy of the films were taken to confirm the as-made Fe_2GeS_4 thin-film was able to remain a single-phase product with the absence of peaks that could be assigned to iron binary phases.

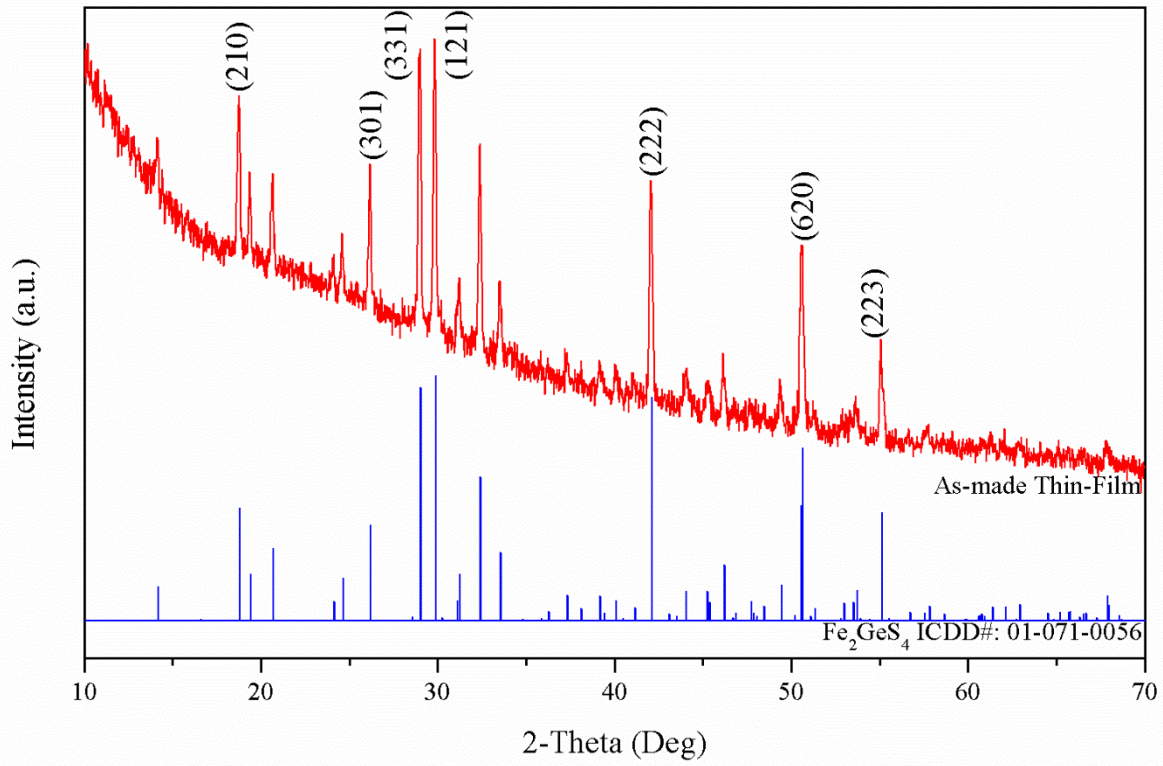


Figure 5.3. Comparison of the XRD patterns of the annealed Fe_2GeS_4 films from 400 °C to 600 °C.

Annealing Temperature	Observed Phases	ICDD No.	% Phase	Crystallite Size (nm)
As-made	Fe_2GeS_4	01-073-1074	100 ± 3	48.4 ± 17.0

Table 5.2. Refined phase analysis of Film Composition Study of Ink 4 post thin-film processing.

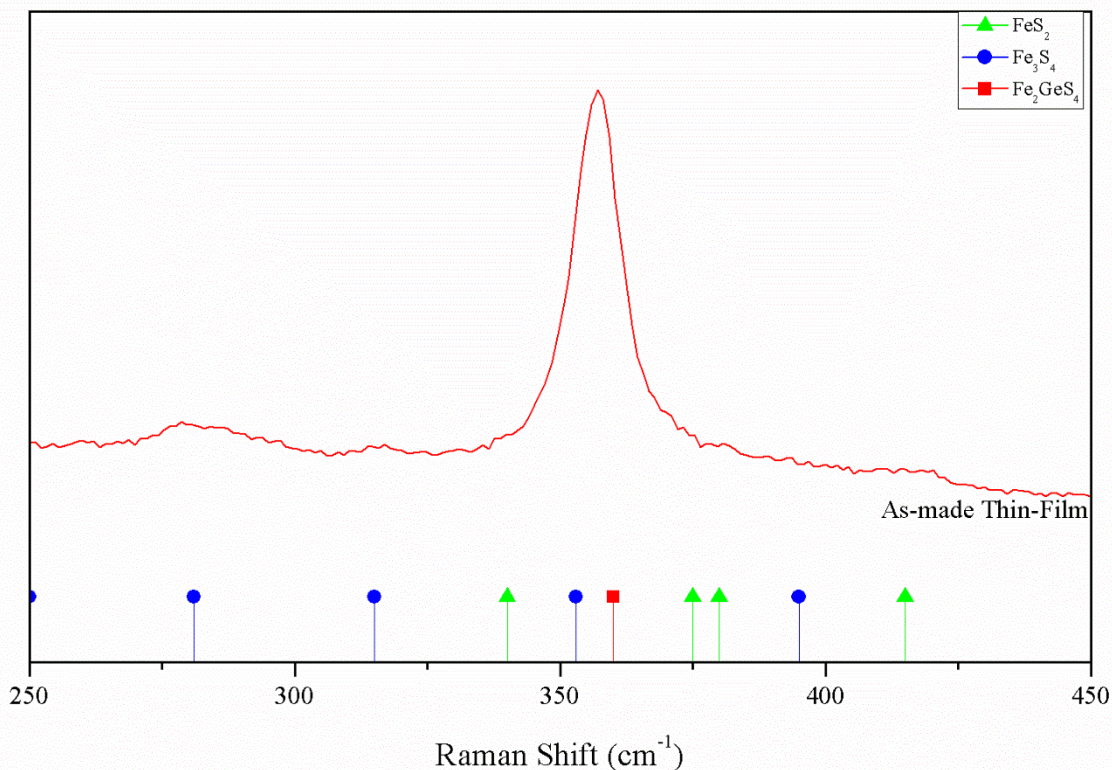


Figure 5.4. Raman spectroscopy of Film Composition Study of Ink 4 post thin-film processing. Each symbol and vertical drop-line marks different iron compound phase. The ■ symbol represents reference peaks of Fe_2GeS_4 , the ● symbol represents those of greigite, and the ▲ symbol represents those of pyrite.

5.4. Discussion

The $\text{Cl}_3\text{-Gly}$ series produced the single-phase Fe_2GeS_4 nanoparticle products at 600 °C. Once coated via bar-coating, it was discovered that the thin-films would lose the phase-purity as early as the at 400 °C, the lowest annealing temperature stage in the scope of this research. A possible explanation was the lack of sulfur atmosphere during the annealing process. The solid-state synthesis to generate Fe_2GeS_4 was a sulfurization process, where elemental sulfur was

atomized under high temperature and a steady argon flow was used to spread the sulfur atmosphere across the sites of precursor materials to participate in the reaction continuously until the annealing temperature was lowered to under the reaction temperature. On the other hand, the thin-film annealing test was done without the sulfur involved, which presented the scenario the samples had simply been under thermal decomposition as the annealing temperature increased during the process. Without examining the lower annealing environments, it is difficult to determine the thermal stability of Fe_2GeS_4 . Regardless, an unannealed Fe_2GeS_4 thin-film has been determined to provide excellent mechanical strength while retaining the phase purity, as shown by the Rietveld refinement and Raman spectrum obtained for the thin-film sample. The procedure has provided an optimal thin-film product ready for further PV assembly.

CHAPTER 6. CONCLUSION AND PATH FORWARD

Our research set out with the goal to improve FeS₂ pyrite as a photovoltaic material that has been plagued with the phase instability issue. The phase instability of pyrite begins with its lack of thermal stability, which makes the material prone to decompose into the S-deficient iron binary phases, such as Fe_{1-δ}S pyrrhotite, under low to moderate temperatures. With its less useful electronic and magnetic properties, S-deficient phases like pyrrhotite undermined the photovoltaic effect of a pyrite-based solar cell severely. To increase the stability of the iron sulfides, the inclusion of the metalloid germanium is conducted to formulate Fe₂GeS₄, the iron germanium sulfide. In this report, a rapid and highly scalable molecular precursor based solid-state synthesis route capable of generating high stability and phase pure Fe₂GeS₄ nanoparticles as well as a facile approach to produce high quality nanoparticle ink and thin-film device ready for PV device assembly is successfully demonstrated.

A solid-state synthesis such as the procedure presented in this report can provide an alternate route to synthesize greater yields of Fe₂GeS₄ nanoparticles than the solution-based synthesis, which typically does not translate well in the industrial scale. Despite the disadvantage of a higher reaction temperature requirement, the solid-state approach demonstrated in this report has shown the capability of better industrial adaption overall. In addition to the larger yield per synthesis, the preparation of the molecular precursors by grinding on a mortar and pestle takes only 10 min, and the facile annealing procedure to synthesize high-quality Fe₂GeS₄ nanoparticle takes only 5 h if including the cool-down time but could be used readily for characterization or further ink and thin-film processing. The total reaction time to obtain the product is only a quarter of the 24 h reaction time shown in previous publications³⁵, and this is not considering

the purification and the vacuum drying process necessary to wash the excess organic ligands and solvents away to obtain the purified product, which typically is an overnight procedure^{34,35}. The designed solid-state procedure, although simple in operation, has been proven in this research to provide a rapid procedure to synthesize the high-quality product with larger yield and shorter reaction time, which makes it very ideal for future commercialization.

Ink processing and thin-film processing demonstrated in this report is designed to be facile and robust in practice for the purpose of industrial adaptation in the future. By improving the ink recipes step by step, this report has presented a high-quality ink with high homogeneity with little to no agglomeration of the nanomaterial powders, a significant improvement as a roll-to-roll printable ink is realized. Determined by the Adhesion Test, a high vertical lift-off pressure value, an important mechanical strength parameter for a photovoltaic thin-film device, is determined. Not only is that the preparation for the nanoparticle ink could be completed very quickly, the fact that it can be deposited via a bar-coating procedure, commonly regarded as a crude deposition method, but still retain high-quality is nothing but a testament of the thin-film's quality itself.

To understand the nature of phase shift of iron sulfides better to our advantage, a detailed analysis of the percentage phase compositions of the iron sulfide phases, utilizing the Rietveld refinement, has provided great insights by showing all possible the detectable phases across the selected of annealing temperature stages in increments. Studying these phase analysis data by the associated temperature stages has provided great insights of the reaction trends and the nature of the phase shift paradigm integral and unique to the iron sulfide materials. It is observed that

pyrite would only decompose and convert into pyrrhotite, as shown by cases where the phase composition lost on pyrite were replaced by the increase of pyrrhotite. It is also observed that pyrrhotite phase being the only possible phase that can react with germaniums in the molecular precursors to form Fe_2GeS_4 , as instances where the % Phase of pyrite are found to be independent to the growth of Fe_2GeS_4 phase. In addition to the analysis of the phase shift mechanism, the delay effect of chloride-based precursor combination series was observed, yet, despite the delay effect, FeCl_3 has demonstrated a robust reaction to form the fastest percentage growth of Fe_2GeS_4 in a mere 50°C increment. These observations are important as it has challenged the traditional concept when it comes to iron sulfide binary chemicals forming ternary products. Previous publications have commonly suggested the role of FeS_2 as the precursor required to react to form a ternary from a binary iron sulfide. However, the discovery and evidence provided by this report has shown another possibility where the S-deficient phases in the form of $\text{Fe}_{1-\delta}\text{S}$ pyrrhotites are the actual precursors that have actually participated in the reaction. The conversion from pyrite to pyrrhotite to iron germanium sulfide is speculated to be the mechanism in the scope of this report, but it is the desire to continue the analysis at higher annealing temperature environments in a future date, so it would allow the determination of the phase shifts beyond iron germanium sulfide phase.

Lastly, the observations detailed in this report could be unique only to the iron sulfides, but this has showcased the capability of a temperature-based phase composition analysis to speculate the nature of a series of reactions by cooperating the functionality of XRD spectroscopy and Rietveld refinement together. A significant benefit could be the discovery of an alternate reaction route, as what is observed in the case of pyrrhotite over pyrite in the reaction to

synthesize Fe_2GeS_4 . Designing a synthetic process of a novel inorganic material with the help of the full realization of a phase shift mechanism of a specific family of materials, such as the case study of iron sulfides to iron germanium sulfide, could also prove invaluable as it could result in a more accurate and efficient design process.

REFERENCES

- [1] U.S. Energy Information Administration. (2017). U.S. electricity generation by source, amount, and share of total in 2017. Retrieved from <https://www.eia.gov/tools/faqs/faq.php?id=427&t=3>
- [2] Particle Pollution and Your Health (2013). [Graph illustration of the Air Quality Index for Particle Pollution September 2013]. Air Quality Index Data Access from United States Environmental Protection Agency. Retrieved from <https://www.epa.gov/pm-pollution/health-and-environmental-effects-particulate-matter-pm>
- [3] Huang, A., Han, S., Huang, W., & Liu X. (2013). Enhancing solar cell efficiency: the search for luminescent materials as spectral converters. *Chem. Soc. Rev.*, 42(1), 173 - 201.
- [4] Yoshikawa, K., Kawasaki, H., Yoshida, W., Irie, T., Konishi, K., Nakano, K., ... Yamamoto, K. (2017). Silicon heterojunction solar cell with interdigitated back contacts for a photoconversion efficiency over 26%. *Nature Energy*, 2(5) 17032.
- [5] Green M. A., Hishikawa, Y., Dunlop, E. D., Levi, D. H., Hohl-Ebinger, J., & Ho-Baillie, A. W. Y. (2018). Solar cell efficiency tables (version 52). *Progress in Photovoltaics: Research and Applications*, 26(7), 427 - 436.
- [6] Benick, J., Richter, A., Muller, R., Hauser, H., Feldmann, F., Krenckel, P., ... Glunz, S. W. (2017). High-Efficiency n-Type HP mc Silicon Solar Cells. *IEEE Journal of Photovoltaics*, 7(5), 1171 - 1175.
- [7] Matsui, T., Bidiville, A., Sai, H., Koida, T., Suezaki, T., ... Kondo, M. (2015). High-efficiency amorphous silicon solar cells: Impact of deposition rate on metastability. *Appl. Phys. Lett.*, 106(5), 053901.
- [8] National Renewable Energy Laboratory. Copper Indium Gallium Diselenide Solar Cells. Retrieved from <https://www.nrel.gov/pv/copper-indium-gallium-diselenide-solar-cells.html>
- [9] Bonnet, D., & Meyers, P. (1998). Cadmium-telluride - Material for thin film solar cells. *J. Mater. Res.*, 13(10), 2740 - 53.
- [10] Tempe, A. (2014, August 5). First Solar Builds the Highest Efficiency Thin Film PV Cell on Record. Business Wire. Retrieved from <https://www.businesswire.com/news/home/20140805006535/en/Solar-Builds-Highest-Efficiency-Thin-Film-PV>
- [11] Todorov, T. K., Tang, J., Bag, S., Gunawan, O., Gokmen, T., Zhu, Y., Mitzi, D. B. (2012). Beyond 11% Efficiency: Characteristics of State-of-the-Art $\text{Cu}_2\text{ZnSn}(\text{S},\text{Se})_4$ Solar Cells. *Adv. Energy Mater.*, 3(1), 34 - 38.

- [12] Yoshida, S. (2017 December 20). Solar Frontier Achieves World Record Thin-Film Solar Cell Efficiency of 22.9%. Solar Frontier. Retrieved from http://www.solar-frontier.com/eng/news/2017/1220_press.html
- [13] Smestad, G., Ennaoui, A., Fiechter, S., Tributsch, H., Hofmann, W. K., Birkholz, M., Kautek, W. (1990). Photoactive thin film semiconducting iron pyrite prepared by sulfurization of iron oxides. *Solar Energy Materials*, 20(3), 149 - 165.
- [14] Ennaoui, A., Fiechter, S., Pettenkofer, C., Alonso-Vante, N., Bükler, K., Bronold, M., ... Tributsch, H. (1993). Iron disulfide for solar energy conversion. *Solar Energy Materials and Solar Cells*, 29(4), 289 - 370.
- [15] Ennaoui, A., & Tributsch, H. (1984). Iron sulphide solar cells. *Solar Cells*, 13(2), 197 - 200.
- [16] Puthussery, J., Seefeld, S., Berry, N., Gibbs, M., & Law, M. (2011). Colloidal Iron Pyrite (FeS₂) Nanocrystal Inks for Thin-Film Photovoltaics. *J. Am. Chem. Soc.*, 133(4), 716 - 719.
- [17] Yu, L., Lany, S., Kykyneshi, R., Jieratum, V., Ravichandran, R., Altschul, E., ... Zunger, A. (2011). Iron Chalcogenide Photovoltaic Absorbers. *Adv. Energy Mater.*, 1(5), 748 - 753.
- [18] Zhang, Z., Niu, J., Yang, P., Gong, Y., Ji, Q., Shi, J., ... Zhang, Y. (2017). Van der Waals Epitaxial Growth of 2D Metallic Vanadium Diselenide Single Crystals and their Extra-High Electrical Conductivity. *Adv. Mater.*, 29(37), 1702359.
- [19] Ennaoui, A., Fiechter, S., Jaegermann, W., & Tributsch, H. (1986). Photoelectrochemistry of Highly Quantum Efficient Single-Crystalline n-FeS₂ (Pyrite). *Journal of The Electrochemical Society*, 133(1), 97.
- [20] Seehra, S. S., Montano, P. A., Seehra, M. S., & Sen, S. K. (1979). Preparation and characterization of thin films of FeS₂. *Journal of Materials Science*, 14(11), 2761 - 2763.
- [21] Steinhagen, C., Harvey, T. B., Jackson Stolle, C., Harris, J., & Korgel, B. A. (2012). Pyrite Nanocrystal Solar Cells: Promising, or Fool's Gold. *J. Phys. Chem. Lett.*, 3(17), 2352 - 2356.
- [22] Smestad, G., Ennaoui, A., Fiechter, S., Hofmann, W., Tributsch, H., & Kautek, W. (1990). Thin film preparation of semiconducting iron pyrite. *Optical Materials Technology for Energy Efficiency and Solar Energy Conversion IX*, 1272, 67 - 78. doi: 10.1117/12.20433
- [23] Höpfner, C., Ellmer, K., Ennaoui, A., Pettenkofer, C., Fiechter, S., & Tributsch, H. (1995). Stoichiometry-, phase- and orientation-controlled growth of polycrystalline pyrite (FeS₂) thin films by MOCVD. *Journal of Crystal Growth*, 151(3-4), 325 - 334.

- [24] Zhang, X., Scott, T., Socha, T., Nielsen D., Manno, M., Johnson, M., & Leighton, C. (2015). Phase Stability and Stoichiometry in Thin Film Iron Pyrite: Impact on Electronic Transport Properties. *ACS Appl. Mater. Interfaces*, 7(25), 14130 - 14139.
- [25] Limpinsel, M., Farhi, N., Berry, N., Lindemuth, J., Perkins, C. L., Lin, Q., & Law, M. (2014). An inversion layer at the surface of n-type iron pyrite. *Energy Environ. Sci.*, 7(6), 1974.
- [26] Zhang, Y. N., Hu, J., Law, M., & Wu, R. Q. (2012). Effect of surface stoichiometry on the band gap of the pyrite FeS₂(100) surface. *Phys. Rev. B*, 85(8). doi: 10.1103/physrevb.85.085314
- [27] Baruth, A., Manno, M., Narasimhan, D., Shankar, A., Zhang, X., Johnson, M., ... Leighton, C. (2012). Reactive sputter deposition of pyrite structure transition metal disulfide thin films: Microstructure, transport, and magnetism. *Journal of Applied Physics*, 112(5), 054328.
- [28] Hu, J., Zhang, Y., Law, M., & Wu, R. (2012). Increasing the Band Gap of Iron Pyrite by Alloying with Oxygen. *J. Am. Chem. Soc.*, 134(32), 13216 - 13219.
- [29] Macpherson, H. A. & Stoldt, C. R. (2012). Iron Pyrite Nanocubes: Size and Shape Considerations for Photovoltaic Application. *ACS Nano*, 6(10), 8940 - 8949.
- [30] Höpfner, C., & Ellmer, K. On the stoichiometry of the semiconductor pyrite (FeS₂). *Philosophical Magazine A*, 75(4), 1129 - 1151.
- [31] Thomas, B., Cibik, T., Höpfner, C., Diesner, K., Ehlers, G., Fiechter, S., & Ellmer, K. Formation of secondary iron-sulphur phases during the growth of polycrystalline iron pyrite (FeS₂) thin films by MOCVD. *Journals of Materials Science: Materials in Electronics*, 9(1), 61 - 64.
- [32] Birkholz, M., Fiechter, S., Hartmann, A., & Tributsch, H. (1991). Sulfur deficiency in iron pyrite (FeS_{2-x}) and its consequences for band-structure models. *Physical Review B*, 43(14), 11926 - 11936.
- [33] Vadkhiya, L., & Ahuja, B. L. (2011). Electronic and optical properties of iron pyrite. *Journal of Alloys and Compounds*, 509(6), 3042 - 3047.
- [34] Liu, M., Berg, D. M., Hwang, P., Lai, C., Stone, K. H., Babbe, F., ... Radu, D. R. (2018). The promise of solution-processed Fe₂GeS₄ thin films in iron chalcogenide photovoltaics. *J. Mater. Sci.*, 53(10), 7725 - 7734.

- [35] Fredrick, S. J., & Prieto, A. L. (2013). Solution Synthesis and Reactivity of Colloidal Fe₂GeS₄: A Potential Candidate for Earth Abundant, Nanostructured Photovoltaics. *J. Am. Chem. Soc.*, 135(49), 18256 - 18259.
- [36] Park, B., Yu, S., Hwang, Y., Cho, S., Lee, J., Park, C., ... Lee, S. Y. (2015). Highly crystalline Fe₂GeS₄ nanocrystals: green synthesis and their structural and optical characterization. *J. Mater. Chem. A*, 3(5), 2265 - 2270.
- [37] Chiang, H., Wang, M., & Ueng, C. (1993). Synthesis and Structure of Diaquabis(glycolato-O,O")germanium(IV). *Acta Cryst.*, C49, 244 - 246.
- [38] ICDD (2018). PDF-4+ 2018 (Database), edited by Dr. Soorya Kabekkodu, International Centre for Diffraction Data, Newton Square, PA, USA
- [39] Cho, J., Ismail, A., Park, S., Kim, W., Yoon, S., & Min, B. (2013). Synthesis of Cu₂ZnSnS₄ Thin Films by a Precursor Solution Paste for Thin Film Solar Cell Applications. *ACS Appl. Mater. Interfaces*, 5(10), 4162 - 4165.